



THE HONG KONG
POLYTECHNIC UNIVERSITY

香港理工大學

Pao Yue-kong Library
包玉剛圖書館

Copyright Undertaking

This thesis is protected by copyright, with all rights reserved.

By reading and using the thesis, the reader understands and agrees to the following terms:

1. The reader will abide by the rules and legal ordinances governing copyright regarding the use of the thesis.
2. The reader will use the thesis for the purpose of research or private study only and not for distribution or further reproduction or any other purpose.
3. The reader agrees to indemnify and hold the University harmless from and against any loss, damage, cost, liability or expenses arising from copyright infringement or unauthorized usage.

If you have reasons to believe that any materials in this thesis are deemed not suitable to be distributed in this form, or a copyright owner having difficulty with the material being included in our database, please contact lbsys@polyu.edu.hk providing details. The Library will look into your claim and consider taking remedial action upon receipt of the written requests.

THE HONG KONG POLYTECHNIC UNIVERSITY

DEPARTMENT OF APPLIED PHYSICS

**RAMAN AND OPTICAL CHARACTERIZATION OF
TUNGSTEN BRONZE NIOBATES THIN FILMS AND
NANOCRYSTALS**

LIU WEN CHAO

**A THESIS SUBMITTED IN PARTIAL FULFILMENT
OF THE REQUIREMENTS FOR THE DEGREE OF
DOCTOR OF PHILOSOPHY**

September, 2008

CERTIFICATE OF ORIGINALITY

I hereby declare that this thesis is my own work and that, to the best of my knowledge and belief, it reproduces no material previously published or written, nor material that has been accepted for the award of any other degree or diploma, except where due acknowledgement has been made in the text.

_____ (Signed)

Liu Wen Chao (Name of student)

ABSTRACT

Lead-free ferroelectric niobates with tetragonal tungsten-bronze (TTB) structure have large spontaneous polarization, significant piezoelectric properties, enhanced photorefractive and nonlinear optic properties. Among various TTB niobates, calcium-modified strontium sodium niobate, $\text{Sr}_{2-x}\text{Ca}_x\text{NaNb}_5\text{O}_{15}$ (SCNN, $0.05 \leq x \leq 0.35$) and $\text{Sr}_{1-x}\text{Ba}_x\text{Nb}_2\text{O}_6$ (SBN, $0.25 < x < 0.75$) are two typical materials. With similar structure, SCNN presents similar electro-optic, pyroelectric and piezoelectric with SBN. By adding Na into the void site, the Curie temperature of SCNN is substantially increased.

The planar waveguide structures have been proposed and demonstrated for many applications, including nonlinear optical devices, electro-optic waveguide modulators and passive integrated optical circuits. The fabrication of SCNN waveguides is very attractive because the optical confinement inherent in the waveguide structure allows a significant improvement in the efficiency of the electro-optic and nonlinear optical applications. Optical waveguides can be achieved by depositing the SCNN films on a substrate of lower refractive index such as MgO and fused quartz. We focus on studying the relationship between microstructures and optical waveguide properties

(i.e., refractive index, birefringence, transmittance and propagation loss). We have investigated the optical properties of the planar waveguides using the prism coupler technique. The ordinary (n_o) and the extraordinary (n_e) refractive indices of the SCNN/MgO films are determined to be 2.278 and 2.183, respectively. The relatively large index difference of 0.095 due to uniaxial birefringence is the result of anisotropic crystal microstructure. An optical propagation loss of 0.90 dB/cm for the TE₀ mode of the SCNN/MgO waveguide was measured. Thermal and electric field dependence of the refractive indices of SCNN and SBN thin films has been discussed.

Raman spectroscopy is a powerful and sensitive technique used to study the crystalline structures based on the vibrational bands. We investigated the temperature induced ferroelectric to paraelectric phase transition of epitaxial SCNN and SBN thin films using thermo-Raman spectroscopy. The temperature dependence of peak position and FWHM of the Raman bands around 238 cm⁻¹ present obvious softening (shift to lower wavenumber) and clear anomalies near the phase transition.

Temperature dependence of Brillouin light scattering (BLS) was employed to investigate the phase transition and dynamics of polar nanoregions of the SCNN film on Si substrate. The LA and TA mode

frequency shifts change continuously with temperature. A broad increase in the LA and TA shifts are found near 270 °C in the heating process. Such a continuous change is typical for relaxor ferroelectrics. A broad clear central peaks (CPs) was observed, we believe that the CPs is related to polarization fluctuations along the c axis.

Magnetoelectric (ME) materials have attracted wide and increasing attention due to their attractive physical properties and potential applications in actuators, transducers, field sensors, and data storage devices. We selected SCNN $\text{Sr}_{1.9}\text{Ca}_{0.1}\text{NaNb}_5\text{O}_{15}$ (SCNN) and Co-ferrite CoFe_2O_4 (CFO) as the ferroelectric and ferrimagnetic components due to a high Curie point for the ferroelectric phase, a high Néel temperature for the ferrimagnetic phase, and large piezoelectric as well as magnetostrictive coefficients. A remarkable dielectric constant dispersion spectrum with Curie temperature of 270 °C was observed. A well-defined ferroelectric hysteresis loop and a ferrimagnetic hysteresis loop were obtained for the same composite ceramic. A maximum ME coupling coefficient α_E of 58 mV/cm·Oe was obtained under zero dc bias and an ac magnetic field of 10 Oe at 88 kHz.

LIST OF PUBLICATIONS

1. **W. C. Liu**, C. L. Mak, K. H. Wong, D. Y. Wang, and H. L. W. Chan, “Optical properties of epitaxial and polycrystalline $\text{Sr}_{1.8}\text{Ca}_{0.2}\text{NaNb}_5\text{O}_{15}$ thin-film waveguides grown by pulsed laser deposition”, *J. Appl. Phys.* 100, 033507 (2006)
2. Z. R. Shen, H. Ye, C. L. Mak, K. H. Wong, T. Y. Yum, **W. C. Liu**, T. Zhou, “Preparation of highly c-axis oriented $\text{Sr}_{0.6}\text{Ba}_{0.4}\text{Nb}_2\text{O}_6$ thin films grown on silicon substrate by the sol-gel process”, *Mater. Chem. Phys.* 99, 10 (2006)
3. A. D. Li, J. Tan, **W. C. Liu**, C. L. Mak, K. H. Wong, H. Ye, D. Wu, N. B. Ming, “Fabrication and characteristics of $\text{Sr}_{0.6}\text{Ba}_{0.4}\text{Nb}_2\text{O}_6$ films prepared by pulse laser deposition”, *Ferroelectrics.* 332, 159 (2006)
4. **W. C. Liu**, C. L. Mak and K.H. Wong, “Optical waveguiding in epitaxial $\text{Sr}_{1.8}\text{Ca}_{0.2}\text{NaNb}_5\text{O}_{15}$ films integrated on Si(0 0 1) substrates”, *J. Phys. D.* 40, 749 (2007)
5. J. Tan, A. D. Li, X. Z. Fan, **W. C. Liu**, Z. X. Xu, Y. Lin, H. T. Wang, D. Wu, N. B. Ming, “Effects of processing on all-optical poling characteristics of guest-host azo-dye polymer thin films”, *Phys. Stat. Sol. A.* 204, 1114 (2007)

6. **W. C. Liu**, C. L. Mak, K. H. Wong, C. Y. Lo, S. W. Or, W. Zhou, A. Hauser, F. Y. Yang and R. Sooryakumar, “Magnetolectric and dielectric relaxation properties of the high Curie temperature composite $\text{Sr}_{1.9}\text{Ca}_{0.1}\text{NaNb}_5\text{O}_{15}\text{-CoFe}_2\text{O}_4$ ”, J. Phys. D: Appl. Phys. 41, 125402 (2008).
7. **W. C. Liu**, G. Hoffman, W. Zhou, R. M. Reano, P. Boolchand, and R. Sooryakumar, “Slab waveguides and nanoscale patterning of pulsed laser-deposited $\text{Ge}_{0.2}\text{Se}_{0.8}$ chalcogenide films”, Appl. Phys. Lett. 93, 041107 (2008)
8. **W. C. Liu**, A. D. Li, C. L. Mak, K. H. Wong, “Fabrication and Electro-optic Properties of Ferroelectric Nanocrystal/Polymer Composite Films”, J. Phys. Chem. C. 112, 14202-14208 (2008).
9. B. Fei, B. T. Qian, Z. Y. Yang, R. H. Wang, **W. C. Liu**, C. L. Mak, John H. Xin, “Coating carbon nanotubes by spontaneous oxidative polymerization of dopamine”, Carbon. 46, 1795 (2008).
10. G. B. Hoffman, **W. C. Liu**, W. Zhou, R. Sooryakumar, P. Boolchand, R. M. Reano, “Relief and Trench Formation on Chalcogenide Thin-Films Using Electron Beams”, J. Vac. Sci. Technol. B.26, 2478 (2008).
11. **W. C. Liu**, C. L. Mak, K. H. Wong, “Temperature effect on Raman

scattering of the epitaxial $\text{Sr}_{1.9}\text{Ca}_{0.1}\text{NaNb}_5\text{O}_{15}$ film”, *Thin. Solid. Films.*

Accepted (2008).

Conference poster

1. **W. C. Liu**, C. L. Mak, K. H. Wong, C. Y. Lo, S. W. Or, W. Zhou, A. Hauser, F. Y. Yang, R. Sooryakumar, “Magnetolectric Properties of the High Curie Temperature Relaxor Composite $\text{Sr}_{1.9}\text{Ca}_{0.1}\text{NaNb}_5\text{O}_{15}\text{-CoFe}_2\text{O}_4$ ”, 52rd Annual Conference on Magnetism and magnetic Materials (MMM), Tampa, USA, 2007. The Best Poster Award.
2. **W. C. Liu**, C. L. Mak, K. H. Wong, “Temperature effect on Raman scattering of the epitaxial $\text{Sr}_{1.9}\text{Ca}_{0.1}\text{NaNb}_5\text{O}_{15}$ film”, The 4th International Conference on Technological Advances of Thin Films & Surface Coatings (Thinfilms 2008), Singapore, (2008)
3. Galen Hoffman, **Wenchao Liu**, Wei Zhou, R Sooryakumar, Punit Boolchand and Ronald Reano, “Relief And Trench Formation On

Chalcogenide Thin-Films Using Electron Beams”, THE 52nd
INTERNATIONAL CONFERENCE on ELECTRON, ION, and
PHOTON BEAM TECHNOLOGY & NANOFABRICATION, Portland.
(2007)

ACKNOWLEDGMENT

I enjoyed my research work every day in the past three years. First of all I would sincerely like to express my appreciation to my supervisor Dr. C. L. Mak for his valuable guidance, continuous support, encouragement and patience in the whole period of my research study. He gave me enough freedom in the selection of research field and constructive suggestion in the project design, experiment and results publication. I will also never forget his warm encouragement when I was in a very difficult situation. I am happy to study and work with his guidance.

I would like also to thank Prof. K. H. Wong of PLD group for his guidance and nice encouragement in the whole period. I am impressed by his personality as well as the attitude toward research works. I also like to give my appreciation to Prof. R. Sooryakumar of The Ohio State University for his guidance and endless support when I was in OSU

I also want to give my appreciation for the help and assistance from the my groupmates, namely Ms. C. Y. Lam, Ms. C. S. Ng, Ms. L. Zhuang, Ms. M. Y. Pang, Ms. X. T. Li, Mr. Y. T. Yu, M. Y. B. Yao, Mr. M. H. Wong, Mr. W. L. Sin, Mr. C. H. Lau, Mr. H. F. Wong, Mr. Y. K. Chan, Mr. Z. R.

Shen, Mr. X. Jin, Mr. W. F. Cheng. I would like to thank Dr. H. Ye, Mr. Mr. M. N. Yeung, Mr. W. Zhou for their assistance in material characterization.

At last but not least, I must give my deepest appreciations to my parents and my family. Without their endless love, continuous support, encouragement and understanding, it is impossible for me to complete the Ph.D process. I love them forever.

I gratefully acknowledge the financial support from the Research Grants Council (RGC) of the Hong Kong Special Administrative Region and technical support provided by Materials Research Centre (MRC) of the Hong Kong Polytechnic University. I am grateful for the award of a research studentship by the Hong Kong Polytechnic University.

ABSTRACT.....	I
LIST OF PUBLICATIONS	IV
ACKNOWLEDGMENT.....	VIII
List of Figures	XV
List of Tables.....	XXI
1 INTRODUCTION	1
1.1 BACKGROUND	1
1.2 FERROELECTRIC MATERIAL	5
1.2.1 History	5
1.2.2 Polarization	5
1.2.3 P-E loop.....	7
1.2.4 Curie temperature.....	9
1.3 TUNGSTEN TETRAGONAL BRONZE NIOBATES MATERIALS	11
1.4 OPTICAL WAVEGUIDE.....	18
1.4.1 Background.....	18
1.4.2 Optical waveguide theory.....	19
1.5 ELECTRO-OPTIC EFFECT.....	27
1.5.1 Refractive index.....	27
1.5.2 Optical Birefringence	28
1.5.3 Electro-optic effect	29
1.6 SCOPE OF THE PRESENT STUDY	34
1.7 STATEMENT OF ORIGINAL CONTRIBUTIONS	36
2 FILM FABRICATION AND CHARACTERIZATION	39
2.1 PULSED LASER DEPOSITION.....	39

2.1.1	<i>Introduction</i>	39
2.1.2	<i>Film deposition</i>	42
2.2	RELATIONSHIP OF DEPOSITION CONDITIONS AND STRUCTURAL AND SURFACE MORPHOLOGY OF SCNN THIN FILMS	47
3	OPTICAL PROPERTIES OF SCNN AND SBN FILMS	51
3.1	OPTICAL PROPERTIES OF EPITAXIAL AND POLYCRYSTALLINE SCNN FILMS	51
3.1.1	<i>Introduction</i>	51
3.1.2	<i>Structural and morphology properties</i>	53
3.1.3	<i>Optical transmission properties</i>	59
3.1.4	<i>Waveguide properties</i>	63
3.1.5	<i>Conclusion</i>	71
3.2	OPTICAL WAVEGUIDING IN EPITAXIAL SR _{1.8} CA _{0.2} NANB ₅ O ₁₅ FILMS INTEGRATED ON SI(001) SUBSTRATES	73
3.2.1	<i>Introduction</i>	73
3.2.2	<i>Experimental detail</i>	74
3.2.3	<i>Structural characterization</i>	76
3.2.4	<i>Waveguide properties</i>	80
3.2.5	<i>Waveguide properties of epitaxial SCNN/In:Mg_xZn_{1-x}O/TiN/Si heterostructure</i>	86
3.2.5.1	<i>Introduction</i>	86
3.2.5.2	<i>Experiment detail</i>	88
3.2.5.3	<i>Structure and waveguide properties</i>	88

3.2.6	<i>Conclusion</i>	95
3.3	THERMO-OPTIC PROPERTIES OF SBN FILMS	96
3.3.1	<i>Introduction</i>	96
3.3.2	<i>Film fabrication</i>	98
3.3.3	<i>Thermo-optical properties of SBN/fused quartz films</i>	99
3.3.4	<i>Conclusion</i>	108
3.4	EO COEFFICIENT MEASUREMENT OF SCNN/FUSED QUARTZ	
	109	
3.4.1	<i>Introduction</i>	109
3.4.2	<i>Structural characterization</i>	109
3.4.3	<i>Transmission and E-O measurement</i>	111
3.4.4	<i>Conclusion</i>	117
3.5	A POTENTIAL APPLICATION OF PRISM COUPLER	
	TECHNIQUE: ROUGHNESS SENSOR	118
3.5.1	<i>Introduction</i>	118
3.5.2	<i>Results and discussion</i>	119
4	RAMAN AND BRILLOUIN SCATTERING INVESTIGATION OF SBN AND SCNN THIN FILMS	121
4.1	PHASE TRANSITION INVESTIGATION OF THE EPITAXIAL $\text{Sr}_{1.9}\text{Ca}_{0.1}\text{NaNb}_5\text{O}_{15}$ FILM USING THERMO-RAMAN SCATTERING	121
4.1.1	<i>Introduction</i>	122
4.1.2	<i>Experimental details</i>	125
4.1.3	<i>Raman scattering results and discussion</i>	126
4.1.4	<i>Conclusion</i>	133

4.2	PHASE TRANSITION INVESTIGATION OF THE EPITAXIAL SBN60 FILM USING THERMO-RAMAN SCATTERING	134
4.2.1	<i>Introduction</i>	134
4.2.2	<i>Thermo-Raman spectra results and discussion</i>	136
4.2.3	<i>Conclusion</i>	144
4.3	CENTRAL PEAKS, ACOUSTIC MODES, AND THE DYNAMICS OF POLAR NANOREGIONS IN OF HIGH ORIENTED SCNN THIN FILMS ON SI SUBSTRATE BY BRILLOUIN SCATTERING.	145
4.3.1	<i>Introduction</i>	145
4.3.2	<i>Experiment details</i>	149
4.3.3	<i>Results and discussion</i>	152
4.3.4	<i>Conclusion</i>	168
5	MAGNETO-ELECTRIC AND DIELECTRIC RELAXOR PROPERTIES OF THE SR _{1.9} CA _{0.1} NANB ₅ O ₁₅ -COFE ₂ O ₄ COMPOSITE	169
5.1	INTRODUCTION.....	170
5.2	EXPERIMENTAL DETAILS	171
5.3	RESULTS AND DISCUSSION.....	172
5.4	CONCLUSION	182
6	FABRICATION OF SBN NANOCRYSTALS.....	183
6.1	INTRODUCTION.....	183
6.2	FABRICATION OF NANOCRYSTALS	185
6.3	CHARACTERIZATION.....	186
6.4	CONCLUSION	189
7	CONCLUSIONS AND FUTURE WORK.....	190

7.1	CONCLUSIONS	190
7.2	FUTURE WORK	195
	References	197
	<i>Appendix</i>	
	A1. X-ray Diffraction	212
	A2. Scanning Electron Microscopy (SEM) and Energy-Dispersive X-ray spectrometer (EDX)	215
	A3. Atomic Force Microscopy (AFM)	217
	A4. Transmission spectrometer	218
	A5. Prism Coupler technique	220
	A6. Raman spectroscopy	221
	A7. Brillouin light Scattering (BLS)	224
	A8. Vibrating sample magnetometer	226
	A9. P-E loop measurement	228

List of Figures

Fig. 1.1 (a) Linear, (b) nonlinear and (c) nonlinear loop relationships of polarization and electric field.....	6
Fig. 1.2 A typical P-E hysteresis loop of ferroelectrics.....	8
Fig. 1.3 Projection of $\text{Sr}_{0.61}\text{Ba}_{0.39}\text{Nb}_2\text{O}_6$ along the c axis.....	17
Fig. 1.4 Schematic of planar waveguide and reflection of the plane TE-wave	20
Fig. 1.5 Schematic diagram of the prism coupler.	25
Fig. 2.1 A schematic diagram of the PLD system used in our laboratory.....	41
Fig. 2.2 θ - 2θ XRD pattern of SCNN 19 target.	43
Fig. 2.3 XRD θ - 2θ scan patterns of SCNN thin films deposited on MgO (100) substrates at different temperatures.....	47
Fig. 2.4 (a) rocking curve of the (002) diffraction peak for SCNN thin films grown on MgO (001) substrate at different temperature; (b) FWHM as a function of substrate temperature.....	49
Fig. 2.5 SEM micrographs showing the surface morphologies of SCNN films deposited at: (a) 400 °C; (b) 500 °C; (c) 600 °C and (d) 700 °C.	50
Fig. 3.1 X-ray diffraction patterns of SCNN films on (a) fuse quartz and (b) MgO substrates. Inset is the rocking curve of (200)SCNN peak of SCNN/MgO film. (c) Phi-scan pattern of SCNN films on MgO substrates. (d) is illustration of one unit cell of SBN corresponding to sixteen unit cells of the MgO substrate.....	56
Fig. 3.2 Schematic diagrams show single SCNN unit cell sitting on 3×3 MgO lattice. In (a), the 3×3 MgO lattice has zero rotation with respect to the SCNN unit cell. In (b), a 45° rotation is shown. It is noticed that in (b), the	

NbO ₆ octahedrons (B1 sites) are aligned with the MgO unit cells.	57
Fig. 3.3 AFM images of SCNN films on (a) fused quartz and (b) MgO substrates.....	58
Fig. 3.4 The wavelength dependence of transmittance for SCNN films on fused quartz and MgO substrates and SCNN single crystal. The inset is plots of $(h\omega\alpha)^2$ as a function of $h\omega$ for SCNN/fused quartz and SCNN/MgO films. Extrapolating the line to intersect with the energy axis, E_g was obtained.....	61
.....	61
Fig. 3.5 Dispersion of the refractive index of SCNN films on fused quartz and MgO substrates obtained by optical transmission data. Inset is plots of $1/(n^2 - 1)$ as a function of $1/\lambda^2$	62
Fig. 3.6 Mode spectra of SCNN/MgO thin films in (a) TE and (b) TM polarizations and SCNN/fused quartz films in (c) TE and (d) TM polarizations.	64
Fig. 3.7 TE refractive index profiles obtained by an inverse WKB method for SCNN films deposited on fused quartz and MgO.	66
Fig. 3.8 Optical attenuation of different order modes of (a) SCNN waveguide on MgO and (b) SCNN waveguide on fused quartz. (c) Photograph of a screen image of the propagating 633 nm He-Ne laser beam in SCNN/MgO films.	69
Fig. 3.9 Optical propagation loss and FWHM of different order modes of TE guided modes coupled to the SCNN waveguide structures on MgO and fused quartz substrates.....	70
Fig. 3.10 XRD θ - 2θ profile of the SCNN/MgO/TiN/Si heterostructure. Left inset shows the XRD ω -scans of the SCNN(002) and TiN&MgO(002) planes. Right inset shows the ϕ -scans at the Si(111), TiN&MgO(111) and SCNN(221)	

planes.	78
Fig. 3.11 SEM cross-section image of the SCNN/MgO/TiN/Si heterostructure. Inset is the SEM surface morphology image of the SCNN film on MgO/TiN/Si.	80
Fig. 3.12 Excited (a) TM-line and (b) TE-line (lower plot) spectra for the air/SCNN/MgO waveguiding structure on a TiN buffered Si substrate.	82
Fig. 3.13 The digital camera captured photographs of excited (a) TM mode-lines and (b) TE mode-lines at 632.8 nm coupled into the SCNN film deposited on MgO/TiN/Si.	83
Fig. 3.14 Optical loss measurement (at TE ₀ mode) of the air/SCNN/MgO waveguide on a TiN buffered Si substrate.	85
Fig. 3.15 XRD θ -2 θ profile of the SCNN/In:c-MZO/TiN/Si heterostructure.	91
Fig. 3.16 XRD ω -scans of the SCNN(002) and TiN&In:c-MZO(002) planes.	92
Fig. 3.17 ϕ -scans of the Si(111), TiN&In:c-MZO(111) and SCNN(221) planes.	92
Fig. 3.18 TE and TM modes of In:c-MZO films on fused quartz substrates.	93
Fig. 3.19 Excited (a) TE-line and (c) TM-line spectra for the air/SCNN/In:c-MZO waveguiding structure on a TiN buffered Si substrate. The digital camera captured photographs of excited (b) TE mode-lines and (d) TM mode-lines at 632.8 nm coupled into the SCNN film deposited on In:c-MZO/TiN/Si.	94
Fig. 3.20 Apparatus for measuring the thermo-optical coefficient of thin films using a prism coupler technique.	99

Fig. 3.21 Temperature dependence of refractive index of SBN films on fused quartz.....	104
Fig. 3.22 Temperature dependence of thermo-optical coefficient of SBN films on MgO.....	105
Fig. 3.23 Experimental and theory data of temperature dependence of refractive index.....	106
Fig. 3.24 The mode spectrum and their enlarged figure at room temperature and Curie temperature.....	106
Fig. 3.25 X-ray θ - 2θ scans of (a) SCNN ceramic and (b) thin films deposited on fused quartz substrates. The inset is SEM surface and cross-section image of the SCNN films on fused quartz.....	110
Fig. 3.26 The wavelength dependence of transmittance for SCNN films on fused quartz. Inset is plot of $(h\omega\alpha)^2$ as a function of $(h\omega - E_g)$. Extrapolating the line to intersect with the energy axis, E_g was obtained.	111
Fig. 3.27 Excited (a) TE-line and (b) TM-line (lower plot) spectra for the air/SCNN/fused quartz waveguiding structure. The left inset (a) shows the schematic diagram of the set-up for measuring EO coefficient. The inset in (a) and inset in (b) are the digital camera captured photographs of excited TE mode-lines and TM mode-lines at 632.8 nm, respectively.	115
Fig. 3.28 (a) Reflectivity mode line curves measured with TM polarized light with (dot line) and without (solid line) an applied voltage. (b) Added voltage induced displacement of the refractive index.	116
Fig. 3.29 Evolution of FWHM of the TE ₀ excited guided-mode with roughness of SCNN films.	120
Fig. 4.1 Schematic representation of the structural skeleton of the TTB type structure projected on the a - b plane. Square, pentagonal, and triangular	

tunnels available for cation inclusion can be observed.....	124
Fig. 4.2 Room temperature Raman spectrum of SCNN.	127
Fig. 4.3 Temperature dependence of the Raman spectra of the main mode (at around 238 cm ⁻¹) for the SCNN film.	128
Fig. 4.4 Temperature dependence of the (a) Raman shift and (b) full width at half maximum (FWHM) of the main mode (at around 238 cm ⁻¹) for the SCNN film.	130
Fig. 4.5 Temperature dependence of the Raman spectra for the epitaxial SBN60 film.	139
Fig. 4.6 Raman spectra and multi-peak lorentzian fit at 170 °C for the epitaxial SBN60 film.	139
Fig. 4.7 Temperature dependence of the (a) Raman shift and (b) full width at half maximum (FWHM) of the main mode (at around 625 cm ⁻¹) for the SBN film.....	142
Fig. 4.8 Temperature dependence of the (a) Raman shift and (b) full width at half maximum (FWHM) of the main mode (at around 242 cm ⁻¹) for the SBN film.....	143
Fig. 4.9 Schematic of the experimental Brillouin scattering set-up in backscattering geometry. FP1 and FP2 represent the Fabry-Perot etalons; M, L and S identify various mirrors, lenses and slits, respectively. BS is a beam splitter and R a corner cube.	151
Fig. 4.10 Linkam high temperature cell (model TMS94). (a). Control Unit; (b). Sample Stage; (c). Water Tank & Pump.	151
Fig. 4.11 Brillouin spectra at various temperatures observed in heating process.....	153
Fig. 4.12 Temperature dependence of the frequency shift of TA mode	154

Fig. 4.13 Temperature dependence of the FWHM of TA mode.....	154
Fig. 4.14 Temperature dependence of the frequency shift of LA mode.....	155
Fig. 4.15 Temperature dependence of the FWHM of LA mode	155
Fig. 4.16 Temperature dependence of refractive index.....	158
Fig. 4.17 Temperature dependences of elastic constants: (a) C_{11} and (b) C_{44} determined using Brillouin scattering	159
Fig. 4.18 Temperature dependences of Young's modulus.....	160
Fig. 4.19 Temperature dependence of the FWHM of central peak	162
Fig. 4.20 Temperature dependence of the relaxation time.....	168
Fig. 5.1 (a) XRD patterns of the SCNN-CFO composite ceramic. (b) SEM micrographs of the polished and etched surface of composite ceramic. (The inset is an enlarged image of the labeled rectangular of the etched region)	173
Fig. 5.2 Temperature dependence of the dielectric constant of the SCNN-CFO composite ceramic at various frequencies.	175
Fig. 5.3 Plot of $\ln(\varepsilon_m / \varepsilon - 1)$ as a function of $\ln(T - T_m)$ for the SCNN-CFO composite ceramics.....	177
Fig. 5.4 (a) Polarization-electric (PE) hysteresis loop and (b) ferromagnetic hysteresis (MH) loop of the SCNN-CFO composite ceramic.	179
Fig. 5.5 Frequency dependence of experimental α_E at ac magnetic field of 10 Oe for the SCNN-CFO composite ceramic at room temperature. The inset shows the dc bias magnetic field dependence of α_E	181
Fig. 6.1 XRD patterns of SBN nanocrystals.....	187
Fig. 6.2 The TEM photographs of: SBN nanocrystals. and the energy dispersive x-ray spectrum of SBN nanocrystals.	188
Fig. 6.3 Raman spectrum of as-synthesized SBN nanocrystals.....	188
Fig. A1 Bragg'S Law	213

Fig. A2 Phi and omega scan.....	215
Fig. A3 Schematic of the major components of an AFM	218
Fig. A4 Energy level diagram showing the states involved in Raman signal.	222
Fig. A5 Schematic of the vibrating sample magnetometer.	227
Fig. A6 Schematic of the Sawyer-Tower.	230

List of Tables

Table 1.1 Electric and optical properties of SBN.	13
Table 1.2 Electric and optical properties of SCNN.....	14
Table 2.1. PLD growth condition.....	45
Table 3.1 Thermo-optical coefficients of some TO materials.....	107

1 Introduction

1.1 Background

A ferroelectric is generally defined as a material whose intrinsic lattice polarization can be reversed through the application of an external electric field E that is greater than the coercive field E_c . Ferroelectrics usually have a phase-transition temperature T_c above which they are paraelectric. From their discovery by Valasek in 1920, ferroelectric materials attract more and more interests both in academic and application field. Before 1970, the most exciting challenge in ferroelectrics was modeling ferroelectric phase transitions and discovering new ones [Lines, 1977]. The focus changed after 1984, when thin-film ferroelectrics were developed and first integrated into semiconductor chips [Scott, 1989]. In fact, due to the difficulty in reducing fatigue in the ferroelectric memory device, the progress in this direction has been limited in these years. Besides the application for memory, however, at the same time, all ferroelectrics are also pyroelectric, and all pyroelectrics are piezoelectric. They are widely used for pyroelectric detectors, nonlinear optics, piezoelectric transducers, temperature sensors, magneto-electric transformers and integrated optics.

One application field of ferroelectric materials is waveguide integrated optics. The concept of integrated optics was initially proposed by S. E. Miller of Bell Laboratories in 1969 [Millier, 1969]. Integrated optics is mainly developed in the direction of integration of waveguides and optoelectronic components on a single substrate to achieve creation of multifunctional devices, thus ensuring the advantages of low cost, robustness, compactness, integration and compatibility with microelectronic systems [Palais, 1988]. In order to improve the device performance, the material used for these photonic devices has thus become a critical issue to be considered. Various materials are under investigation for use in integrated optics applications, including polymers, glasses, semiconductors, and ferroelectric materials [Kaminov, 1974; Petraru, 2002; Thapliya, 2003]. Among them, ferroelectric materials with high electro-optic coefficients and good chemical stability are a leading class of materials for integrated optics applications. Significant achievements have been made over the past twenty years in the development of waveguide electro-optic modulator devices [Wang, 1995]. However, many of the above modulators are based on bulk single crystals, there have been few modulators based on ferroelectric thin films. Thin-film waveguide has become a key component in integrated optics, optical communications and optical interconnects. High-quality ferroelectric thin films have advantages over

bulk single crystals because they can operate at a higher modulation frequency and a lower driving voltage and get high confinement efficiency. Many modern thin film technologies have been used to fabricate high quality waveguide structure to make these concepts a reality although there are still many challenges before ferroelectric thin films can be used widely in optical waveguides. The fabrication of ferroelectric thin films by a variety of techniques, including liquid phase epitaxy [Neurgaonkar, 1987], molecular beam epitaxy [Betts, 1985], sol-gel deposited [Zhai, 2001], metal organic chemical vapor deposition (MOCVD) [Moret, 2002], pulsed laser deposition (PLD) [Kim, 1995] and sputtering [Blomqvist, 2003].

Most of ferroelectric materials show good piezoelectric property and are widely used in piezoelectric and related devices. One important application of ferroelectric materials is that it is used as the piezoelectric phase in the multiferroelectric materials. Multiferroic magnetoelectric materials [Fiebig, (2005); Eerenstein, (2006)], which simultaneously exhibit ferroelectricity and ferromagnetism, have recently stimulated an extensive number of research activities for their scientific interest and significant technological promise in the novel multifunctional devices since its appearance in 1972. Natural multiferroic single-phase compounds are rare, and their magnetoelectric responses are either

relatively weak or occurs at temperatures too low for practical applications.

Multiferroic composites, however, incorporating both ferroelectric and ferri-/ferromagnetic phases, typically yield giant magnetoelectric coupling response above room temperature, which makes them ready for technological applications. In such composites the magnetoelectric effect is generated as a product property of a magnetostrictive and a piezoelectric substance. An electric polarization is induced by a weak ac magnetic field oscillating in the presence of a dc bias field, and/or a magnetization polarization appears upon applying an electric field. The elastic coupling interaction between the magnetostrictive phase and piezoelectric phase leads to giant magnetoelectric response of these magnetoelectric composites. Multiferroelectric materials with high Curie temperatures show excellent stability in high temperature though most of them have not as large ME coefficient as that of alloy-piezoelectric multiferroelectrics. In this thesis, one part work was focused on the fabrication and ME properties of the SCNN-CFO multiferroelectric systems.

1.2 Ferroelectric material

1.2.1 History

The ferroelectric effect was first observed by Valasek in 1920 [Valasek, 1920, 1921], in the Rochelle salt which has molecular formula $\text{KNaC}_4\text{H}_4\text{O}_6 \cdot 4\text{H}_2\text{O}$. The effect was then not considered for some time, and it wasn't until a few decades ago that they came into great use. Nowadays, ferroelectric materials are used widely, not only in memory applications, but also in piezoelectric and nonlinear optical applications.

1.2.2 Polarization

Most materials are polarized linearly with external electric field, nonlinearities are insignificant. This behavior is called dielectric polarization (Fig 1.1 (a)). Some materials, known as paraelectric materials, demonstrate nonlinear polarization (Fig 1.1 (b)). The electric permittivity, corresponding to the slope of the polarization curve, is thereby a function of the applied electric field. Ferroelectric materials are also nonlinear and demonstrate a spontaneous polarization (Fig 1.1

(c)). Commonly, materials demonstrate ferroelectricity only below a certain phase transition temperature, while being paraelectric above.

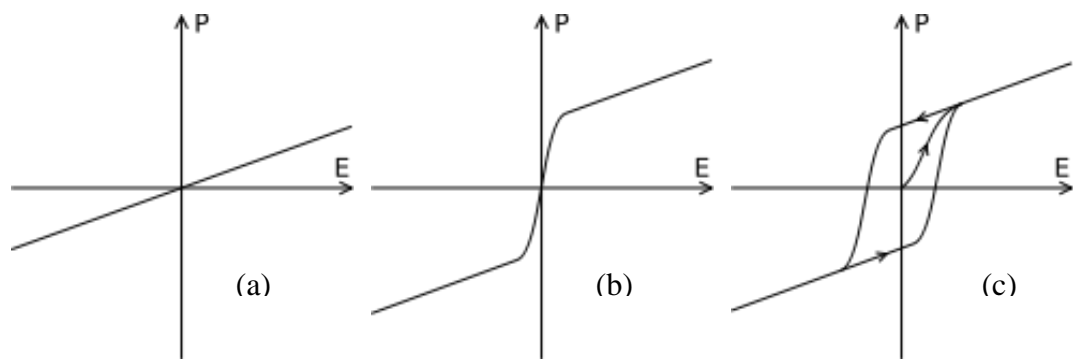


Fig. 1.1 (a) Linear, (b) nonlinear and (c) nonlinear loop relationships of polarization and electric field.

To be ferroelectric, a material must possess a spontaneous dipole moment that can be switched in an applied electric field, i.e. spontaneous switchable polarisation. The electric moment (μ) of a point charge q relative to an arbitrary origin is defined as:

$$\begin{aligned} \mu &= q \cdot r \\ \sum \mu &\neq 0 \end{aligned} \tag{1.1}$$

where charge q is the charge of ions, and r is the position vector from the origin to the charge. In a ferroelectric material, there is a net permanent dipole moment, which comes from the vector sum of dipole moments in each unit cell, $\sum \mu$. In order to let $\sum \mu \neq 0$, ferroelectrics must be non-centrosymmetric. There must also be a spontaneous local dipole moment. This means that the central atom must be in a non-equilibrium position. Polarization is then defined as the total dipole moment per unit volume.

1.2.3 P-E loop

Figure 1.2 shows the origin of the hysteresis loop. The removal of the field will leave some polarization behind (curve C-D-F in the figure), and only when the field is reversed does the polarization start to lessen since new and oppositely poled domains form (F-G). They grow quickly however, giving a large change of polarization for very little change in electric field. But to form an entirely reversed

material, a large switching field is required (G). This is because of both defects in the crystal structure, in a manner similar to Zener drag, and also to do with stray field energy. The polarization of the material goes from a coupled pattern, with 180° boundaries, to a state in which many heads and tails are separated. This leads to the increase in stray field energy. Therefore, to attain this state, lots of energy has to be put in through a large field.

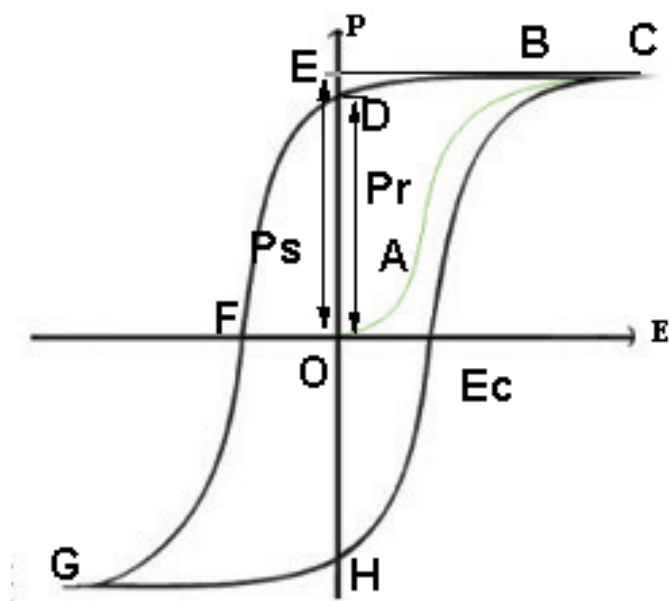


Fig. 1.2 A typical P-E hysteresis loop of ferroelectrics.

1.2.4 Curie temperature

Another important characteristic of the ferroelectrics is the temperature of phase transition, the Curie point T_c . When the temperature is above T_c the crystal does not exhibit ferroelectricity; on the other hand, when the temperature is below T_c , the crystal exhibits ferroelectricity. It is believed that the ferroelectric structure of a crystal is created by a small distortion of the paraelectric structure such that the lattice symmetry in the ferroelectric phase is always lower than in the paraelectric phase.

When the temperature is in the vicinity of the Curie point, thermodynamic properties such as dielectric, electro-optic and thermal properties of a ferroelectric crystal show anomalies and the structure of the crystal changes. So it is valuable to pay attention to the change of physical properties around the Curie temperature of the ferroelectrics. For tetragonal tungsten bronze niobates SCNN and SBN, they show Curie temperature of 279 to 297 °C and 60 to 250 °C, respectively, depending on the composition. Normally the temperature dependence of the dielectric permittivity can be expressed by the modified Curie–Weiss law [Trainer, 2000]:

$$\frac{1}{\varepsilon(f,T)} - \frac{1}{\varepsilon_m(f)} = C[T - T_m(f)]^\gamma \quad (1.2)$$

This equation defines the diffuseness of the relaxor phase transition, where γ ($1 < \gamma < 2$) is a constant which expresses the diffuseness exponent of the phase transition, indicating if the phase transition is or not “completely” diffusive. C is the Curie-Weiss constant, ε_m is the dielectric permittivity maxima and T_m is the temperature at dielectric maxima. When $\gamma = 1$, the material follows an ideal Curie–Weiss law which is validity in case of normal ferroelectrics, whereas $\gamma = 2$ corresponds to a so-called “complete” diffuse phase transition. This method is used to characterize whether one material is relaxor ferroelectric or normal ferroelectric. Most ferroelectrics such as BaTiO₃, TGS (triglycine sulfate) and KDP (potassium dihydrogen phosphate) are normal ferroelectrics. The temperature dependence of their dielectric permittivity displays a sharp and sudden change. Different from normal ferroelectrics, some perovskite type compounds, such as Pb(Mg_{1/3}Nb_{2/3})O₃ and Pb(Sc_{1/2}Ta_{1/2})O₃ and tungsten-bronze type compounds SCNN and SBN, belong to relaxor ferroelectrics, show very broad peak in the temperature dependence of dielectric permittivity [Xu, 1991].

1.3 Tungsten Tetragonal Bronze Niobates Materials

In recent years, increasing attention has been focused on the preparation of dielectric and ferroelectric optical waveguides. The planar waveguide structures have been proposed and demonstrated for many applications, including nonlinear electro-optical devices, electro-optic waveguide modulators and passive integrated optical circuits [Foster, 1993; Kholkin, 1997; Yin, 1998; Wegner, 1991]. Ferroelectric materials have attracted a lot of attention for electrical and optical applications due to their excellent electro-optic properties. From 1960s, lead-free ferroelectric materials of tetragonal tungsten-bronze-structure (TTB) become a family of the most important ferroelectric materials due to their potential applications in various electronic and waveguide devices. In the present study, we focus on the researches of $\text{Sr}_{2-x}\text{Ca}_x\text{NaNb}_5\text{O}_{15}$ (SCNN, $x = 0.05\sim 0.35$) and $\text{Sr}_{1-x}\text{Ba}_x\text{Nb}_2\text{O}_6$ (SBN, $x = 0.25\sim 0.75$). SBN and SCNN belongs to the group of materials possessing a tungsten bronze structure with a general formula $(A_1)_2(A_2)_4C_4(B_1)_2(B_2)_8O_{30}$. As seen in Figure 1.3, this structure is characterized by a network of NbO_6 octahedra, which are connected by the edges to form pentagonal A_2 , tetragonal A_1 , and trigonal C channels. The 12-fold-coordinated A_1 and A_2 positions are occupied only by a divalent or monovalent metal ion such as Sr, Ba, Ca and Na, the B positions are occupied by either Nb or Ta, and the C positions are

occupied by very small metal ions, for example, Li ions or remain empty. The crystal symmetry is tetragonal $4/mmm$ above T_m and remains tetragonal ($4mm$) below T_m , where T_m is the temperature where dielectric constant is the largest. Through changing the ratio of irons in A sites, we can change the related properties such as Curie temperature, E-O coefficient, pyroelectric coefficient of the crystal. For example, for SBN, the Curie temperature, dielectric constant in room temperature, pyroelectric coefficient and E-O coefficient r_{33} changes from 250 to 60 °C, 3400 to 118, $31.0 \cdot 10^{-2}$ to $3.0 \cdot 10^{-2}$ $\mu\text{C}/\text{cm}^2\text{K}$ and 1380 to 41 with x changing from 0.25 to 0.75 [Xu, 1991]. Table 1.1 lists some main electric and optical parameters of the SBN25, SBN50 and SBN 75. LiNbO_3 , as an industry standard, is used as a reference.

Property	unit	x=0.75	x=0.5	x=0.25	LiNbO ₃
Effective EO coefficient γ_c	(10 ⁻¹² m/V)	41	205	1380	19
Half-wave voltage	kV	1.34	0.25	0.037	2.8
Refractive index n_o		2.3144	2.3123	2.3117	2.286
index n_e		2.2596	2.2734	2.2987	2.200
Dielectric constant ϵ		118	450	3400	30
Pyroelectric coefficient	(10 ⁻¹² μ C/cm ² K)	3.0	8.2	31.0	

Table 1.1 Electric and optical properties of SBN.

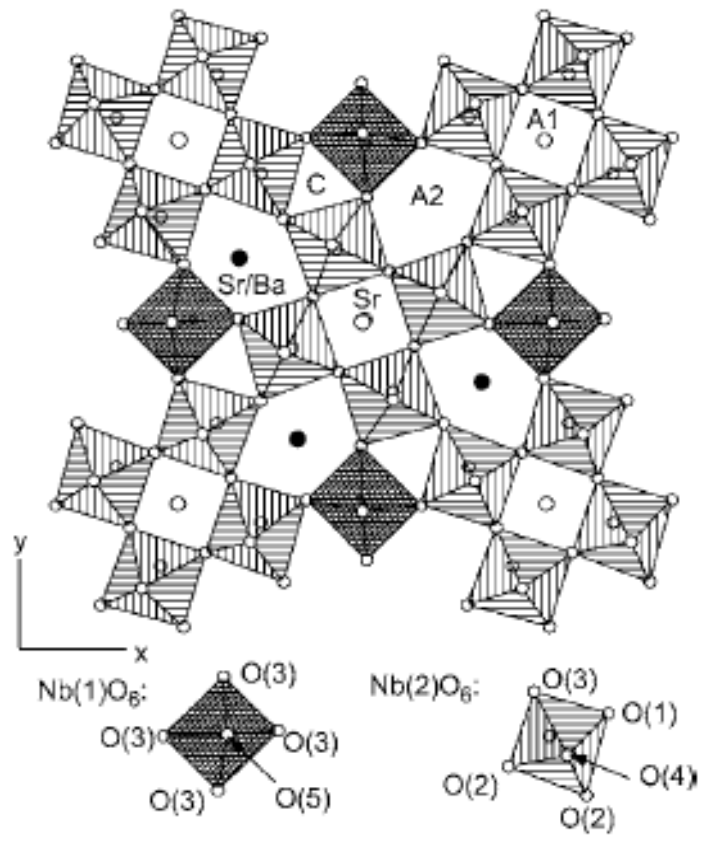
x	0.05	0.1	0.2	0.35	[Xie,2002]
T_c (°C)	279	285	287	297	
T_s (°C)	-11	0	7	2	
ϵ at T_c	1353	1140	793	543	
$\tan \delta$ at T_c (%)	4.9	3.4	3.9	5.3	
P_r ($\mu\text{C}/\text{cm}^2$)	2.7	2.9	2.2	1.10	
P_s ($\mu\text{C}/\text{cm}^2$)	7.4	7.4	8.0	0	
E_c (kV/cm)	12.4	10.4	10.2	0	
Pyroelectric coefficient at 20 °C ($\mu\text{C}/\text{cm}^2 \cdot ^\circ\text{C}$)		0.092			[Neurgaonkar, 1988]
Electro-optic coefficient (10^{-12} m/V)		1325			

Table 1.2 Electric and optical properties of SCNN.

For SCNN, the Curie temperature and dielectric constant in room temperature changes from 279 to 297 and 1353 to 543 in the x range of 0.05 to 0.35, respectively. Some main dielectric and ferroelectric parameters are listed in table 2. SCNN shows similar ferroelectric and electro-optic coefficients with SBN. But due to the introduction of Na iron in the void site, SCNN shows much higher Curie temperature than that of SBN [Xie, 2002]. Unfortunately, there are not enough optical parameter data such as E-O coefficient, refractive index and optical propagation loss in literature.

It should be noticed that in both SBN and SCNN, the sites are not fully filled for example, the small C site is empty, and in SBN, only 5 Sr^{2+} and Ba^{2+} ions are occupying the 6 A_1 and A_2 sites. Thus, it is possible to modify the optical properties of the materials through doping some metal ions to the empty site. In the past twenty years, much work was done in this field. Rakuljic et.al investigated the increased photorefractive properties of Ce and Fe doped SBN single crystals in 1986 [Rakuljic, 1986]. Liang. *et.al.* holographic recording with orthogonally polarized beams in a cesium-doped $(\text{K}_{0.5}\text{Na}_{0.5})_{0.2}(\text{Sr}_{0.75}\text{Ba}_{0.25})_{0.9}\text{Nb}_2\text{O}_6$ crystal [Liang, 2001]. Chen H et. al. found that the photorefractive properties of KNSBN can be further increased and can be used to make self-pump phase conjugate

device by Cu-doping [Chen,1997]. In the present work, we focus on the measurements of EO and magneto-electric properties, and fabrication of waveguide structure. Among SBN and SCNN, SCNN is the main material that we have focused on due to its higher Curie temperature.



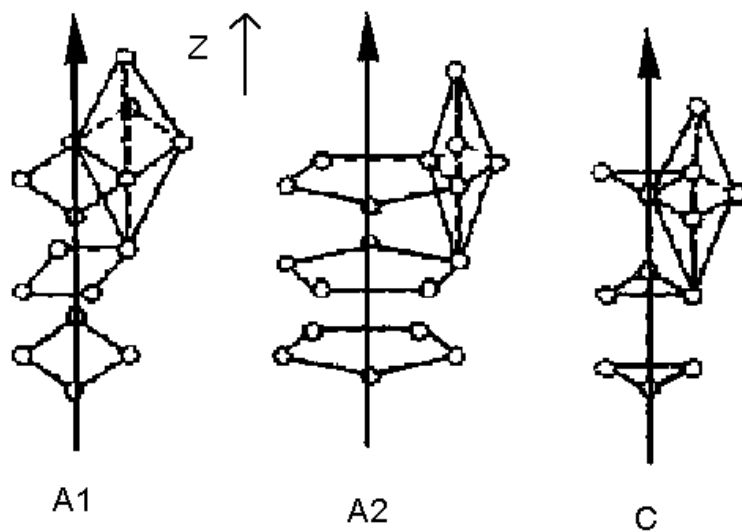


Fig. 1.3 Projection of $\text{Sr}_{0.61}\text{Ba}_{0.39}\text{Nb}_2\text{O}_6$ along the c axis.

1.4 Optical waveguide

1.4.1 Background

The intense developments in the new devices and in the applications of thin films in optics and electronics have stimulated investigations to improve the existing methods of measuring thin film parameters and develop new measurement techniques. Usage of waveguide propagation phenomena of light in thin films makes it possible to create non-destructive diagnostic techniques with high resolution that maintains the integrity and the quality of the investigated sample. It also allows one to directly measure the film's refractive index, thickness and optical propagation loss. The existing methods of direct measurements of the thin film parameters require either the destruction of the investigated sample or results in less accurate characterization of the thin films. In this project, a prism coupler technique was used to measure the waveguide properties of ferroelectric waveguide thin films. This technique is based on the principles of spatial Fourier spectroscopy of the reflected light beam when the guided mode is excited in thin film structure by prism coupler, i.e., they are based on the recording of the spatial spectrum of the intensity of the light beam reflected from a prism coupler [Stoll, 1973]. In this approach, the advantages of the resonant and interference

measurement techniques are incorporated, and consequently, the methods considered here has very high sensitivity and resolution.

1.4.2 Optical waveguide theory

In this thesis, we focus on the research of the planar film waveguide. In a thin film waveguide (Fig. 1.4) the refractive index n_f of the guiding layer is normally greater than the refractive index of substrates n_s and the refractive index n_c (normally it is air) of the surrounding medium. This condition is necessary to provide the waveguiding regime, i.e. for the existence of optical guided modes in the waveguide structure. In the case of the reflection of wave from the medium with lower optical density ($n_s < n_f$) at the incidence angle which is greater than some angle ϕ_c (satisfying the condition $\sin \phi_c = \frac{n_s}{n_f}$), the reflection coefficient $r=1$ is always satisfied. This phenomenon is referred to as total internal reflection. The reflection coefficient r , has two different values, depending on the polarization. Here, r_{TE} and r_{TM} are given by:

$$r_{TE} = \frac{\cos \phi - \frac{n_s}{n_f} \cos \theta}{\cos \phi + \frac{n_s}{n_f} \cos \theta}$$

$$r_{TM} = \frac{\cos \theta - \frac{n_s}{n_f} \cos \phi}{\cos \theta + \frac{n_s}{n_f} \cos \phi} \quad (1.3)$$

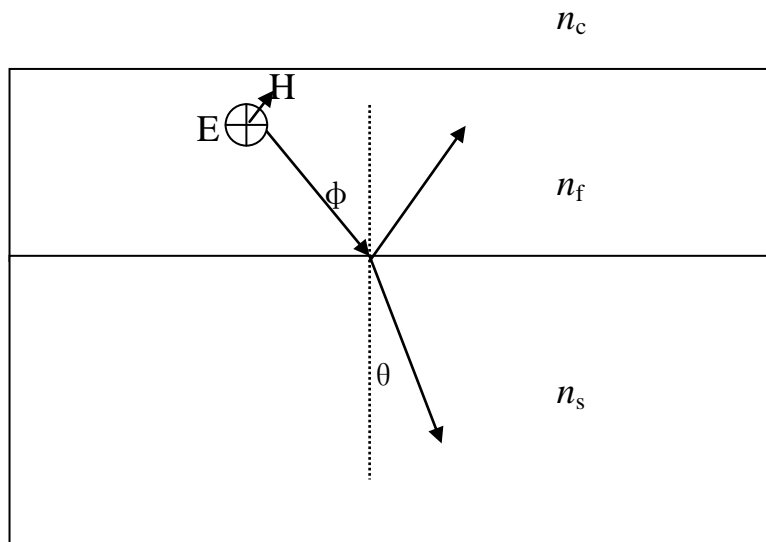


Fig. 1.4 Schematic of planar waveguide and reflection of the plane TE-wave

From the viewpoint of ray optics, the waveguide propagation of radiation in the waveguide layer can be interpreted with the help of total internal reflection

phenomenon. The angle of reflection θ_m is different for each plane wave and this leads to difference in the phase velocity. The propagation of plane waves can be described in term of propagation constants [Prokhorov, 1996]:

$$\begin{aligned} f &= a \exp(iux + ihz - i\omega t) \\ g &= b \exp(-iux + ihz - i\omega t) \end{aligned} \quad (1.4)$$

where $h = k_0 n \sin \alpha$ is a longitudinal propagation constant, $u = k_0 n \cos \alpha$ is the transverse propagation constant, with $\alpha = (\pi/2 - \theta_m)$. In the case of total reflection, the amplitudes of incident and reflected waves should satisfy the following relationship:

$$\begin{aligned} g &= f \exp(-2i\delta_1) \\ f &= g \exp(-2i\delta_2) \end{aligned} \quad (1.5)$$

where δ_1 and δ_2 are phase jumps at the upper and lower interfaces, respectively,

$$\begin{aligned} \delta_1 &= \arctan \sqrt{\frac{(h/k_0)^2 - n_c^2}{n^2 - (h/k_0)^2}} \\ \delta_2 &= \arctan \sqrt{\frac{(h/k_0)^2 - n_s^2}{n^2 - (h/k_0)^2}} \end{aligned} \quad (1.6)$$

The phase relations mentioned above are satisfied at the condition

$$k_0 n d \cos \alpha - \delta = m \pi$$

therefore, the light propagation in thin film takes place only for a discrete series of incidence angles, being greater than the critical angle of total reflection, although the total reflection is observed at any angle $\theta > \theta_c$.

The characteristics or dispersion equations for TE and T modes can be found from Maxwell equations and boundary conditions:

$$k_0 d \sqrt{n^2 - (h/k_0)^2} = \arctan \sqrt{\frac{(h/k_0)^2 - n_c^2}{n^2 - (h/k_0)^2}} + \arctan \sqrt{\frac{(h/k_0)^2 - n_s^2}{n^2 - (h/k_0)^2}} + m \pi \quad (1.7)$$

$$k_0 d \sqrt{n^2 - (h/k_0)^2} = \arctan \frac{n^2}{n_c^2} \sqrt{\frac{(h/k_0)^2 - n_c^2}{n^2 - (h/k_0)^2}} + \arctan \frac{n^2}{n_s^2} \sqrt{\frac{(h/k_0)^2 - n_s^2}{n^2 - (h/k_0)^2}} + m \pi$$

where $k_0 = 2\pi/\lambda$, m is the mode order, and d the thickness of waveguide.

All guided modes have a definite critical thickness, i.e. the waveguide effect can be observed only when the film thickness is greater than some minimum value d_{\min} (which is referred to as the ‘cut-off’ condition). It is defined by the condition of

total internal reflection at the interface of the guiding layer and the substrate. For

$h = k_0 n_s$, it is possible to derive the following relationship from (1.7):

$$d_{\min}^{(TE)} = \frac{1}{k_0 \sqrt{n^2 - n_s^2}} \left(\arctan \sqrt{\frac{n_s^2 - n_c^2}{n^2 - n_s^2}} + m\pi \right)$$

$$d_{\min}^{(TM)} = \frac{1}{k_0 \sqrt{n^2 - n_s^2}} \left(\arctan \frac{n^2}{n_c^2} \sqrt{\frac{n_s^2 - n_c^2}{n^2 - n_s^2}} + m\pi \right) \quad (1.8)$$

It follows from (1.7) that the minimal layer thickness, required for waveguide propagation of light in the layer, depends on the difference between refractive index of the substrate and the surrounding. Large difference of between refractive index of the substrate and film helps to form waveguide propagation. For the excitation of guided modes, directed by the film, the experimental techniques that use a prism coupler (see Fig1.5) of a tunnel excitation of modes are employed. The condition of the phase synchronization can be easily satisfied with help of the prism coupler:

$$h_m = k_0 n_p \sin \gamma_m \quad (1.9)$$

where γ_m is the incidence angle of radiation on the prism base and n_p is the

refractive index of the prism. In the mode angle ϕ_m , the laser energy can tunnel into the guided mode. It must follow the following condition [Ulrich, 1973]:

$$h = k_0 n_p \sin(\theta_p - \arcsin \frac{n_c \sin \phi_m}{n_p}) \quad (1.10)$$

where θ_p is an angle at the prism base, ϕ_m is the mode angle. At last, using equations (1.10), (1.7) and (1.8), we can calculate the refractive index and thickness of waveguide film using the measured two or more data of mode angle ϕ_m . Using the couple prism method, not only the refractive index and thickness can be measured, but also the EO and thermal-optical properties can be investigated through measuring the temperature and electric field dependence of the refractive index.

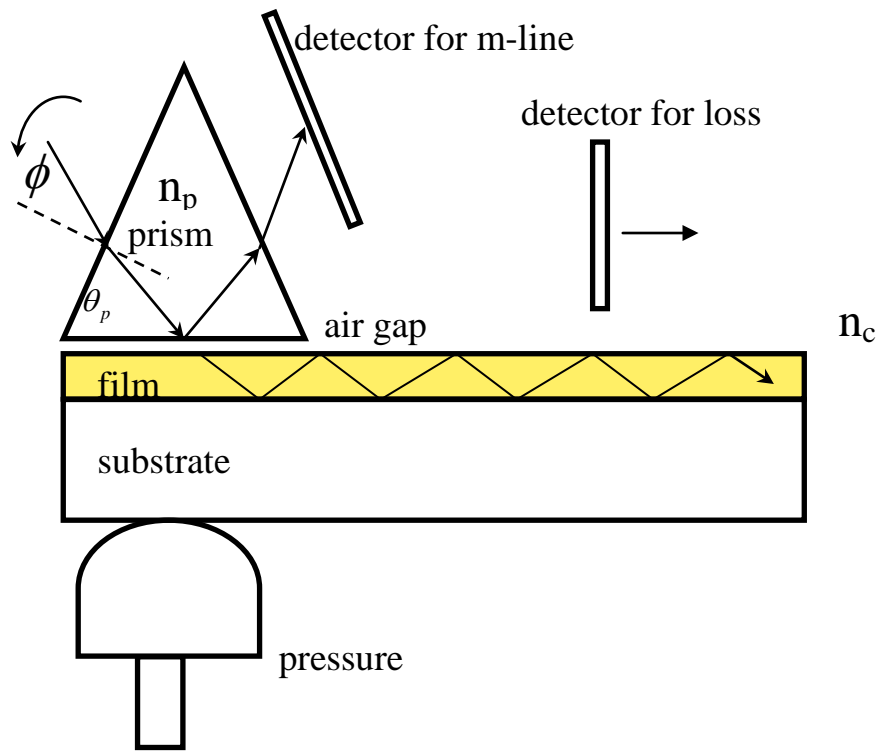


Fig. 1.5 Schematic diagram of the prism coupler.

The techniques of determination of losses in waveguides are based on the input of the definite light power into this film and following the measurement of power at the output of the waveguide. One of the simplest and most precise method is based on focusing the light on the face of the waveguide and further move the detector to measure the optical intensity at different distance.

$$tg\beta = \ln(P_1 / P_2)(l_2 - l_1) \quad (1.11)$$

where P_1 and P_2 are the radiation power at the output of waveguide with length l_2 and l_1 , respectively [Khomchenko, 2005].

1.5 Electro-Optic effect

1.5.1 Refractive index

The refractive index of an isotropic material is defined as:

$$n = \frac{c_0}{c} \quad (1.12)$$

where c_0 is the speed of light in vacuum and c is the speed of light in the material [Nye, 1976]. Here following Maxwell's equations:

$$c = c_0 / \sqrt{\varepsilon} \quad (1.13)$$

where ε is the relative permittivity at optical frequency. So refractive index can be expressed as:

$$n = \sqrt{\varepsilon} \quad (1.14)$$

1.5.2 Optical Birefringence

In an anisotropic medium, Maxwell's equations show that not one but two light waves, of different velocities, may in general be propagated through the medium with a given wave normal; moreover, these waves are plane polarized. The refractive indices of the two waves as functions of the direction of their common wave vector k are obtained by drawing an ellipsoid known as the indicatrix. If x, y, z are the principal axes of the relative permittivity tensor, the indicatrix is defined by the equation:

$$\frac{x^2}{n_1^2} + \frac{y^2}{n_2^2} + \frac{z^2}{n_3^2} = 1 \quad (1.15)$$

where $n_1 = \sqrt{\epsilon_x}$, $n_2 = \sqrt{\epsilon_y}$, $n_3 = \sqrt{\epsilon_z}$ and $\epsilon_x, \epsilon_y, \epsilon_z$ are the principal relative permittivities.

The optical properties of a crystal are closely related to its crystal symmetry. For a cubic crystal, such as MgO, the indicatrix is a sphere and all central sections are circles, thus $n_1=n_2=n_3$. For hexagonal, tetragonal and trigonal crystals, the indicatrix is necessarily an ellipsoid of revolution about the principal symmetry axis z . The principal axis is called the optic axis and the crystal are said to be

uniaxial. $n_o = n_1 = n_2$ and $n_e = n_3$ are the ordinary and extraordinary refractive indices, respectively. The difference between the two indices, $\Delta n = n_o - n_e$, is called the birefringence. Tungsten bronze SCNN and SBN belong to tetragonal structure crystals, the refractive indices of the epitaxial or high oriented films measured by the prism coupler method using two different polarized lasers TE and TM are different, this is the birefringence.

1.5.3 Electro-optic effect

Generally, the origin of the EO effect of the TTB SBN or SCNN induced by the applied electric field is closely related to the electric field-induced unit cell structure change. The electro-optic (E-O) effect refers to the change of optical refractive index in the crystal due to the presence of electric field. With the knowledge of the general optical indicatrix of the crystal, an understanding of the electro-optic effect can be realized. The equation of the indicatrix is generally modified to:

$$\eta_{11}x^2 + \eta_{22}y^2 + \eta_{33}z^2 + \eta_{12}xy + \eta_{23}yz + \eta_{13}xz = 1 \quad (1.16)$$

where η_{ij} is the impermeability tensor which is related to the relative permittivity tensor:

$$\eta_{ij} = [\varepsilon^{-1}]_{ij} \quad (1.17)$$

Due to the presence of external electric field \mathbf{E} , the distribution of the charges in the crystal changes, resulting in a change of the impermeability tensor $\Delta\eta_{ij}$:

$$\Delta\eta_{kj} = \sum_k r_{hjk} E_k + \sum_{km} R_{hijk} E_k E_m \quad (1.18)$$

where the first term and second term are called the linear electro-optic effect (Pockels effect) and quadratic electro-optic effect (Kerr effect), respectively. Since η_{hj} is a symmetric tensor, $r_{hj} = r_{jh}, r_{ik}$, in which each subscript set hj and jh is replaced with a subscript i in the following relation:

$$hj = 11 \rightarrow 1,22 \rightarrow 2,33 \rightarrow 3,23or32 \rightarrow 4,13or31 \rightarrow 5,12or21 \rightarrow 6 \quad (1.19)$$

In non-centrosymmetric crystals, such as tetragonal materials, application of the electric field leads to a linear perturbation of the refractive index so that the

linear electro-optic effect is dominant. When only the linear E-O effect is considered, the change in the impermeability $\Delta\eta_{ij}$ induced by an electric field $\mathbf{E} = (E_x, E_y, E_z)$ can be expressed as:

$$\begin{bmatrix} \eta_{11} \\ \eta_{22} \\ \eta_{33} \\ \eta_{23} \\ \eta_{13} \\ \eta_{12} \end{bmatrix} = \begin{bmatrix} r_{11}, r_{12}, r_{13} \\ r_{21}, r_{22}, r_{23} \\ r_{31}, r_{32}, r_{33} \\ r_{41}, r_{42}, r_{43} \\ r_{51}, r_{52}, r_{53} \\ r_{61}, r_{62}, r_{63} \end{bmatrix} \begin{bmatrix} E_x \\ E_y \\ E_z \end{bmatrix} \quad (1.20)$$

where the 6×3 matrix (r_{ik}) is called the electro-optic tensor. For various crystals, due to the crystal symmetry, some of the E-O coefficients may be zero and some of them may be equal in value (or opposite in sign) [Yariv, 1984]. For example, in tetragonal crystal with the point group of 4mm, it has an electro-optic tensor of the form:

$$\begin{bmatrix} \eta_{11} \\ \eta_{22} \\ \eta_{33} \\ \eta_{23} \\ \eta_{13} \\ \eta_{12} \end{bmatrix} = \begin{bmatrix} 0, 0, r_{13} \\ 0, 0, r_{13} \\ 0, 0, r_{33} \\ 0, r_{51}, 0 \\ r_{51}, 0, 0 \\ 0, 0, 0 \end{bmatrix} \begin{bmatrix} E_x \\ E_y \\ E_z \end{bmatrix} \quad (1.21)$$

It is often possible to avoid the complication of the cross-terms by applying the external field parallel to one of the principal axes of the crystal. Applying the electric field along the z -axis of a uniaxial crystal ($\mathbf{E} = (0, 0, E)$), Eqs (1.6) and (1.9) reduce to:

$$\left(\frac{1}{n_o^2} + r_{13}E\right)(x^2 + y^2) + \left(\frac{1}{n_e^2} + r_{33}E\right)z^2 = 1 \quad (1.22)$$

In this case, the principal axes of the indicatrix only change their lengths, while the indicatrix is not rotated (no cross terms are included). Therefore eqt (1.22) is simplified to:

$$\begin{aligned} \frac{1}{n_o^2(E)} &= \frac{1}{n_o^2} + r_{13}E \\ \frac{1}{n_e^2(E)} &= \frac{1}{n_e^2} + r_{33}E \end{aligned} \quad (1.23)$$

Assuming that the $r_{13}E_z \ll n_o^{-2}; r_{33}E_z \ll n_e^{-2}$ and using the differential equation

$$dn = -\left(\frac{n^3}{2}\right)d\left(\frac{1}{n^2}\right), \text{ Thus, we get}$$

$$\begin{aligned}
n_o(E) - n_o &= -\frac{1}{2}n_o^3 r_{13} E \\
n_e(E) - n_e &= -\frac{1}{2}n_e r_{33} E
\end{aligned}
\tag{1.24}$$

The electric field induced birefringence can be written as:

$$n_o(E) - n_e(E) = \frac{1}{2}n_e^3 E \left[r_{33} - \left(\frac{n_o}{n_e} \right)^3 r_{13} \right] = \frac{1}{2}n_e^3 r_c E
\tag{1.25}$$

where r_c is the effective electro-optic coefficient, given by:

$$r_c = r_{33} - \left(\frac{n_o}{n_e} \right)^3 r_{13}
\tag{1.26}$$

In general, the electro-optic behavior of a material can be characterized by effective electro-optic coefficients.

1.6 Scope of the Present Study

The main objective of the present research is to fabricate and characterize TTB structure SCNN and SBN thin films and to study their potential use as waveguiding and magneto-electric materials. The thesis consists of seven Chapters. Following the introduction given in this Chapter, the fabrication of SCNN and SBN thin films by pulsed laser deposition and some characterization methods of these films are described in Chapter 2. Using the optimum conditions (substrate temperature and oxygen partial pressure), high quality and transparent SCNN and SBN thin films have been deposited on MgO (100) and fused quartz substrates.

In Chapter 3.1, the prism coupler technique is employed to characterize the optical waveguiding properties of polycrystalline and epitaxial SCNN thin films. The relationship of microstructure and waveguiding properties including the refractive indices, refractive index profile (refractive index as a function of depth) and optical loss was investigated.

Chapter 3.2 describes the fabrication and waveguiding properties of the epitaxial SCNN thin films integrated on MgO/TiN or In:c-MZO/TiN buffered Si(100) substrate.

In Chapter 3.3, the thermo and electric field dependence of the refractive index of the SCNN and SBN thin films are investigated using the prism coupler technique.

In Chapter 4, thermo-Raman is used to investigate the phase transition of the epitaxial SCNN and SBN thin films. Temperature controlled Brillouin light scattering is used to study the dynamical property of polarization nano regions (PNRs) of the SCNN film on Si substrate.

Chapter 5 introduces the magneto-electric and dielectric relaxor properties of the SCNN/CFO composite ceramic.

Chapter 6 introduces fabrication and characterization of TTB SBN nanocrystals.

Conclusions and suggestions for future work are given in Chapter 7.

1.7 Statement of Original Contributions

To the best of my knowledge, the present work has made the following original contributions:

1. The optical properties including refractive indices, refractive index profile and optical loss in polycrystalline and epitaxial SCNN thin films of SCNN thin films were investigated systematically using the prism coupler technique. A low optical loss at $\lambda = 632.8$ nm was observed, which is within the acceptable range for optical guided wave devices. The epitaxial structure was proved to play a key role in reducing the optical propagation loss. It was suggested that the SCNN films are promising waveguiding materials for practical integrated optical devices.
2. A simple, direct and reliable technique based on the shift of the synchronous angles of the guided modes as a function of applied electric field was used to investigate the effective electro-optic and thermo-optical coefficient. We demonstrate that this technique is convenience in studying the electro-optic and thermo-optical properties for thin films.

3. Many interesting phenomena in the phase transition period were observed in the temperature dependence of Raman spectra. The temperature dependences of peak position and FWHM of the Raman bands present clear anomalies near the phase transition both in SCNN and SBN films. It is believed that the changes of symmetry of the Nb ion in the NbO₆ octahedral are responsible for the observed change of Raman spectrum.

4. We reported, for the first time, the Brillouin scattering study in detail of highly *c*-oriented SCNN films on Si (100) substrate over a wide temperature range. One phase transition from ferroelectric to paraelectric at 290 °C has been clearly observed upon heating process through acoustic modes of both the frequency shift and hypersonic damping. A relaxational mode is found in the form of a central peak. The relaxation time τ of the mode has a temperature dependence similar to that of dielectric constant and shows a broad peak anomaly around T_m .

5. One novel magneto-electric composite system with SCNN as ferroelectric member and CoFeO₂ as ferromagnetic member was fabricated and its ME and dielectric relaxor properties were investigated for the first time. This

composite exhibits a significant ME effect and a remarkable dielectric constant dispersion with Curie temperature of 270 °C.

6. Pure TTB structure SBN nanocrystals with a nanorod-like shape were successfully synthesized through a simple and convenient Pechini route.

2 Film fabrication and characterization

2.1 Pulsed laser deposition

In the past decades, TTB structure niobates thin films have been successfully grown on various substrates via different deposition techniques, including pulsed laser deposition (PLD) [Parviz Tayebati, 1996; Zhu, 1997], rf magnetron sputtering [Yang, 2000], sol-gel deposition [Junmo, 2003; A.Y. Oral, 2000] and metalorganic chemical vapor deposition (MOCVD) [Nystrom, 1995]. Among them, PLD is the most extensively used technique for growing epitaxial TTB niobates thin films. Pulsed laser deposition is chosen in this study because it can not only provide good stoichiometric control of films but also fabricate highly oriented thin films.

2.1.1 Introduction

Pulsed laser deposition (PLD) process adopts focused high-power pulsed laser beam, which is directed into a chamber and impacted onto a target. The target surface, absorbing the high energy, will be transformed into high

kinetic-energy plasma, and then evaporated. Due to the non-equilibrium deposition, the material composition of thin films and target are almost the same, especially for multi-component materials or doped materials. The thickness of thin films can be precisely controlled by the laser counts. Hence, the thin films grown by PLD demonstrate excellent epitaxial characters.

Most of the films in this report were fabricated by pulsed laser deposition (PLD) . There are numerous methods to fabricate thin films such as thermal evaporation, magnetron sputtering and chemical vapor deposition (CVD). However, PLD offers a number of advantages. It allows ‘congruent’ deposition. It means that the stoichiometry of multi-component elements can be preserved in the deposited films. It is also suitable to grow multiple materials films. Multiple targets can be loaded inside the deposition chamber on a rotating holder thereby enabling the in-situ growth of heterostructure. Another advantage of PLD is that it can be used to fabricate epitaxial films. The most important advantage is that it can be used to fabricate most of materials, so that normally it is used to fabricate new material. However, it also has some disadvantages. The most important one is that it is not suitable to be used to fabricate films with large areas, so that it is normally used to fabricate films only in fundamental research field but not in industry. It is also difficult to deposit thick film using PLD. Another intrinsic disadvantage is

that PLD derived films normally contain some micro-sized particles. In the case of this project, it is suitable to fabricate SCNN and SBN films using PLD.

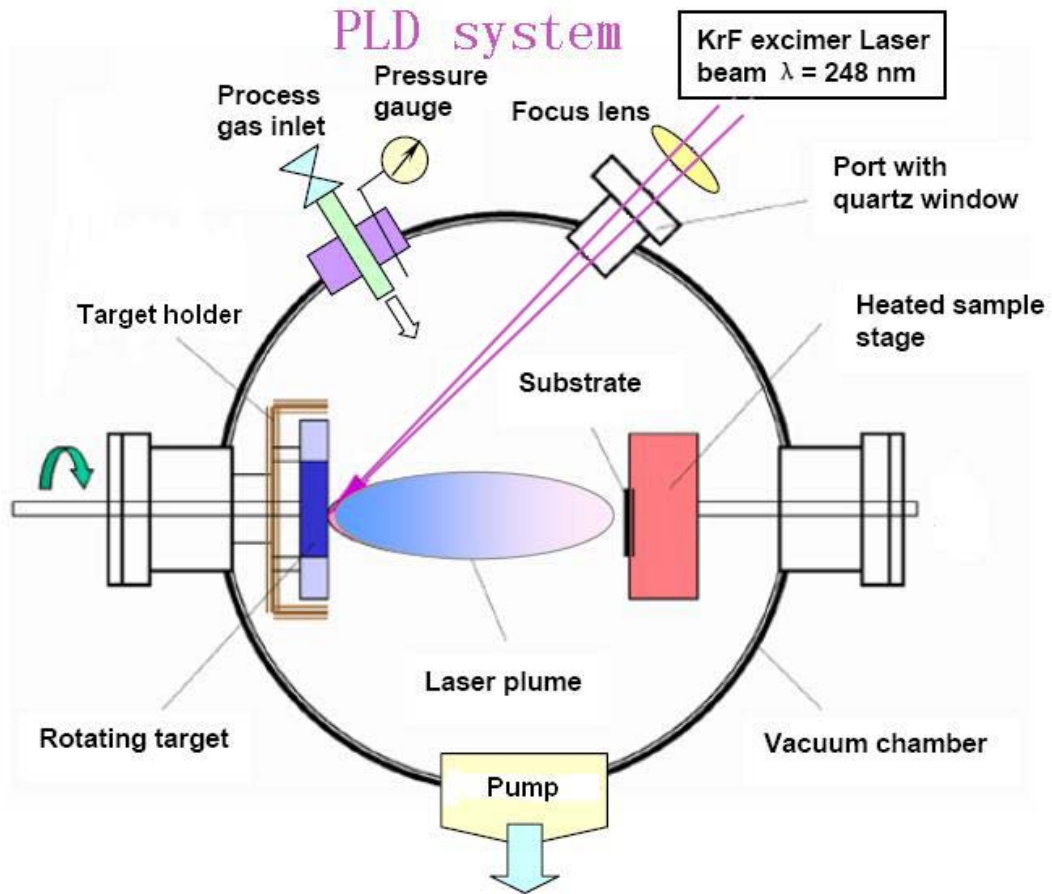


Fig. 2.1 A schematic diagram of the PLD system used in our laboratory.

A schematic diagram of the PLD system used in our laboratory is shown in Fig. 2.1. It consists of a target holder and a heated substrate stage housed in a vacuum chamber. Laser pulses are focused through an optical system onto the target. In order to achieve high photon absorption by the oxide target, UV

wavelengths are preferred. The laser used is a KrF excimer laser with a wavelength of 248 nm and pulse duration of 25 ns (Lambda Physik COMPex 205).

2.1.2 Film deposition

SCNN targets were prepared by conventional ceramic process using analysis grade SrCO_3 , CaCO_3 , NaHCO_3 , and Nb_2O_5 (Aldrich, USA) powders as starting materials. These powders were weighted according to the molecular formula of relate composition SCNN and subsequent ball-milled for 12 h. After being calcined at $1200\text{ }^\circ\text{C}$ for 6 h, the mixed powder was pressed into disk pellets and sintered at $850\text{ }^\circ\text{C}$ for 2 h and then at $1330\text{ }^\circ\text{C}$ for 6 h. Figure 2.2 shows the θ - 2θ XRD pattern of the SCNN 19 target. All the peaks are consistent with a tetragonal tungsten bronze phase and no other impurity phases were found.

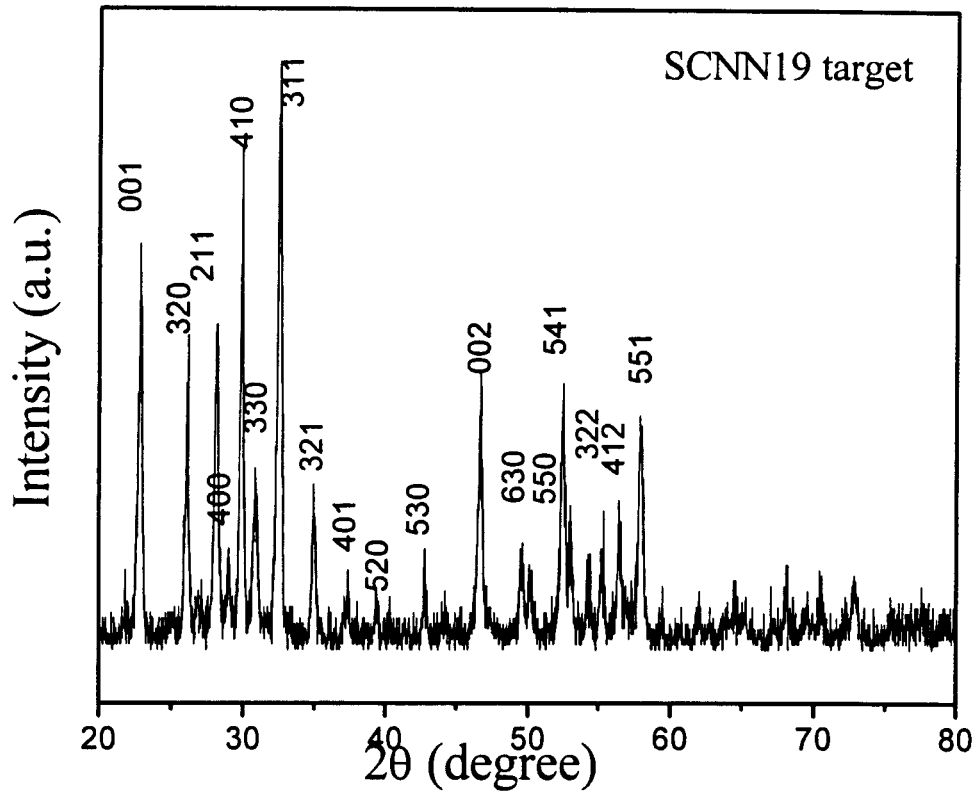


Fig. 2.2 θ - 2θ XRD pattern of SCNN 19 target.

In this thesis, unless special mention, all films were deposited under conditions summarized in Table 2.1. A laser fluence of 180-260 mJ and a repetition rate of 1~10 Hz were used throughout the experiments. Deposition was performed in a vacuum chamber that was evacuated to a base pressure of 5 mTorr and then filled back with oxygen. The laser beam entered the vacuum chamber through a quartz window and was directed towards the solid target. The interaction

of the pulsed laser beam with the target produced a plume of the target material containing energetic neutral atoms, ions and molecules, which were subsequently transported toward a substrate placed directly in line with the plume. The plasma reached the substrate and a thin film was formed. Since sufficient ionic mobility is needed for the growth of epitaxial oxide thin films, the substrate was kept at a high temperature during deposition. Here, the films were grown on MgO (001), fused quartz and Si(100) substrates, which were mounted on a substrate holder with a resistive heater capable of heating the substrate up to 760 °C. The substrate temperature was determined by a thermal couple embedded in the substrate holder. After deposition, the samples were kept in chamber at the growth temperature and 10 Torr oxygen ambience for approximately 20 min. The films were then cooled to room temperature at the same oxygen ambience to avoid oxygen deficiency. In our studies, various temperatures (650–740 °C) and oxygen pressures (50–200 mTorr) were employed. Deposition time was controlled to be 20-60 minutes to obtain films with different thicknesses.

Temperature	500-750 °C
Laser energy	250 mJ
Oxygen pressure	160 mTorr
Distance from target to substrate	4.5 cm
Deposit time	20-60 min
Substrate	Si (100) MgO(100) Fused quartz

Table 2.1 PLD growth conditions

In our study, the deposited films have been characterized using several techniques to yield information on their structural, optical, magnetic and electrical properties. The crystal structure of the deposited films was characterized by a four-circle X-ray diffractometer (Philips, X'pert) with Cu K_{α} radiation operated at an acceleration voltage of 50 kV. The surface morphology of the films were characterized by Atomic force microscopy (AFM, Nanoscope IV, Digital

Instruments) and Scanning Electron Microscopy (SEM, Leica, Stereoscan 440). The optical transmittance measurements were carried out by a two-beam spectrophotometer (Shimadzu UV-2101). The optical waveguide properties were examined by a prism coupler method (Model 2010 prism, Metricon, USA) using a 632.8 nm laser beam. Raman spectroscopy and Brillouin Light Scattering were used to investigate the phase transition of the fabricated films. The capacitance-frequency (C-F) and capacitance-temperature (C-T) characteristics of Pt/SCNN/LNO/MgO were measured using an Agilent HP4294A impedance analyzer and computer assisted HP4194A impedance analyzer, respectively. The ferroelectric hysteresis loop was characterized using a ferroelectric test tower (RT66A, Radiant Technologies). The magnetic properties of the samples were measured using a vibrating sample magnetometer (VSM).

2.2 Relationship of deposition conditions and structural and surface morphology of SCNN thin films

In PLD process, deposition temperature has been found to have a significant effect on the crystalline growth of ferroelectric oxide thin films. We have investigated the structure of SCNN thin films deposited at substrate temperatures ranging from 400 °C to 750 °C.

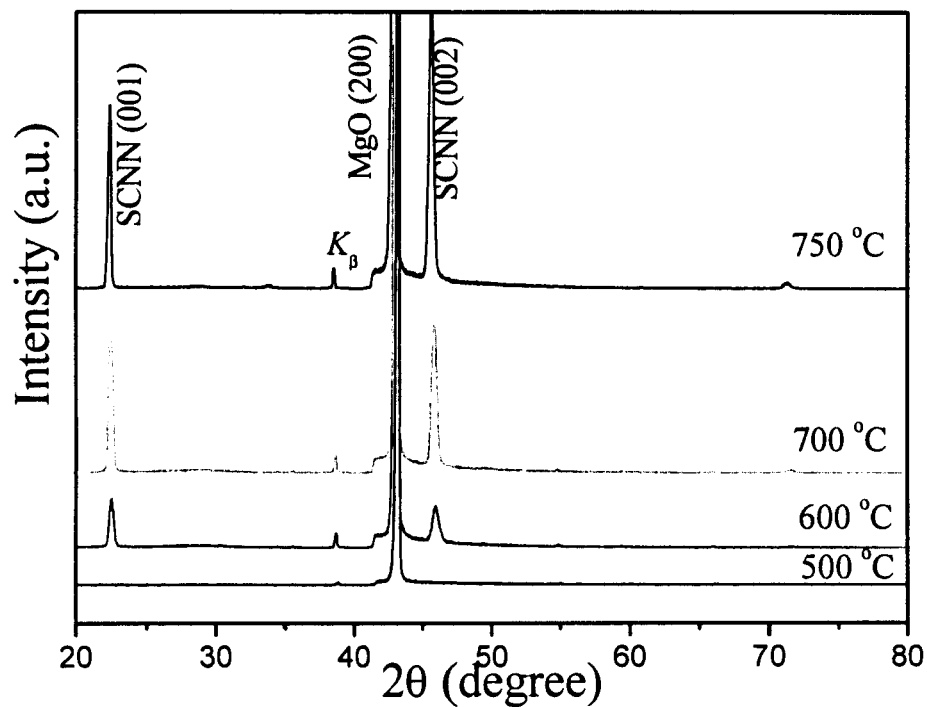


Fig. 2.3 XRD θ - 2θ scan patterns of SCNN thin films deposited on MgO (100) substrates at different temperatures.

Figure 2.3 shows the θ - 2θ scan patterns of SCNN thin films deposited at different temperatures. At temperatures higher than 600 °C, the as-grown SCNN film presents crystalline state. Only the (00 l) peaks are observed, which implies that, in a broad range of deposition temperature, SCNN films deposited on MgO substrates are highly c -axis oriented. One important feature is that the intensity and sharpness of the SCNN (002) peaks increase with the increase of deposition temperature, indicating higher crystalline quality at higher deposition temperatures, as shown in Fig. 2.4.

The grain orientation is a key factor which has been known to be correlated with the optical loss of thin film waveguides [Kang, 1998; Liu, 2006]. Therefore, the grain orientation must be controlled in order to avoid high optical losses due to light scattering at grain boundaries. The degree of grain misorientation in our SCNN thin films was evaluated by measuring the FWHM of the ω -scan of the (002) diffraction peak, as shown in Fig. 2.4. It shows that the FWHM drops substantially with the increase of deposition temperature. The highest degree of grain orientation with the smallest FWHM value was achieved in the SCNN film deposited at 750 °C, which has a FWHM of 0.86°. Figure 2.5 shows surface morphologies of SCNN films deposited at different temperature. Very small

grains appear with the temperature above 500 °C and then the grains grow with the increment of the temperature. At the same time, AFM was used to observe the surface roughness of these films. The roughness increases with the increase of the depositions.

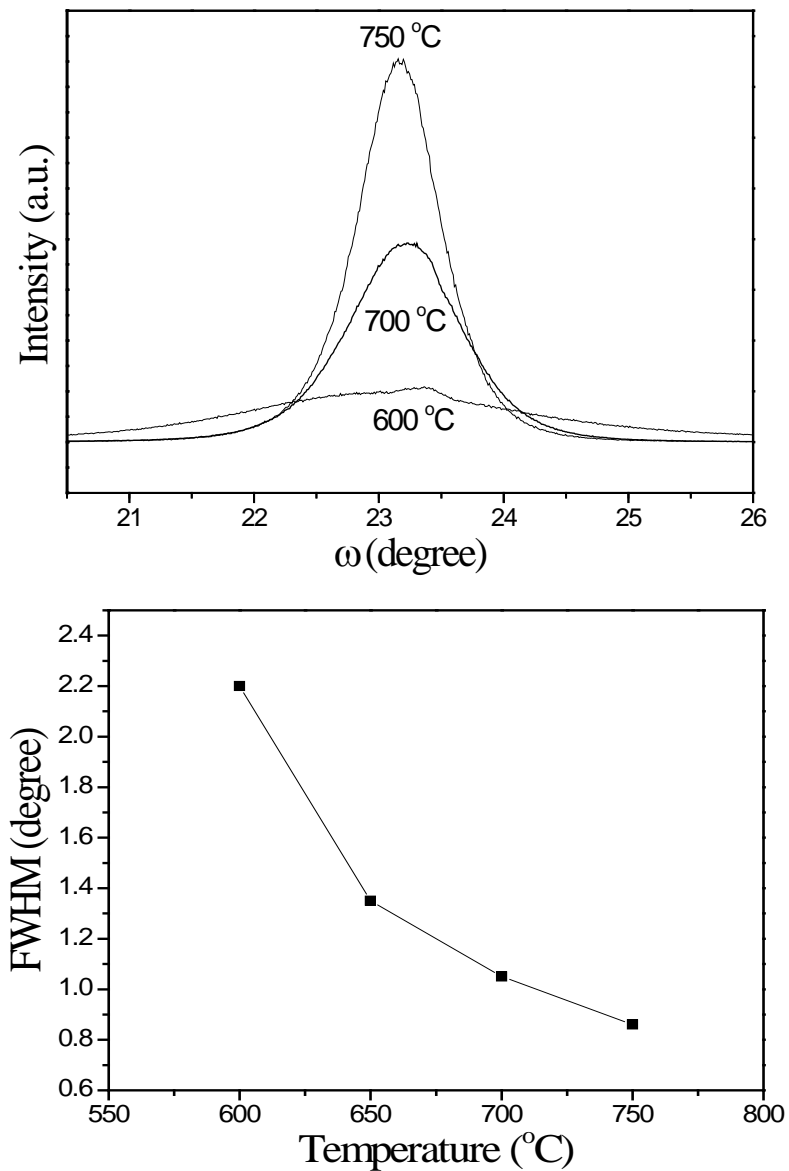


Fig. 2.4 (a) rocking curve of the (002) diffraction peak for SCNN thin films grown on MgO (001) substrate at different temperature; (b) FWHM as a function of substrate temperature

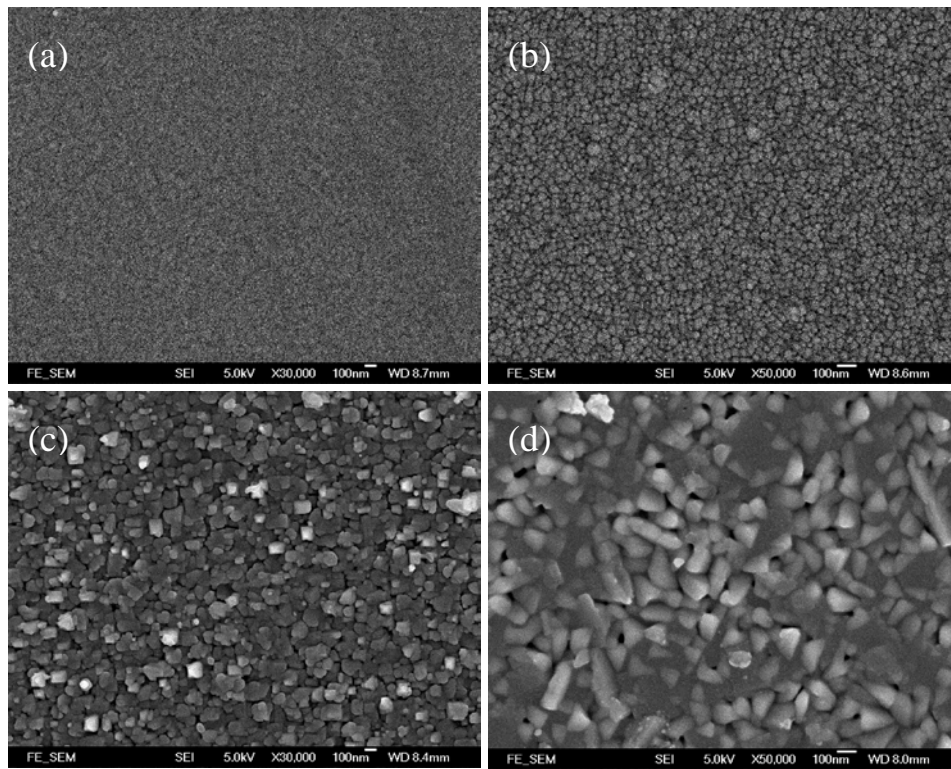


Fig. 2.5 SEM micrographs showing the surface morphologies of SCNN films deposited at: (a) 400 °C; (b) 500 °C; (c) 600 °C and (d) 700 °C.

3 Optical properties of SCNN and SBN films

3.1 Optical properties of epitaxial and polycrystalline SCNN films

3.1.1 Introduction

SCNN exhibits much higher Curie temperatures (279~297 °C) than those of SBN (20~180 °C) due to the introduction of Na⁺ ions in the void site [Xie, 2002]. The higher Curie temperatures allow SCNN become more useful for practical devices. Furthermore, bulk SCNN exhibits extremely high EO coefficients ($\gamma_{33} = 1325 \text{ pm/V}$), a large refractive index and good optical figure of merit. Since R. R. Neurgaonkar fabricated the SCNN single crystal in 1988 for the first time [Neurgaonkar, 1988], much work has been done to investigate their dielectric, piezoelectric and electro-optic (E-O) properties. But most of these studies focus on the research of bulk SCNN, such as single crystal and ceramic. Indeed, growth of SCNN single crystals has been proven to be very difficult. On the other hand, SCNN ceramics are easily fabricated, but they also have drawbacks such as being polycrystalline structure, have a large opacity and contain a high density of defects. Therefore, the development of waveguide applications has been

concentrated on the fabrication of materials in thin film form so as to perform the same function as bulk (with higher speeds and smaller applied voltage), and take advantage of the geometrical flexibility and possible integration with integrated optical devices. The fabrication of SCNN waveguides is very attractive because the optical confinement inherent in the waveguide structure allows a significant improvement in the efficiency of the EO and nonlinear optical applications. To the best of our knowledge, there have been only a few reports on the fabrication of SCNN waveguide thin films. Since we are mainly interested in fundamental research here, we focus on the research of planar waveguide through depositing high refractive index SCNN films on a substrate of lower refractive index. These structures have good waveguide characteristics due to the large refractive indices difference between SCNN (~ 2.20 at 632.8 nm) and substrates ($n_{\text{fuse quartz}} = 1.46$ at 632.8 nm). In this project, we focused on comprehensive study of microstructures, optical waveguide properties (i.e., refractive index, optical propagation loss) and EO properties. Using a prism coupling technique, transverse electric (TE) and transverse magnetic (TM) modes (m-line) were observed. From these modes, the thickness and refractive indices of the air/epitaxial SCNN/MgO and air/polycrystalline SCNN/fuse quartz planar waveguide were determined. The loss mechanism of the planar waveguide was also investigated.

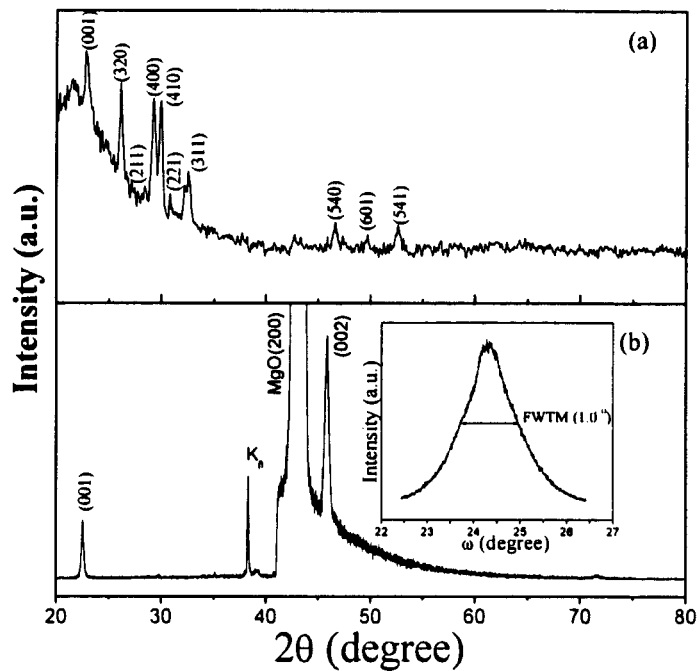
3.1.2 Structural and morphology properties

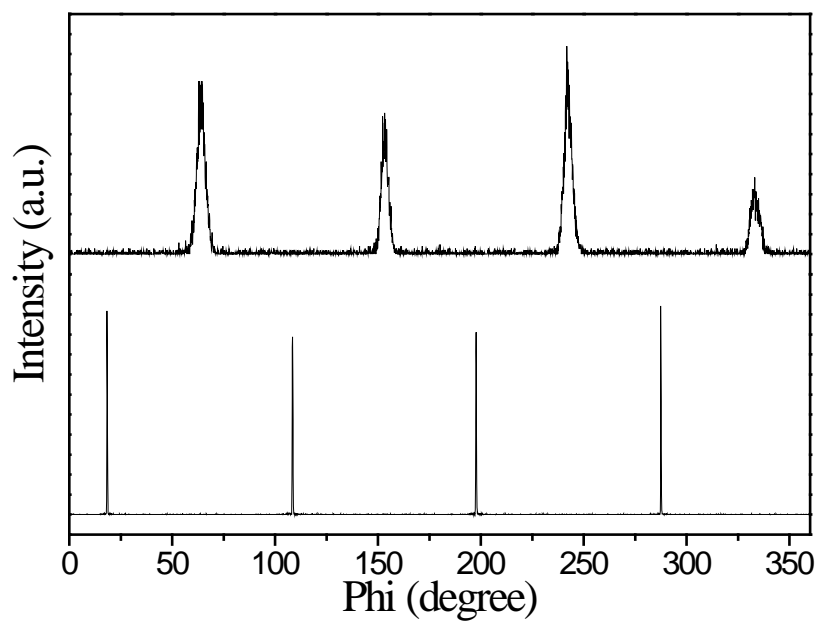
Figures 3.1(a) and 1(b) show the θ - 2θ patterns of the SCNN films on fuse quartz and MgO substrates, respectively. Peaks with weak intensities, indicating a poor crystalline quantity, are observed in the SCNN/fuse quartz films. This is mainly due to the amorphous structure of the fuse quartz substrates. However, strong (001), (320) and (311) SCNN peaks are still clearly recognized. The SCNN film on fuse quartz presents polycrystalline structure and has a pure TTB phase with cell lattice parameters $c = 3.899 \text{ \AA}$ and $a = b = 12.495 \text{ \AA}$. In case of SCNN on MgO substrate, only strong reflections of SCNN (001) and SCNN (002) peaks are identified. No traces of other reflections are founded. Thus, SCNN film is of single phase with c -axis epitaxial growth. The ω -scan rocking curve of SCNN (002) peak was used to gauge the orientation quality of the films. As shown in the inset of Fig.3.1(b), the FWHM is approximately 1.0° . To examine the texture of the in-plane films, the ϕ -scans of the following oblique planes were performed: (111) planes of MgO and (221) plane of SCNN, as shown in Fig.3.1(c). Coincidence of the maxima of ϕ -scans indicates “diagonal-on-side” orientation of SCNN-on-MgO unit cells. As shown in fig.3.1 (d), two times of MgO diagonal perfectly matches the SCNN side ($4.21 \text{ \AA} \times 2 \times \sqrt{2} \approx 12.36 \text{ \AA}$) with a misfit of

3.6%, thus promotes an epitaxial growth of the SCNN film atop the MgO layer.

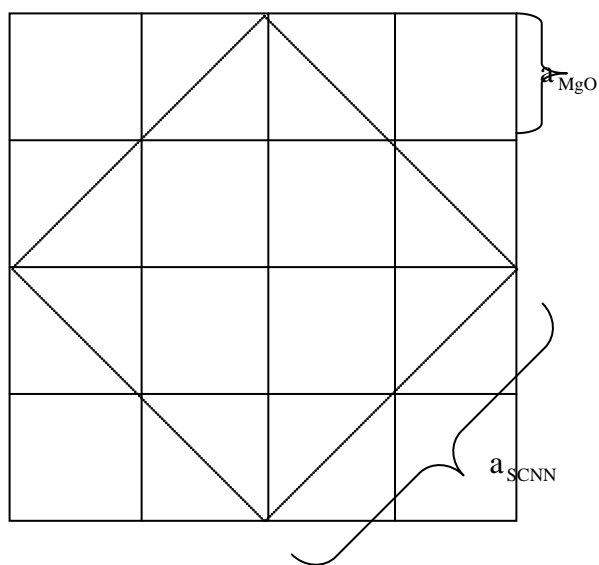
In general, the matching of lattice constants between the substrates and the films as well as the matching of their free surface charge or electrostatic energy will strongly affect the epitaxial growth of thin films. In our case, SCNN has a very complicated structure (as shown in figure 3.2), making it very difficult to be fabricated epitaxially on the surface of many single crystal substrates. Furthermore, SCNN and MgO have lattice constants of 1.236 and 0.421 nm respectively. A more convincing matching for epitaxy would be the alignment between three MgO lattice and one SCNN lattice with no phi-angle rotation. This results in a mismatch of about 2.1%. However, with a phi-angle rotation of 45° as observed in our XRD data, the mismatch is about 3.6%. However, apart from the concern in lattice matching, we also have to consider the electrostatic energy issue. Because of the complicated structure of SCNN, it is almost impossible to have a fully tidy alignment between the atoms in SCNN and MgO. Indeed, SCNN crystal prefers to select an alignment such that the final arrangement should have as many NbO_6 octahedrons (the framework of SCNN cell) as possible to align in the same direction as that of MgO lattice, in order to minimize the electrostatic energy. Figure 3.2(b) shows that through the rotation

of MgO cell by 45° with respect to the SCNN cell, all B1 site octahedrons in the SCNN cell are parallel to the MgO lattice, as compared with the case that with zero rotation (with smaller lattice mismatch) of the MgO lattice, no octahedrons are parallel to the MgO lattice (as shown in figure 3.2(a)).





(c)



(d)

Fig. 3.1 X-ray diffraction patterns of SCNN films on (a) fuse quartz and (b) MgO substrates. Inset is the rocking curve of (200)SCNN peak of SCNN/MgO film. (c) Phi-scan pattern of SCNN films on MgO substrates. (d) is illustration of one unit cell of SBN corresponding to sixteen unit cells of the MgO substrate.

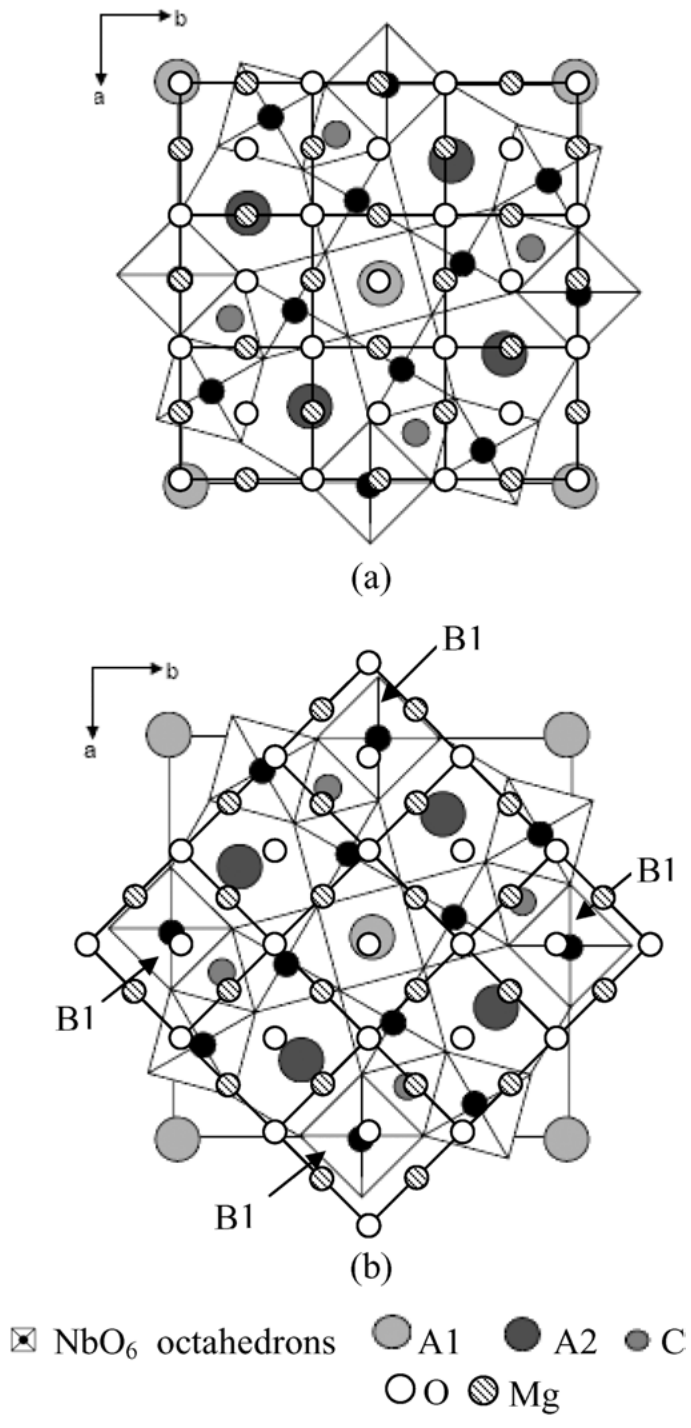


Fig. 3.2 Schematic diagrams show single SCNN unit cell sitting on 3×3 MgO lattice. In (a), the 3×3 MgO lattice has zero rotation with respect to the SCNN unit cell. In (b), a 45° rotation is shown. It is noticed that in (b), the NbO_6 octahedrons (B1 sites) are aligned with the MgO unit cells.

Figures 3.3(a) and (b) show the AFM images ($3 \times 3 \mu\text{m}$) of SCNN films deposited on fused quartz and MgO, respectively. The surfaces are fairly homogeneous and free of any micro-sized particles. The root-mean-square (rms) roughnesses of the SCNN/fused quartz film and SCNN/MgO film are 1.17 nm and 1.72 nm, respectively. The grain sizes of SCNN/fused quartz and SCNN/MgO films are about 80 - 100 nm and 60 - 80 nm, respectively. Our AFM images reveal that the SCNN thin films have smooth and dense surfaces, and the optical loss by surface scattering is expected to be low.

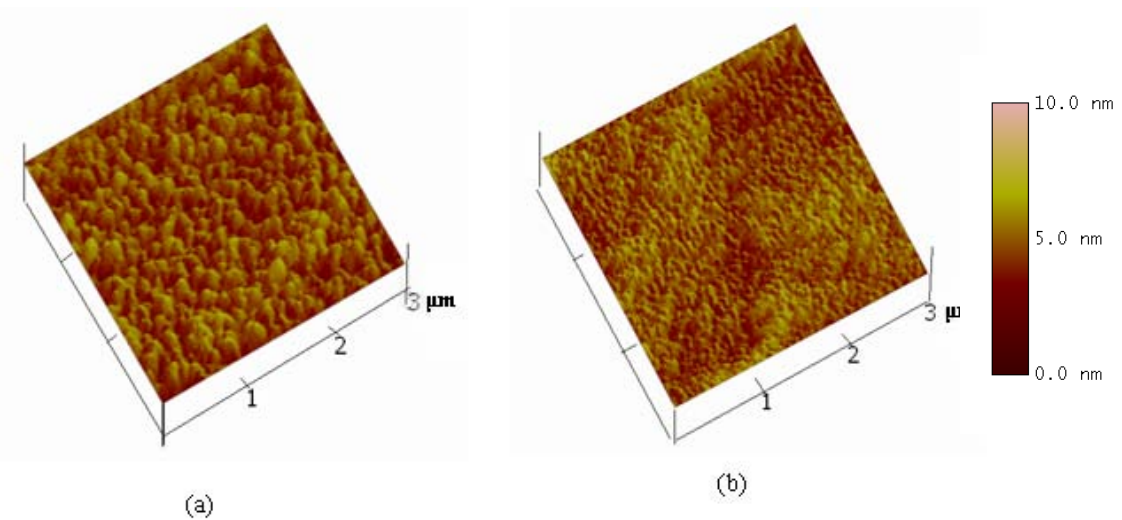


Fig. 3.3 AFM images of SCNN films on (a) fused quartz and (b) MgO substrates.

3.1.3 Optical transmission properties

Optical transmission measurements in the wavelength range of UV-visible-near infrared have been carried out in order to determine the dispersion of the refractive index. Optical transmission $T(\lambda)$ spectra (Fig. 3.4) for SCNN films deposited on transparent MgO and fused quartz substrates were measured using a double beam spectrophotometer. Both the SCNN/MgO and SCNN/fused quartz films exhibit about 80% transmittance from 400 nm to 900 nm. The well structured and smooth oscillations of the transmittance profiles indicate that the films have flat surfaces and uniform thicknesses. The transmittance of SCNN single crystals obtained from reference is also plotted in the figure for comparison [Zhang, 2004]. The inset curves plot $(h\omega\alpha)^2$ as a function of $h\omega$ for SCNN/MgO and SCNN/fused quartz thin films. The absorption coefficient α of the SCNN films near the absorption edge was calculated directly from transmittance T against wavelength using the following formula [Liu, 2005]:

$$\alpha = \frac{1}{d} \ln\left(\frac{1}{T}\right) \quad \text{and} \quad (\alpha h\omega)^2 \propto (h\omega - E_g) \quad (3.1)$$

where d is the thickness of the SCNN film, E_g is the optical band-gap energy

and $h\omega$ is the energy of the incident photon. By using intercept method, optical band-gap energies of the SCNN single crystal and SCNN films grown on MgO and fused quartz are found to be 3.12, 3.97 and 3.98 eV, respectively. A large difference in the band gap energies between the single crystal and our films is obtained. Following Manifacier [Manifacier, 1976], the long wavelength transmittance was employed to calculate the linear refractive index n . The calculated values of the refractive index n are shown in Fig. 3.5. The inset of Fig. 3.5 shows that $1/(n^2 - 1)$ decreases linearly with $1/\lambda^2$. This indicates that the refractive index of the SCNN films follows the Sellmeier dispersion relationship (Here the refractive index $n(\lambda)$ stands for the ordinary refractive index at wavelength of λ) [DiDomenico, 1986]:

$$n(\lambda)^2 - 1 = s_0 \lambda_0^2 / [1 - (\lambda_0/\lambda)^2] \quad (3.2)$$

From the figure, we notice that the refractive indices of the epitaxial SCNN/MgO films are larger than those of the polycrystalline SCNN/fused quartz films at the same wavelength. Takayuki *et. al.* suggested that both the epitaxial and polycrystalline films have a number of void networks. Densely packed crystallites with fewer void networks in epitaxial films usually results in

relatively larger refractive index [Miyazaki, 1992].

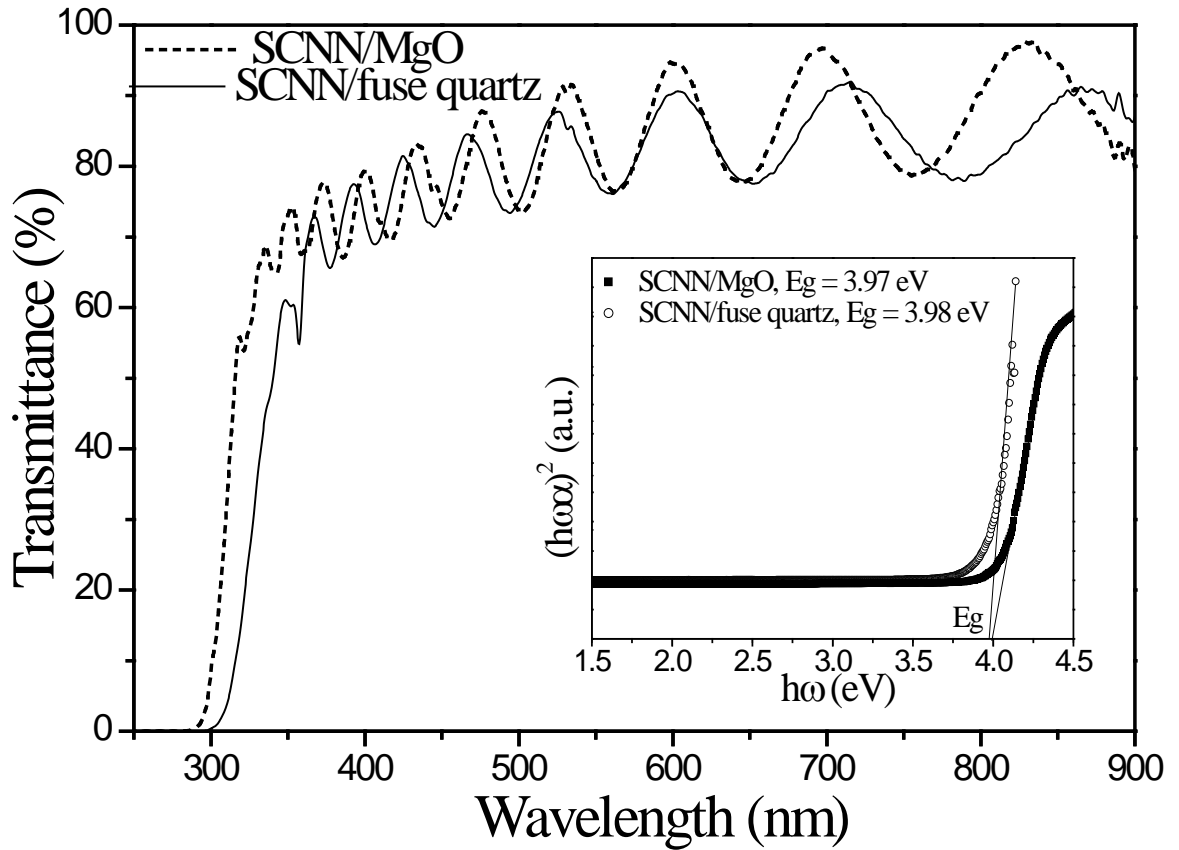


Fig. 3.4 The wavelength dependence of transmittance for SCNN films on fused quartz and MgO substrates and SCNN single crystal. The inset is plots of $(h\omega\alpha)^2$ as a function of $h\omega$ for SCNN/fused quartz and SCNN/MgO films. Extrapolating the line to intersect with the energy axis, E_g was obtained.

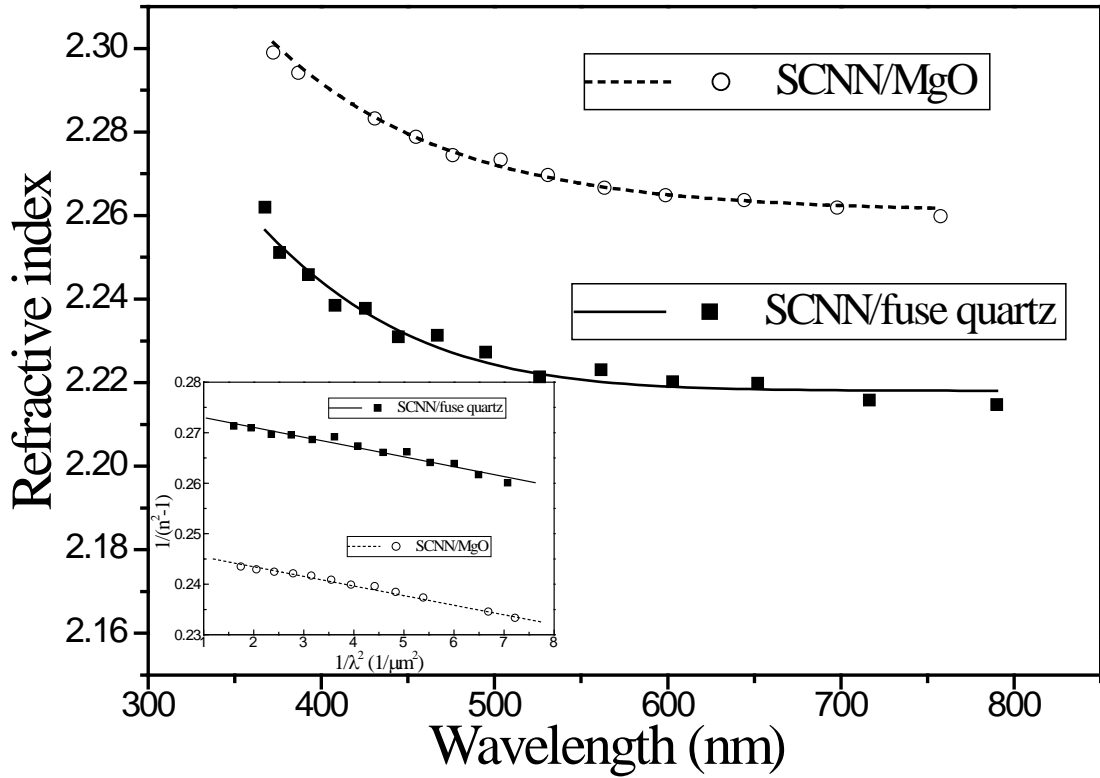


Fig. 3.5 Dispersion of the refractive index of SCNN films on fuse quartz and MgO substrates obtained by optical transmission data. Inset is plots of $1/(n^2 - 1)$ as a function of $1/\lambda^2$.

3.1.4 Waveguide properties

The Model 2010 prism coupler experimental setup describing the m -lines and measuring the propagation loss has been presented in Fig. 1.5. Figures 3.6(a) to (d) show the TE and TM guided modes in the SCNN/MgO and SCNN/fused quartz films. Four TE-polarized, three TM-polarized guided modes and four TE modes, three TM modes are observed in SCNN/MgO and SCNN/fused quartz, respectively. SCNN is a uniaxial crystal of tetragonal structure with c -axis as its optical polar axis. Our SCNN films are c -axis oriented epitaxially grown on (100)MgO substrates. Therefore, the measured n_{TE} and n_{TM} represent the ordinary refractive index n_o and the extraordinary refractive index n_e of the SCNN/MgO films, respectively. At a wavelength of 633 nm, our samples gives $n_o=2.278$ and $n_e=2.183$. Our measured n_o is close to that of SCNN bulk single crystals ($n_{SCNN\ crystal} = 2.280$). The film thickness deduced from the guided mode data is 760 nm. It should be noted that there is a relatively large refractive index difference of 0.095 between n_{TE} and n_{TM} . Due to the tetragonal symmetry and epitaxial growth, the SCNN/MgO films have anisotropic optical properties. The anisotropy results in uniaxial birefringence, i.e. two different refractive indices for polarization parallel and perpendicular to the c -axis [Bergmann, 1999]. For the

SCNN/fused quartz films, n_{TE} and n_{TM} are determined to be 2.251 and 2.237, respectively. The randomly oriented polycrystalline tetragonal films results in a smaller birefringence, that is, a smaller difference between n_{TE} and n_{TM} (0.014), as compared to that of the anisotropic SCNN/MgO films. The thickness of the SCNN/fused quartz film is determined to be 990 nm.

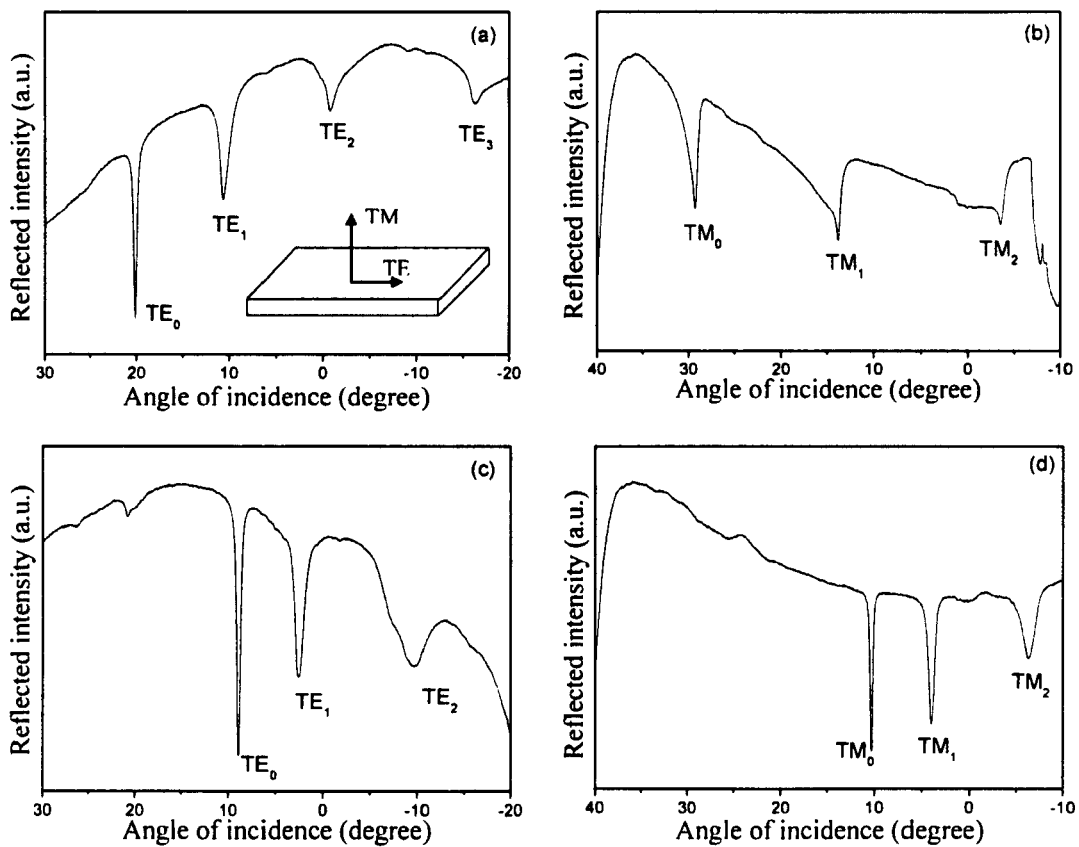


Fig. 3.6 Mode spectra of SCNN/MgO thin films in (a) TE and (b) TM polarizations and SCNN/fused quartz films in (c) TE and (d) TM polarizations.

In order to investigate the film homogeneity and the interface properties, we have reconstructed the refractive index profiles directly from the measured effective indices by using an improved version of the inverse Wentzel-Kramer-Brillouin (*i*WKB) method which only depends on the refractive index distributions within the guiding layer. More details of calculation are given by White [White, 1976]. Using a polynomial interpolation of the measured effective index, we computed the refractive index profiles as a smooth function of the thickness. Figure 3.7 displays the evolution of the TE refractive index as a function of the layer thickness. For both the SCNN/MgO and SCNN/fuse quartz films, the refractive index profiles indicate a step-index variation which is synonymous of a good optical homogeneity along the film thickness. Indeed, the refractive index remains constant within the guiding region and decreases rapidly near the film-substrate interface. Therefore, this step-index variation is rather synonymous of a good optical homogeneity along the film thickness. This result does not show any important interaction between the film and the substrate. The refractive indices turning point of the SCNN/MgO and SCNN/fuse quartz films are observed to be 760 nm and 950 nm, respectively. A good agreement is observed with the data obtained directly by prism coupler.

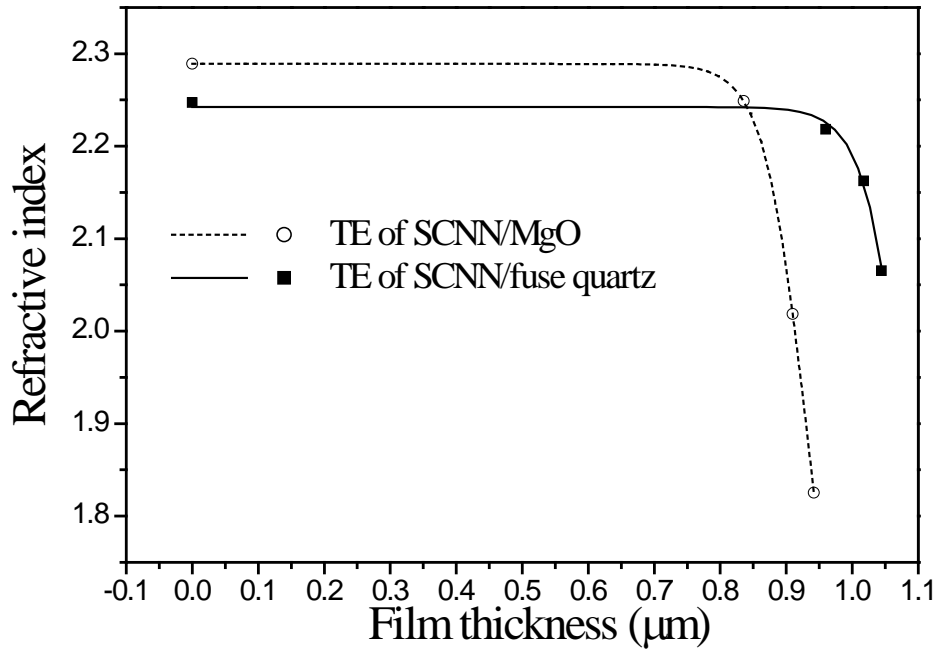


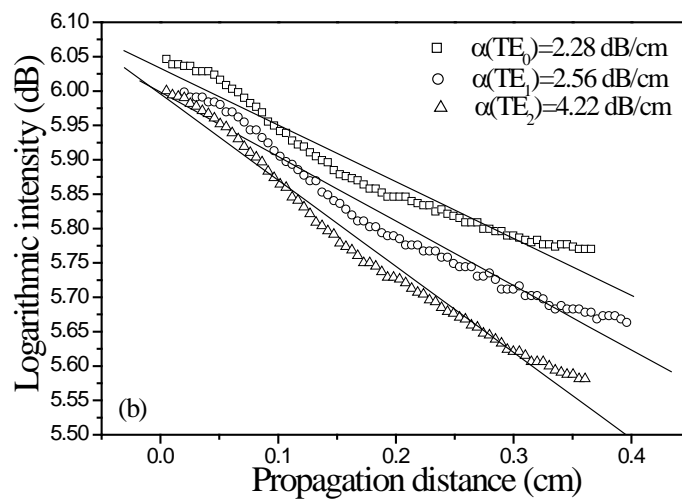
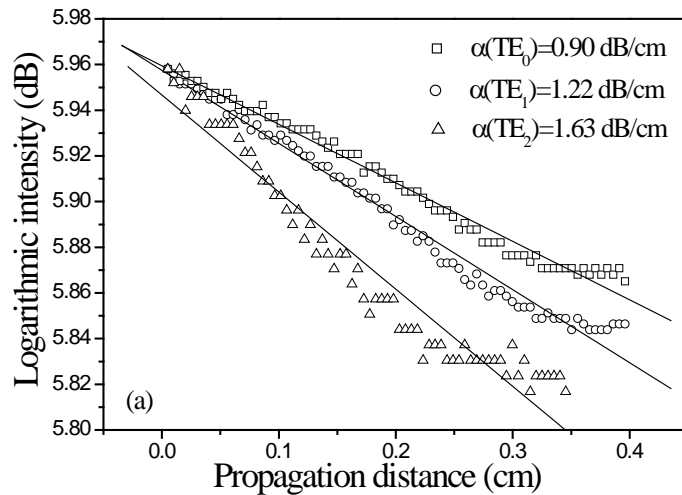
Fig. 3.7 TE refractive index profiles obtained by an inverse WKB method for SCNN films deposited on fuse quartz and MgO.

By varying the incident angle, all guided modes for the films could be separately excited and the out-of-plane scattered light was visible as a streak that extend along the guide away from the prism, as shown in 3.8 (c). The measured scattered intensity from the air/SCNN/MgO and air/SCNN/fuse quartz planar waveguides are observed as a function of propagation along the guide as displayed in Fig. 3.8. TE₀, TE₁, and TE₂ modes were excited in the SCNN films on MgO. A

least-square fit gives the optical loss α of 0.90 dB/cm for the mode TE₀. For modes of higher orders, we determined higher losses with 1.22 dB/cm for the mode TE₁ and 1.63 dB/cm for the mode TE₂. The influence of the different substrates and crystalline quality on the propagation losses was found to be important as observed in Fig. 3.8 (b). We obtained losses of 2.28 dB/cm, 2.56dB/cm and 4.22 dB/cm for the mode TE₀, TE₁ and TE₂ of SCNN films on quartz, respectively. This shows that losses of corresponding modes of the SCNN/fuse quartz waveguide are larger than those of the SCNN/MgO waveguide.

There are several sources of loss, such as absorption, leakage, internal scattering, surface scattering and interface scattering [Mir, 1994]. Among these sources, internal scattering, interface scattering and surface scattering seem to be the major contributors. The surface scattering loss depends on the surface roughness. From our AFM results, the SCNN/fuse quartz films have smoother surface with rms of 1.17 nm, as compared to that of the SCNN/MgO films with rms of 1.72 nm. This means that the SCNN/fuse quartz films should have smaller surface scattering loss than the SCNN/MgO films. But in fact, our results show that the SCNN/MgO films have a much smaller optical loss compared to the SCNN/fuse quartz films. This indicates that the internal scattering and the

interface scattering, rather than the surface scattering, are dominant in our SCNN waveguide structures. Grain boundaries in optically isotropic media may induce refractive index discontinuities among grains that can scatter the guided mode. Refractive index discontinuities at grain boundaries will therefore effectively scatter light along the direction of propagation. Furthermore, any polycrystalline medium that is optically isotropic will scatter light if the crystalline orientation varies among grains. Hence, highly oriented thin films with good crystal quality play an important role in lowering both the interface and internal scattering losses.



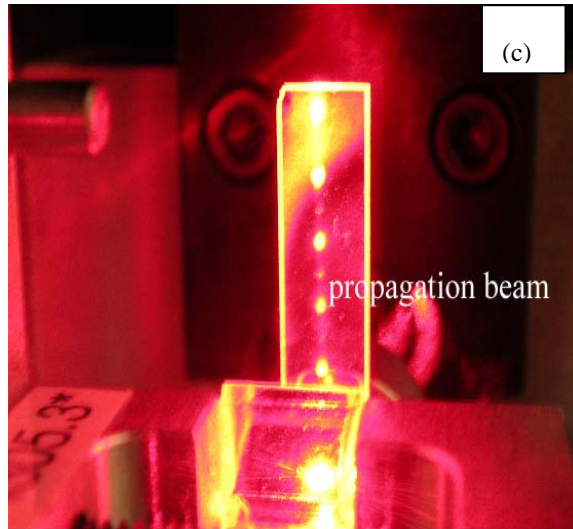


Fig. 3.8 Optical attenuation of different order modes of (a) SCNN waveguide on MgO and (b) SCNN waveguide on fuse quartz. (c) Photograph of a screen image of the propagating 633 nm He-Ne laser beam in SCNN/MgO films.

Figure 3.9 shows the optical propagation loss and the FWHM of TE guided modes coupled to the SCNN waveguide structures on MgO and fused quartz substrates as function of the TE mode order. For both the SCNN/MgO and SCNN/fused quartz samples, the FWHM and the optical loss increase with mode

order. There is a direct proportional relationship between the FWHM and the propagation loss. We notice that the FWHM and optical propagation loss of the TE₀ mode of the SCNN/MgO structure is reduced by around one half and one third in comparison to those of the SCNN/fused quartz waveguide, respectively. Finally, for higher mode order, both the FWHM and propagation loss of the guided modes in the SCNN/MgO waveguide are smaller, indicating that SCNN/MgO waveguides have better performance than the SCNN/fused quartz waveguides.

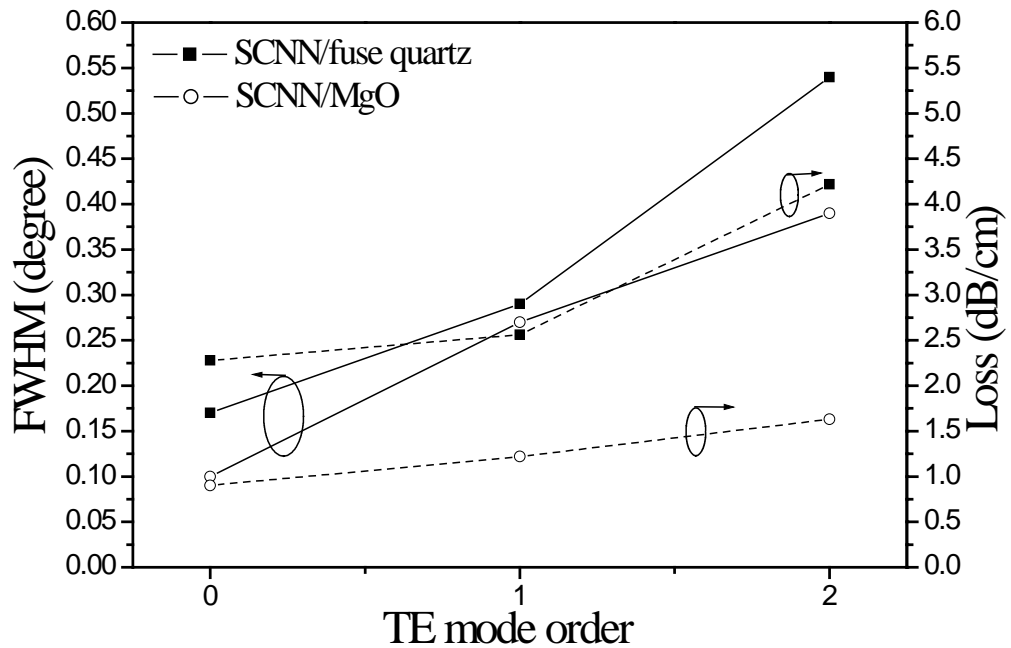


Fig. 3.9 Optical propagation loss and FWHM of different order modes of TE guided modes coupled to the SCNN waveguide structures on MgO and fused quartz substrates.

3.1.5 Conclusion

High transparent epitaxial SCNN films on (100)MgO and polycrystalline SCNN films on fused quartz were successfully deposited by pulsed laser deposition. The surface morphologies of the thin films were observed to be very smooth with RMS of 1.17 nm for the SCNN/fused quartz films and 1.72 nm for the SCNN/MgO films. Refractive indices dispersive curves following Sellmeier dispersion relationship were obtained from the measured transmittance curve using the Manifacier model. The polycrystalline SCNN/fused quartz film shows slightly low refractive indices compared to the epitaxial SCNN/MgO films. We have investigated the optical properties of the planar waveguides using the prism coupler technique. The ordinary (n_o) and the extraordinary (n_e) refractive indices of the SCNN/MgO films are determined to be 2.278 and 2.183, respectively. The relatively large index difference of 0.095 due to uniaxial birefringence is the resulted of anisotropic crystal microstructure. A small difference between n_{TE} and n_{TM} was found in the polycrystalline isotropic SCNN/fused quartz films. An optical propagation loss of 0.90 dB/cm for the TE₀ mode of the SCNN/MgO waveguide was measured. This is much smaller than the 2.28 dB/cm of the SCNN/fused quartz waveguide. This result confirms the interest

of using a well oriented, textured, and crystallized thin film for integrated optics application. A direct proportion relationship between the FWHM of the mode angle profile and the optical loss was observed.

3.2 Optical waveguiding in epitaxial $\text{Sr}_{1.8}\text{Ca}_{0.2}\text{NaNb}_5\text{O}_{15}$ films integrated on Si(001) substrates

3.2.1 Introduction

The optical confinement inherent in the waveguides allows a significant improvement in the efficiency of the EO and nonlinear-optical applications. The basic design of a waveguide device usually incorporates a ferroelectric film with high refractive index as the core layer and a low refractive index layer as the cladding layer. Based on this geometry, high light intensity per unit power in the waveguide can be achieved. Hence, a large nonlinear effect can be obtained in a short interaction length which is necessary for fast- and low-voltage applications. Excellent waveguiding properties have been demonstrated by some research groups in SBN films grown on single crystalline substrates [Lee, (1999); Zhu, (1997)]. But the high cost of single crystal substrates and low compatibility with semiconductor technology limited the practical application of these waveguide devices. If we can combine the good waveguiding properties of TTB materials with the well developed silicon micromachining technology, new devices will be developed by bridging the gap between integrated optics and microelectronics.

Until now, limited studies on this area have been reported. Xiong *et al* fabricated SBN films on Si substrates using SiO₂ or MgO as buffer layer [Xiong, (1998)]. Only polycrystalline SBN films were obtained on Si(0 0 1) substrates. As we know, epitaxial growth is important because it increases the EO effect, reduces the defect in the interface between the films and the substrates and hence decreases the optical propagation loss as shown in previous section. Chiu *et al* fabricated epitaxial SBN films on Si substrates using LaNiO₃(LNO)/CeO₂/YSZ buffer layers [Chiu, (2003)]. Since LNO decomposes easily while La and Ni ions tend to interdiffuse into SBN at high growth temperature of SBN, LNO is not suitable to be used as a cladding layer for the waveguide structure [Jong, (1999)]. Based on the above considerations, we report in this chapter, for the first time, our work on the fabrication of epitaxial SCNN films grown on Si(0 0 1) substrates using MgO and TiN as the buffer layers. Furthermore, the optical waveguiding properties of these heterostructures have also been investigated.

3.2.2 Experimental detail

Epitaxial SCNN films have not been grown directly on Si substrates due to a large lattice mismatch (the lattice constants of a_{Si} and a_{SCNN} are 0.543 and 1.236

nm, respectively). In order to overcome this problem, TiN and MgO were used as buffer layers between SCNN and Si in our studies. TiN has been known to grow epitaxially on Si via domain matching epitaxy [Zheleva, 1994]. TiN has many unique properties such as high electrical conductivity, good chemical stability, and large hardness. It prevents the Si substrate from diffusing to the top MgO and SCNN layers. On the other hand, MgO was selected as the second buffer layer because: (1) it protects the TiN from being oxidized during deposition and post annealing process of the SCNN films at high temperature, (2) epitaxial SCNN is easily grown on MgO due to a small lattice mismatch and (3) MgO is an ideal cladding layer material with a small refractive index (~1.735 at 635.8 nm). This produces a large refractive index difference between MgO and SCNN which results in a strong beam confinement.

In this thesis, SCNN/MgO/TiN heterostructures were successfully grown on Si(001) substrates by pulsed laser deposition (PLD) using an ArF excimer laser. The SCNN target was prepared by conventional solid-state reaction process as described in chapter 2. The MgO and TiN targets were commercial targets with purities of 99.9% and 99.5% (Heifei Kejing Materials Technology Co. LTD, China), respectively. The Si substrates were dipped into a 10% HF solution for 15

min to remove the native oxide layer, followed by ultrasonic cleaning in acetone. The target-to-substrate distance was kept at 40 mm throughout the fabrication. For the fabrication of TiN and MgO films, the pressure of the chamber was pumped down to 5×10^{-5} Torr. The substrate temperature was kept at 660 °C. Laser operated at 10 Hz repetition rate was properly focused to produce an on-target fluence of 5 J/cm². For the fabrication of SCNN films, deposition conditions of 10 Hz laser repetition rate, 5 J/cm² energy density, 160 mTorr ambient oxygen pressure, and 740 °C substrate temperature were employed. All as-grown films were post-annealed at the deposition temperature and pressure for another 15 min and then cooled naturally to room temperature.

3.2.3 Structural characterization

The structural properties of the deposited films were characterized by a four-circle x-ray diffractometer (XRD, Philips, X'pert) with Cu K_{α} radiation. Figure 3.10 shows the XRD θ - 2θ profile of the SCNN/MgO/TiN/Si heterostructure. The lattice constants of TiN and MgO are 0.424 and 0.421 nm, respectively, hence, their (002) peaks overlap with each other. SCNN (001) and (002) peaks are identified with no trace of other reflections, indicating that the

SCNN film is of single phase. The ω -scan rocking curves, shown in the left inset of Fig. 3.10, were used to gauge the orientation quality of the films. The full-width at half-maxima (FWHM) of the rocking curves of TiN/MgO (002) and SCNN (002) are 1.65 and 1.94°, respectively. The FWHM value of SCNN (002) is larger than that of SCNN films grown on single crystal MgO (FWHM=1.10) [Zhang, 2004].

Phi-scans of the SCNN (221), MgO/TiN (111), and Si (111) were performed to confirm the epitaxy of the heterostructure. The results are shown in the right inset of Fig. 3.10. It is noticed that TiN/MgO and Si diffraction peaks are at the same ϕ -angles and the peaks are separated by 90° due to a four-fold symmetry. This indicates that the TiN/MgO films are cube-on-cube grown on Si(001) substrates.

On the other hand, the ϕ -scans clearly revealed that a 45° rotation between the basal planes of MgO and SCNN. This in-plane rotation relationship between SCNN and MgO agrees with that reported in Lin *et. al*'s studies [Lin, 1995], but differs from others where the ϕ -scans of films and substrates have a relationship of 18.43° [Nystrom, 1995; Rouleau, 2003]. On the basis of our XRD results, the epitaxial relationships between the deposited films and the Si substrates were concluded to be out-plane $(001)_{\text{Si}} \parallel (001)_{\text{TiN\&MgO}} \parallel (001)_{\text{SCNN}}$ and in-plane $[110]_{\text{Si}} \parallel [110]_{\text{TiN\&MgO}} \parallel [100]_{\text{SCNN}}$.

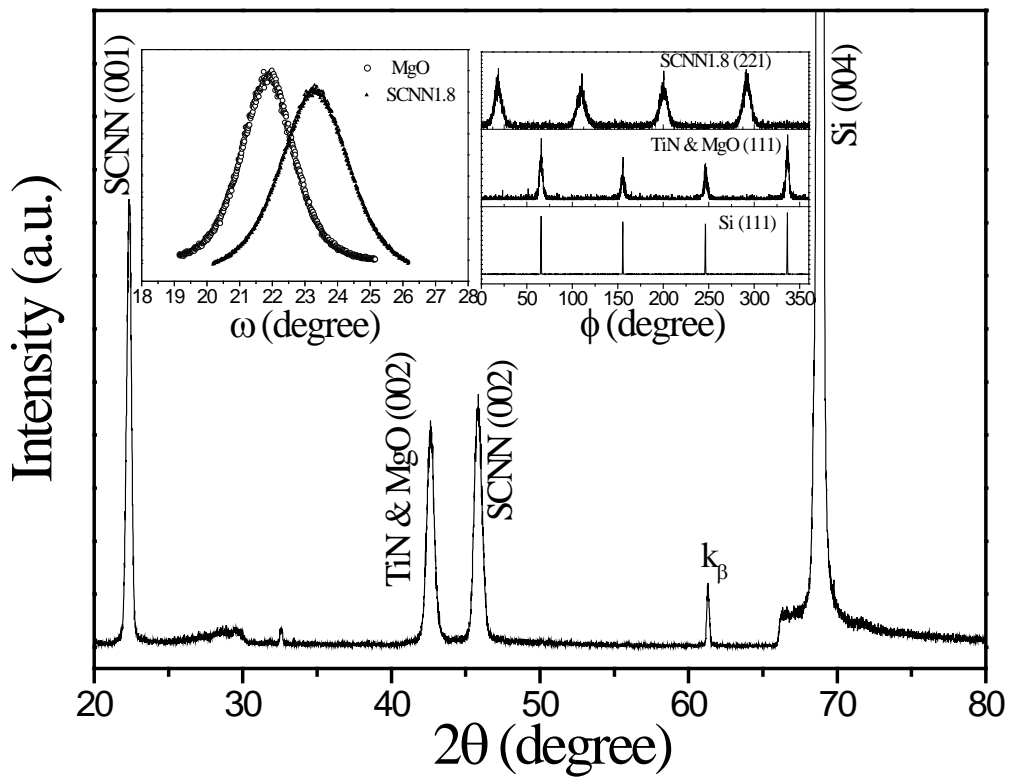


Fig. 3.10 XRD θ - 2θ profile of the SCNN/MgO/TiN/Si heterostructure. Left inset shows the XRD ω -scans of the SCNN(002) and TiN&MgO(002) planes. Right inset shows the ϕ -scans at the Si(111), TiN&MgO(111) and SCNN(221) planes.

SEM was employed to characterize the surface and cross-section morphologies of the heterostructures. Figure 3.11 shows the SEM cross-section

image of the heterostructure, and the inset is its plane view. The top layer of the heterostructure exhibits a smooth, dense and mirror-like microstructure with no observable cracks and large voids. Due to the inherent limitation of the PLD technique, several particulars are observed on the surface. From the cross-section micrograph, three discernable layers with columnar structures are observed. The interface between the SCNN film and MgO buffer layer is smooth and sharp. This smoothness is important in reducing optical loss arisen from interface scattering. The thicknesses of the SCNN, MgO, and TiN layers are estimated to be 650, 200, and 50 nm, respectively. Surface morphologies of the as-grown films were further observed by AFM. Surface with a smooth and grainy structure was observed (figure not shown). The root-mean-square (rms) surface roughness over an area of $5 \times 5 \mu\text{m}^2$ was measured to be 8.9 nm. Surface scattering due to surface roughness is one of the main sources for optical propagation loss in waveguides. We believe that optimization of the growth process can further reduce the surface roughness and decrease the optical loss of our waveguides.

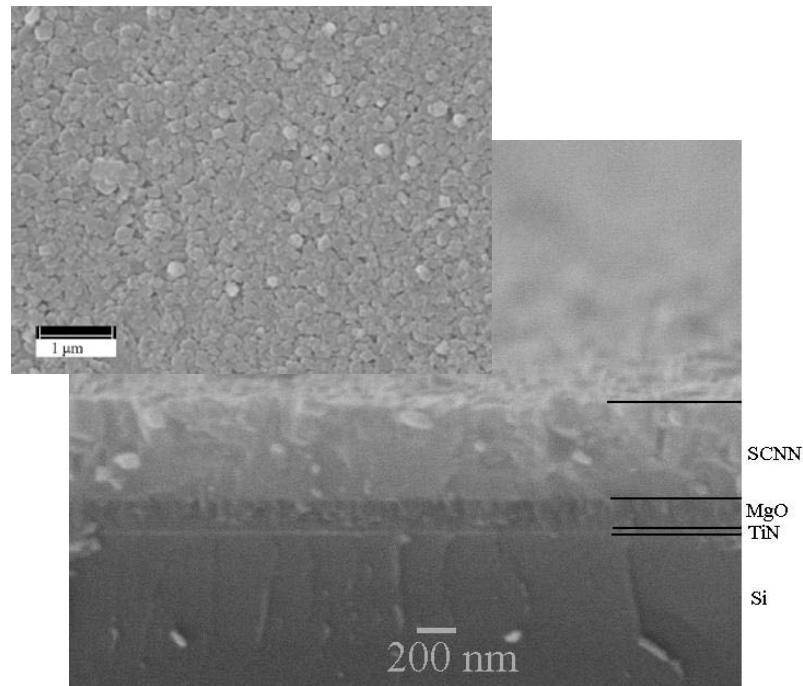


Fig. 3.11 SEM cross-section image of the SCNN/MgO/TiN/Si heterostructure. Inset is the SEM surface morphology image of the SCNN film on MgO/TiN/Si.

3.2.4 Waveguide properties

Optical and waveguiding properties of the SCNN heterostructures were measured using a prism coupler technique. The details of the measurement of the Model 2010 prism coupler was described in chapter 2. Figure 3.12 plots the intensity of the reflected He-Ne laser light (632.8 nm) from the prism as a function of incident angle. In this prism-film coupling method, at specific discrete incident angles called mode angles, photons can tunnel across the air gap to form an optical

propagation waveguide mode, causing a sharp drop in the intensity of light reaching the detector. The existence of propagation modes is clearly demonstrated in Fig. 3.12, where two TM and two TE modes are observed. Figures 3.13(a) and (b) show the direct images of excited TM and TE modes that were coupled into the SCNN films. All excited lines are sharp and distinguishable, indicating that a good confinement of light propagation is achieved. Our measurements clearly demonstrate that the SCNN/MgO/TiN/Si heterostructures are potential candidates for optical waveguide applications.

SCNN is a uniaxial crystal with c -axis as its optical polar axis. All the SCNN films were all c -axis epitaxially grown on Si(001) substrates. The measured n_{TE} and n_{TM} thus represent the ordinary refractive index n_o and the extraordinary refractive index n_e of the SCNN films, respectively. Following Ulrich and Torge [Ulrich, 1973], the refractive index and thickness of waveguide films can be calculated, the details have been shown in chapter 2. Based on the measured TE and TM modes, the n_o and the n_e of our SCNN films are determined to be 2.2141 and 2.1727, respectively. These obtained refractive indices are slightly smaller than those of epitaxial SCNN films grown on single crystal MgO substrates, but larger than those of SCNN films grown on fused quartz. This may mainly due to the slightly deteriorated crystalline quality as well as a lower density

of the SCNN films as compared to that grown on MgO single crystal. It should be noted that there is a relatively large index difference of $\Delta n = n_o - n_e = 0.0414$. We suggest that the large birefringence in SCNN films grown on MgO/TiN buffered Si substrates is due to the pronounced preferential orientation of epitaxial SCNN/MgO films as observed in our XRD analysis. Other orientations in the films will definitely reduce the Δn value. The film thickness of the SCNN films measured by this prism coupler technique was 660 nm, which is in good agreement with that obtained by SEM.

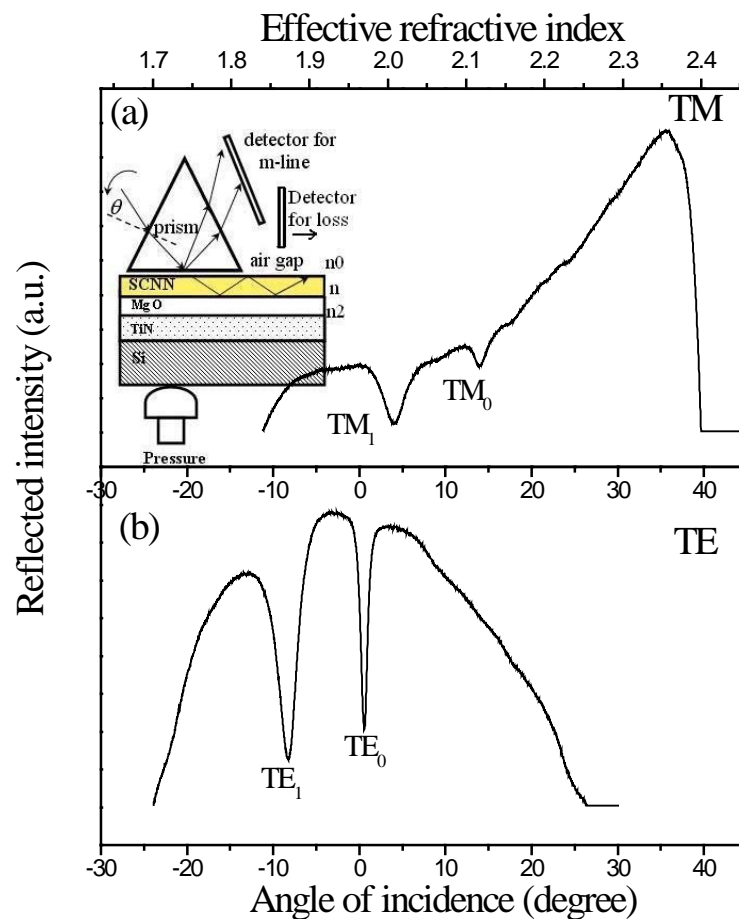


Fig. 3.12 Excited (a) TM-line and (b) TE-line (lower plot) spectra for the air/SCNN/MgO waveguiding structure on a TiN buffered Si substrate.

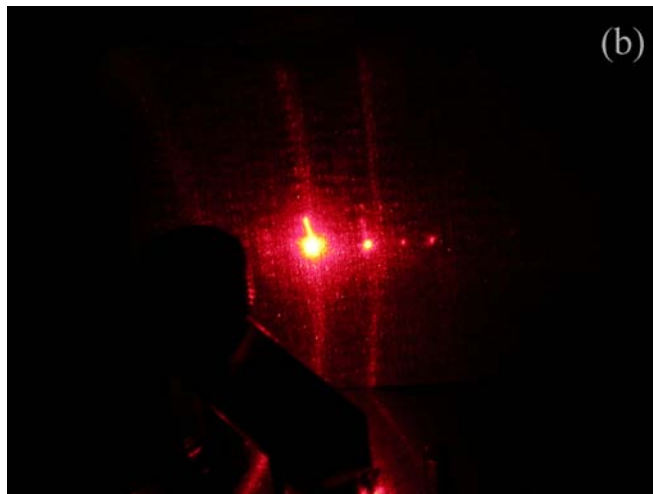
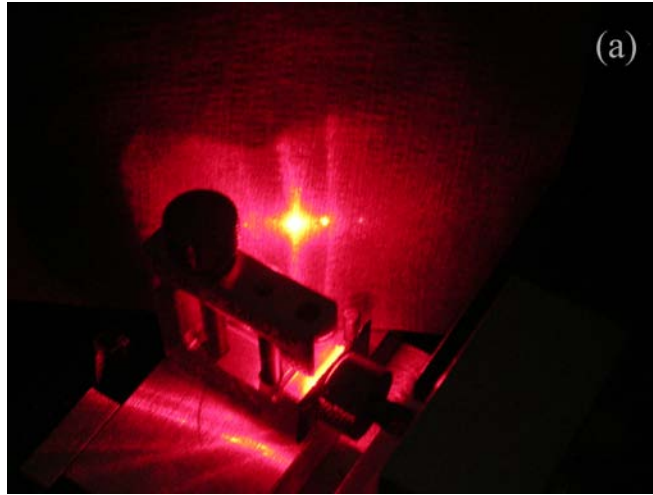


Fig. 3.13 The digital camera captured photographs of excited (a) TM mode-lines and (b) TE mode-lines at 632.8 nm coupled into the SCNN film deposited on MgO/TiN/Si.

Optical loss, critically affecting performance of the film device, is a key parameter for film waveguide. Optical propagation loss in the film can be evaluated as described in chapter 2. The measured data of the SCNN film corresponding to the scattered light intensity as a function of propagation distance for the TE₀ mode are shown in Fig. 3.14. Consequently, the propagation loss δ is calculated to be about 1.7 dB/cm. As introduced in ref. 22, in the measurement of optical loss using prism coupler, the losses can be separated from the surface scattering and from volume attenuation, and volume attenuation has a much stronger influence on low orders of modes than does surface scattering. Surface scattering loss and volume attenuation are determined by film roughness and film quality (orientation and defect), respectively [Zhang, 2002]. Although our SCNN film shows a relative large rms of 8.9nm and should be further improved, an acceptable optical loss value is still obtained due to the excellent epitaxial orientation of the integrated films.

3.2.5 Waveguide properties of epitaxial

SCNN/In:Mg_xZn_{1-x}O/TiN/Si heterostructure

3.2.5.1 Introduction

As introduced in the above section, MgO, combining the advantages of (a) low refractive index; (b) high transparency; (c) matched lattice constant, is an excellent buffer layer material for the integrated waveguide optics. The largest electro-optic coefficient in TTB is the diagonal coefficient, r_{33} , and the measurement of this coefficient in thin films deposited on MgO requires (a) application of an electric field normal to the ferroelectric film surface along the crystal c axis and (b) finite optical polarization component along the c axis [Trivedi, 1996]. So, in some EO waveguide modulators, top transparent and bottom electrodes, but not two parallel electrodes, are needed in order to provide a transverse electric field. The MgO substrate is, however, insulating, thereby making it impossible to have contacts on either side of the film. Though the TiN layer in this heterojunction is a very conductive layer and can be used as the bottom electrode layer, unfortunately, the dielectric constant of MgO is much smaller than that of SCNN (or other ferroelectric materials also), so that most of the electric field is applied on the MgO layer and only very limited part of the

electric field is added on the EO ferroelectric layer. So, beside the above requirements, as an ideal buffer layer, it should be conductive.

Here, indium doped cubic magnesium zinc oxide (In:c-MZO) was introduced to be another choice of buffer layer acting as the role of not just only waveguide buffer layer but also for the bottom electrode layer. Intrinsic ZnO has n-type conduction, which originates from oxygen vacancies in the crystalline structure. By appropriate impurity ions doping, the electrical conductivity of ZnO can be increased dramatically [Iwata, 2004]. This improvement of conductivity can thus lead to a good transparent conducting oxide (TCO). However, ZnO has a stable wurtzite structure at equilibrium condition, which is structurally not compatible to many oxides, such as perovskites and transition metal monoxides. In recently years, cubic $\text{Mg}_x\text{Zn}_{1-x}\text{O}$ was successfully fabricated when magnesium is introduced in ZnO up of 66 at % [Ohtomo, 1998; Sharma, 1999]. Thus, impurity ions doped cubic MZO such as In:c-MZO, combining the advantages of MgO of low refractive index, high transparency and structurally compatibility and adding another advantage of good conductivity, is supposed to be the potential candidate for integrated waveguide optics.

3.2.5.2 Experiment detail

The indium doped c-MZO target was fabricated via a conventional solid state reaction. The original constituents of MgO (99.99%), ZnO (99+%) and In₂O₃ (99.999%) powders immersed in ethanol were firstly mixed by ball milling for at least 6 hours. Then they were calcined twice at 1100°C for 10 hours in air. The final treated powder was pressed into a 2.5 cm circular disc of 0.5 cm thickness by a 4 tones pressure at room temperature. Finally, it was sintered at 1350 °C for 10 hours in air. TiN, and In:c-MZO and SCNN layers were deposited on the HF cleaned Si(100) substrate by PLD in consequent. The deposition conditions for TiN and In:c-MZO and SCNN are similar to that introduced in section 3.2.2.

3.2.5.3 Structure and waveguide properties

Figure 3.15 shows the XRD θ -2 θ profile of the SCNN/In:c-MZO/TiN/Si heterostructure. Only 3 peaks at 22.7°, 41.8° and 45.9° were observed. The peaks at 22.7 and 45.9 are from SCNN (001) and (002), respectively. The 41.8° peak arises from In:c-MZO and TiN (002). Since the lattice of In:c-MZO is slightly smaller

than that of pure MgO and TiN, resulting that these two peaks do not well overlap each other. However, due to the very small difference of these two lattice constants, these two peaks could not be well separated in our measurement. Thus, the peak at 41.8 seems broader than that of MgO&TiN, as shown in Fig. 3.10. As shown in Fig. 3.16, FWHM of the rocking curves of TiN&In:c-MZO (002) and SCNN (002) are 2.9 and 2.2 °, respectively. The FWHM value of SCNN (002) is slightly larger than that of SCNN films grown on TiN &MgO buffered Si. Phi-scans of the SCNN (221), In:c-MZO&TiN (111), and Si (111) were performed to confirm the epitaxy of the heterostructure. The results are shown in Fig. 3.17. The epitaxial relationships between the deposited films and the Si substrates were concluded to be out-plane $(001)_{\text{Si}} \parallel (001)_{\text{TiN\&In:c-MZO}} \parallel (001)_{\text{SCNN}}$ and in-plane $[110]_{\text{Si}} \parallel [110]_{\text{TiN\&In:c-MZO}} \parallel [100]_{\text{SCNN}}$, same with that of SCNN/MgO/TiN/Si heterostructure. Besides the structural match, the conductivity and refractive index of the In:c-MZO have to be considered. The resistivity of the films is highly depended on the doping concentration of indium. For undoped c-MZO films, the resistivity is as high as $3 \times 10^7 \Omega\text{cm}$ which are nearly insulating. The resistance drops when indium is incorporated in the film. At about 18 at. % indium doping, the resistivity goes down to $5.5 \times 10^{-2} \Omega\text{cm}$. In order to get the best conductivity for being the bottom electrode, here we have chosen the 18 at. % indium doping

c-MZO as the buffer material. Fig. 3.18 shows the observed TM and TE modes of In:c-MZO films deposited on fused quartz substrates measured by the prism coupler technique. The refractive index of the In:c-MZO is deduced to be 1.86. This is slightly larger than that of pure MgO of 1.74 due to the introduction of Zinc oxide.

Figures 3.19 (a) and (c) show the TE and TM modes of this waveguide structure. Figures 3.19(b) and (d) show the direct images captured by digital camera of excited TM and TE modes that were coupled into the SCNN films. All of the excited mode-lines are sharp and distinguishable, indicating that a good confinement of light propagation is achieved. These measurements suggest that the SCNN/In:c-MZO/TiN/Si heterostructures are potential candidate for optical waveguide applications. Based on the measured TE and TM modes, the n_o and the n_e of our SCNN films are determined to be 2.1164 and 2.0827, respectively, the thickness is 440 nm. Both of the refractive indices and birefringence are slightly smaller than those of epitaxial SCNN films grown on single crystal MgO&TiN buffered Si(100) substrates. This is mainly due to the slightly deteriorated crystalline quality and orientation order of the SCNN films as compared to that grown on MgO&TiN/Si substrate. This is consistent with the

rocking curve result compare of these two heterostructure. Other orientations in the films will definitely reduce the Δn value.

The final target of this heterostructure is the application in integrated EO modulation. EO coefficient is an important parameter. Unfortunately, due to the large leakage between two large area electrodes in the EO measurement process, up to now, the EO properties have not been measured. The quality of the films should be improved through optimization of the fabrication process.

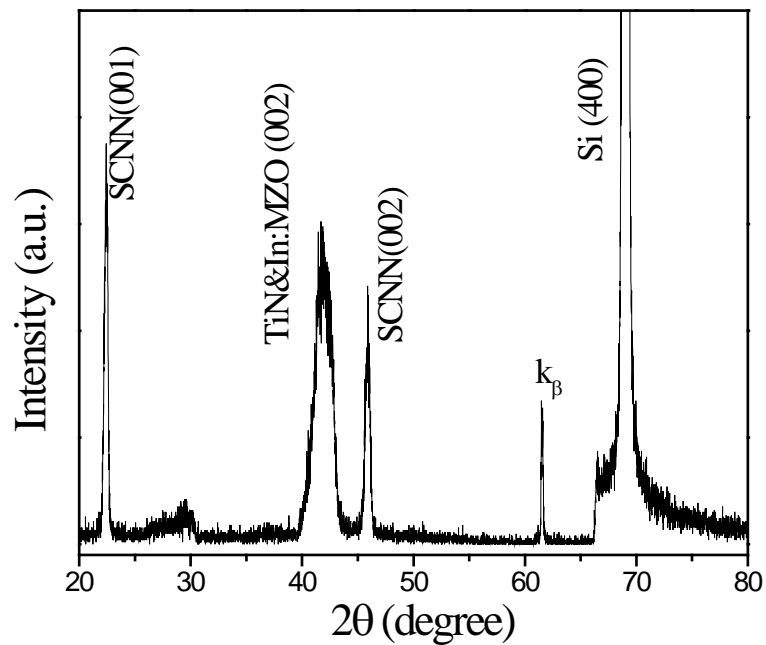


Fig. 3.15 XRD θ - 2θ profile of the SCNN/In:c-MZO/TiN/Si heterostructure.

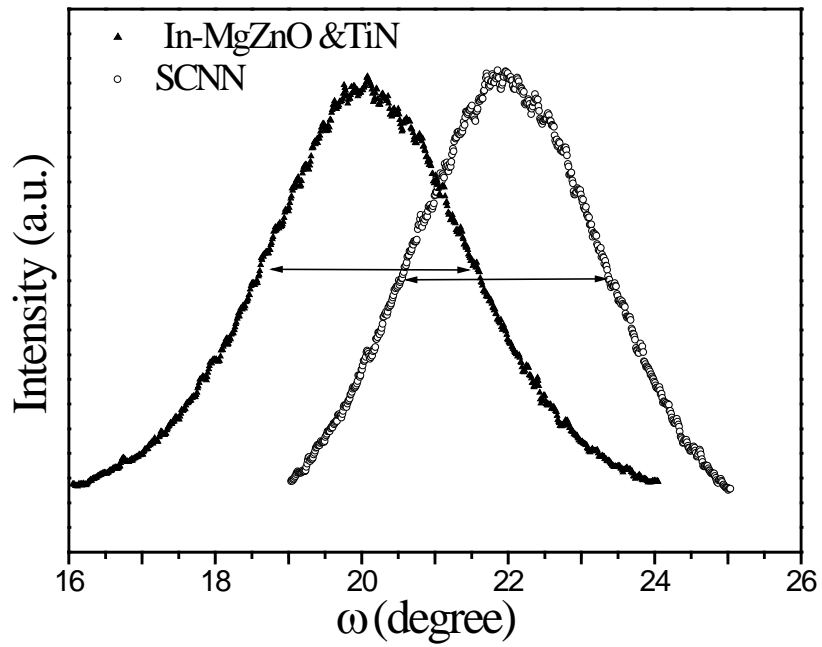


Fig. 3.16 XRD ω -scans of the SCNN(002) and TiN&In:c-MZO(002) planes.

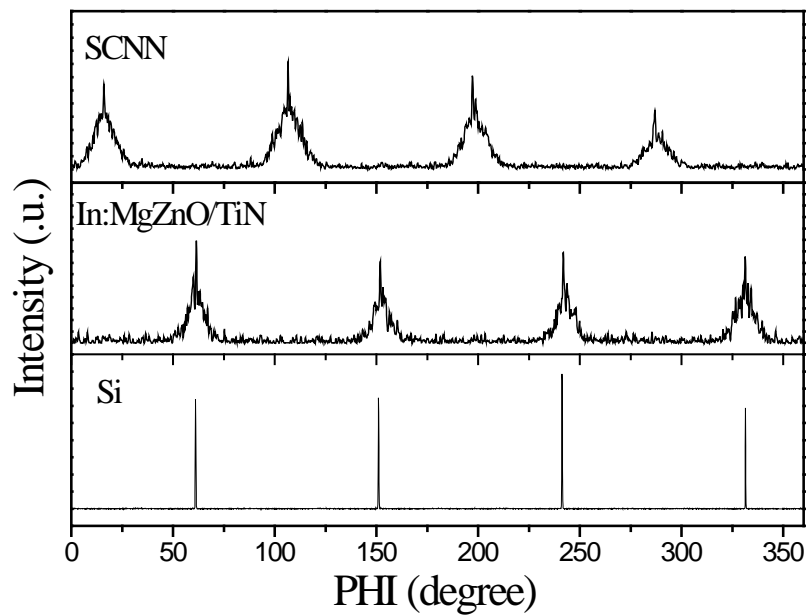


Fig. 3.17 ϕ -scans of the Si(111), TiN&In:c-MZO(111) and SCNN(221) planes.

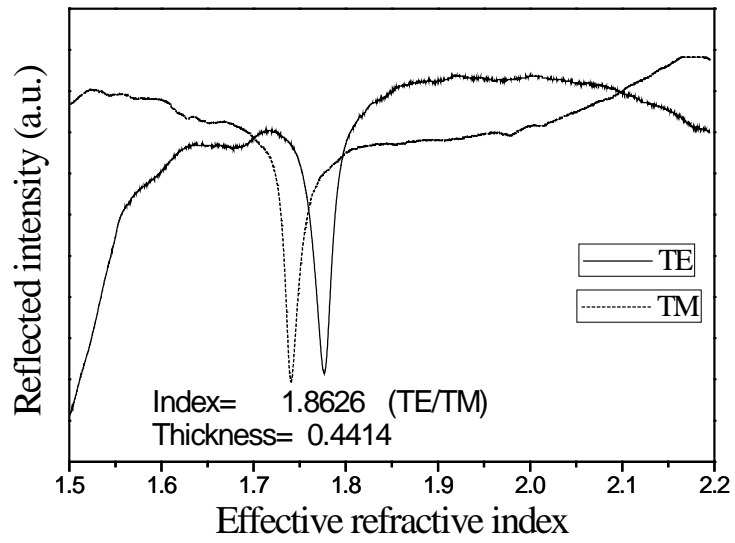
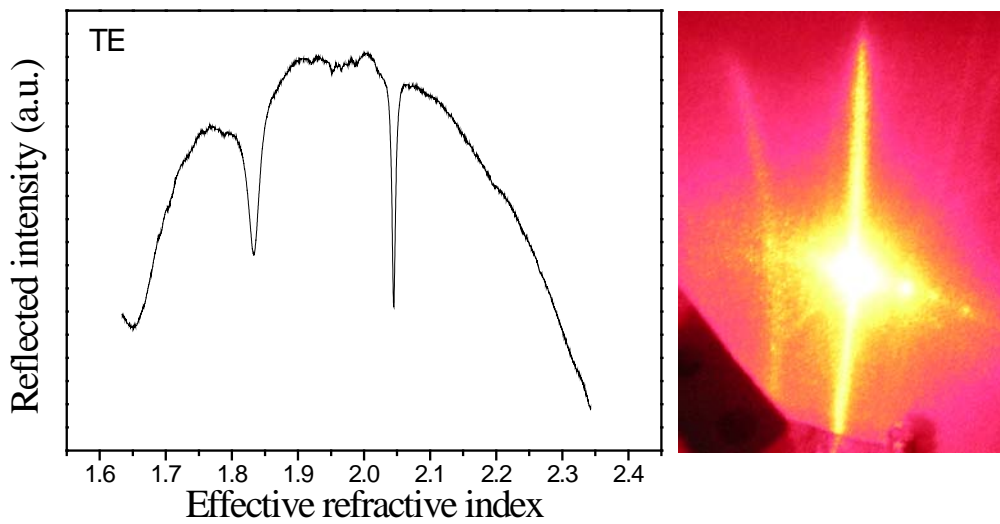
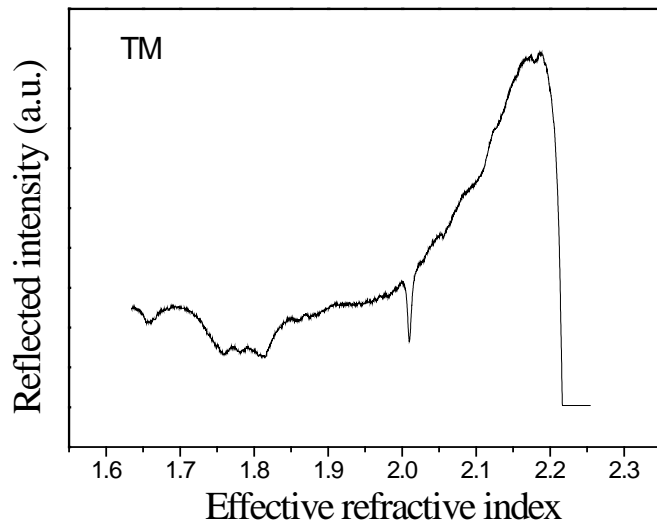


Fig. 3.18 TE and TM modes of In:c-MZO films on fused quartz substrates.



(a)

(b)



(c)



(d)

Fig. 3.19 Excited (a) TE-line and (c) TM-line spectra for the air/SCNN/In:c-MZO waveguiding structure on a TiN buffered Si substrate. The digital camera captured photographs of excited (b) TE mode-lines and (d) TM mode-lines at 632.8 nm coupled into the SCNN film deposited on In:c-MZO/TiN/Si.

3.2.6 Conclusion

In conclusion, epitaxial integrated SCNN/MgO/TiN/Si heterostructures were fabricated successfully by PLD. Three discernable layers with columnar grain structures were observed through SEM characterization. Surface roughness of approximately 8.9 nm was observed using AFM characterization. Optical and waveguiding properties of this heterostructure were measured using the prism coupler technique. Two clear and sharp excited TE mode-lines and TM mode-lines were observed. The ordinary and extraordinary refractive indices were calculated to be $n_o = 2.2141$ and $n_e = 2.1727$, respectively, implying a birefringence of $\Delta n = n_o - n_e = 0.0414$. Propagation loss of 1.7 dB/cm was measured in our waveguides. On the basis of our results, we show that SCNN films are promising waveguiding materials for practical integrated optical devices.

Indium doped cubic magnesium zinc oxide, as another choice for the waveguide buffer layer, exhibits a special advantage compared to pure MgO. It is a very conductive material and can be used as bottom electrode in EO modulator application. Two clear and sharp excited TE mode-lines and TM mode-lines were observed, suggesting the SCNN/In:c-MZO/TiN/Si is a suitable waveguide potential for integrated optics.

3.3 Thermo-optic properties of SBN films

3.3.1 Introduction

Tetragonal tungsten bronze niobates such as SBN and SCNN have been widely studied with regard to both scientific studies of its EO and nonlinear properties and possible application in the field of EO materials such as holographic storage, phase-conjugated mirrors and self-focusing lens [Zhang, 1991; Micheron, 1972; Quiao, 1993]. When a laser beam is passing through a SBN crystal medium, a great change in the refractive index could be created. Obviously, EO effect plays an important role in the change of refractive index [Scott, 1990]. The laser beam creates photo-carriers (electrons excited from traps to conduction band) which induce a local electric field and change the spontaneous polarization of the crystal, thus, induce a change of refractive index. Much work about the EO properties of these materials has been reported. We believe that there is another factor which can affect the refractive index, namely, the thermal effect. The temperature of the crystal increases when a laser with high energy is passing through it. This probably will change the polarization in the crystals. Ramirez *et.al.* reported that the coherent light generation from a Nd:SBN crystal at the temperature through its ferroelectric phase transition [Ramírez, 2005] . They

suggested that both phonons and heat have effect on the second nonlinear properties [Jacinto, 2006]. But how does the heat affect the refractive index of the single crystal independently? It still needs to be investigated. Temperature dependence of the optical properties of the EO thin films or single crystals is an important consideration as it alters the device performance when temperature varies but may also be used in thermo-optical device applications. The thermo-optical effect is a variation of refractive index caused by temperature change. To fabricate active waveguide using the thermo-optical effect, the anisotropies of the films in the variation of refractive index with temperature has to be examined because the films have a strong ferroelectric behavior for which electronic polarization in the films dominates.

In this section, we introduce some basic research work about the temperature dependence of refractive index and thermo-optical properties of SBN thin film, especially in the range near its Curie temperature of 90 °C.

3.3.2 Film fabrication

SBN60 targets were prepared by conventional mixed-oxide process using analysis grade SrCO_3 , BaCO_3 and Nb_2O_5 powders as the starting materials. The process is similar to that used for the fabrication of SCNN. These powders were weighted according to the molecular formula $\text{Sr}_{0.6}\text{Ba}_{0.4}\text{Nb}_2\text{O}_6$ and subsequently ball-milled for 12 h. After being calcined at $1200\text{ }^\circ\text{C}$ for 6 h, the mixed powder was pressed into disk pellets and sintered at $850\text{ }^\circ\text{C}$ for 2 h and then at $1250\text{ }^\circ\text{C}$ for another 10 h. The laser used for the PLD process was a KrF excimer laser (Lambda Physik COMPex205, 248 nm, 20 ns), with a repetition rate of 10 Hz. The distance between the substrate and the target was fixed at 4.5 cm. The on-target laser energy density is about 5 Jcm^{-2} . $\text{MgO}(100)$ substrates were placed on the substrate holder. The SBN films were deposited at a substrate temperature of $740\text{ }^\circ\text{C}$ and under an oxygen pressure of 100 mTorr. Immediately after the deposition, the films were in-situ post-annealed at the growth temperature and 10 Torr oxygen ambient for 10 minutes before they were naturally cooled to room temperature to minimize oxygen deficiency.

3.3.3 Thermo-optical properties of SBN/fused quartz films

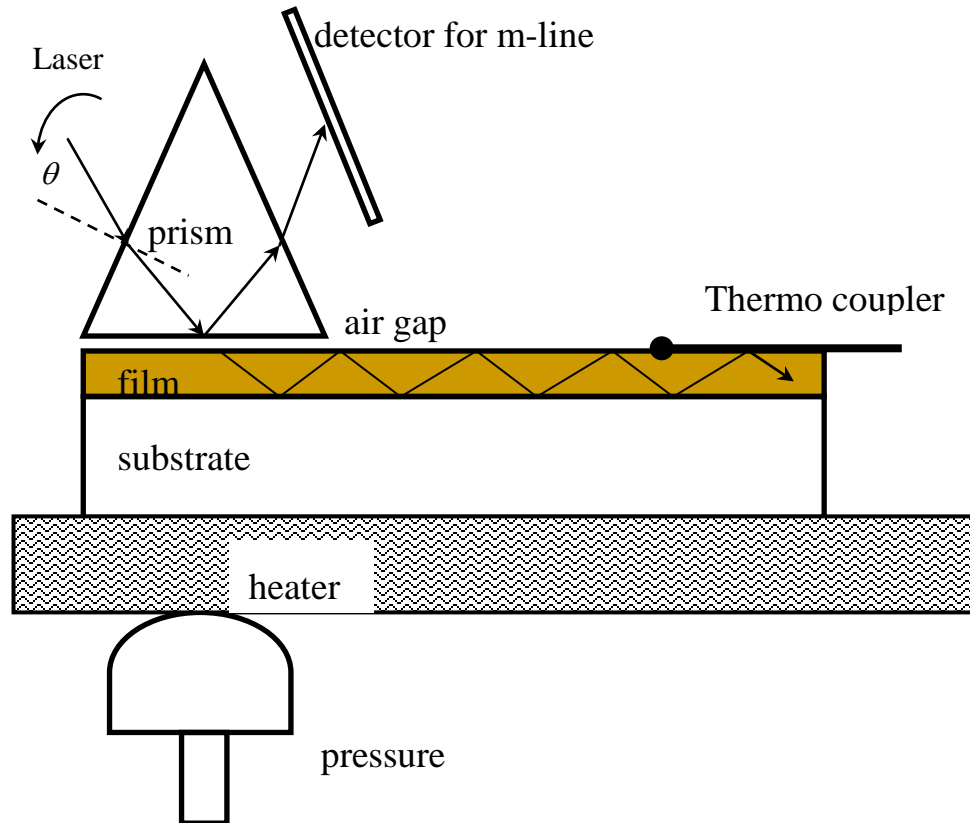


Fig. 3.20 Apparatus for measuring the thermo-optical coefficient of thin films using a prism coupler technique.

A direct and accurate method using prism coupler technique was introduced to determine the refractive indices and thermo-optic coefficients of the waveguide films. Figure 3.20 shows the setup for the thermo-optical

measurement using the temperature controlled prism coupler technique. The films were put on a temperature controlled heater. The temperature control apparatus was driven by ac power. The temperature was controlled by an adjustable voltage. Conductive silver paste was used as an adhesive between the heater and the sample substrate to achieve good thermal contact. Sample temperature was monitored by a thermocouple glued on the film surface with a small amount of silver paste. A laser beam (632.8 nm) with TE or TM polarization was used for the measurements. By heating up the SBN thin films from room temperature to 150 °C, the mode spectra of the TM and TE modes were recorded between 20 °C to 150 °C with interval of 10 °C. Figure 3.21 shows the changes of refractive index as well as the birefringence as a function of temperature. For both TM and TE polarizations, below the Curie temperature, the refractive indices increase slowly with the temperature. In the range of Curie temperature, they increase rapidly. Above the Curie temperature, they increase slowly again. Through differentiating the curves, thermo-optical coefficients (dn/dT) at different temperatures for TM and TE modes were obtained and are plotted in Fig. 3.22. For temperature near T_c , a strong enhancement in the thermo-optic coefficient is observed. This enhancement is probably related to the critical change of the polarization near T_c . The values of dn_{TM}/dT are

significantly larger than that of dn_{TE}/dT due to the larger quadratic electro-optic coefficient in TM direction.

In order to understand these results in more details, we correlate the changes in refractive index at different temperature $n(T)$ with the quadratic EO effect. This effect occurs in all crystals and relates a change in the refractive index to the square of a polarization P [Burns, 1983].

$$\Delta(n^{-2})_{mn} = \sum g_{mnop} P_0 P_p \quad (3.3)$$

where g is the quadratic electro-optic coefficient. Relationship between polarization and refractive index can be described in the following equation:

$$\Delta n_i = n_i^f - n_i^0 = -(n_i^0)^3 g_{i3} P_3^2 / 2 \quad (3.4)$$

where n_i^0 is the refractive index when P is zero, g is the quadratic electro-optic coefficient, $i=1$ or 3 when 1 stands the direction perpendicular to the polarization, 3 stands the direction along the polarization. The refractive index depends on the parameter of polarization P and quadratic EO coefficient g . The value of g_{33} of SBN is about 3 times of that of g_{13} and both of g_{33} and g_{13}

are temperature independent [Imlau, 2006; Burns, 1983]. This explains why the longitude thermo-optical coefficient dn_{TM}/dT is about 3 times of that of transverse thermo-optical coefficient dn_{TE}/dT at corresponding temperature. In order to confirm these observed phenomena, the three dimensional random field Ising model (RFIM) was employed to calculate the temperature dependence of the polarization [Granzow, 2004]. SBN, as one of the typical relaxor ferroelectrics, are polar with glassy or domain state properties at low temperatures, while becomes nonpolar paraelectrics at high temperatures [Kleemann, (2002)]. For $T < T_c$, local dipoles interact to form stable ferroelectric domains, while at $T > T_c$ they are only loosely correlated into polar clusters, which are thermodynamically unstable at infinite times. For most applications it is favorable to work as close to the transition temperature as possible without exceeding it, since most physical effects reach a maximum at the transition from the ferroelectric into the paraelectric state. Based on the RFIM, predictions based on critical exponents are possible. According to thermodynamic theories, a phase transition can be described by a constant set of critical exponents, which are well determined and unchangeable in a single system. This critical behavior is an inherent property caused by the interaction of the system's constituent parts. In this context, the behavior of the order parameter, the spontaneous polarization P ,

over the temperature T is of special interest. Below the phase transition temperature it is described by the equation:

$$P(T) = P_0 \left(1 - \frac{T}{T_c}\right)^\beta \quad (3.5)$$

with the critical exponent β . In the RFIM, the β is 0.125 for fully poled SBN epitaxial film [Granzow, 2004].

Combining (3.4) and (3.5), the temperature dependence of the refractive index can be obtained, as shown in Fig. 3.23. In the range below Curie temperature, the data of experiment is well consistent with that of calculated data. But since the Ising model can't be used to calculate the polarization above the Curie temperature, the experiment data is deviated separated from the theoretical data in this range.

Table 3.1 shows the thermo-optical coefficients of some usual thermo-optical materials. Comparing with these materials especially such as silicon and some other polymers which are commonly used in thermo-optical waveguide applications, epitaxial SBN thin films have larger thermo-optical coefficient around transition temperature, indicating the possible application of SBN film in this field. Figure 3.24 shows the mode spectra and their enlarged figure at room temperature and around Curie temperature. It clearly shows that the

reflected optical intensity at a fixed angle of incidence can be modulated through changing the temperature of the films. In the TM mode, the intensity drops about 60 percent through changing the temperature by ~ 100 °C. On the basis of our results, it is shown that the ferroelectric materials are potential candidates for thermo-optical modulator. In the range of Curie temperature, the modulator has high efficiency compared with traditional Si [Cocorullo, 1999].

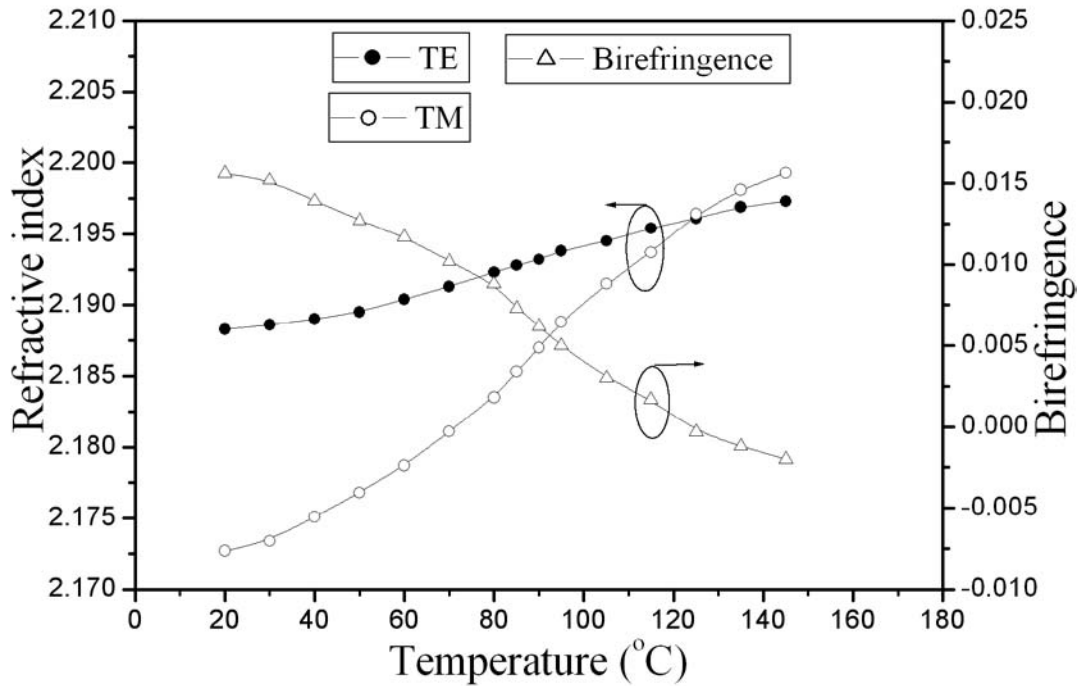


Fig. 3.21 Temperature dependence of refractive index of SBN films on fused quartz.

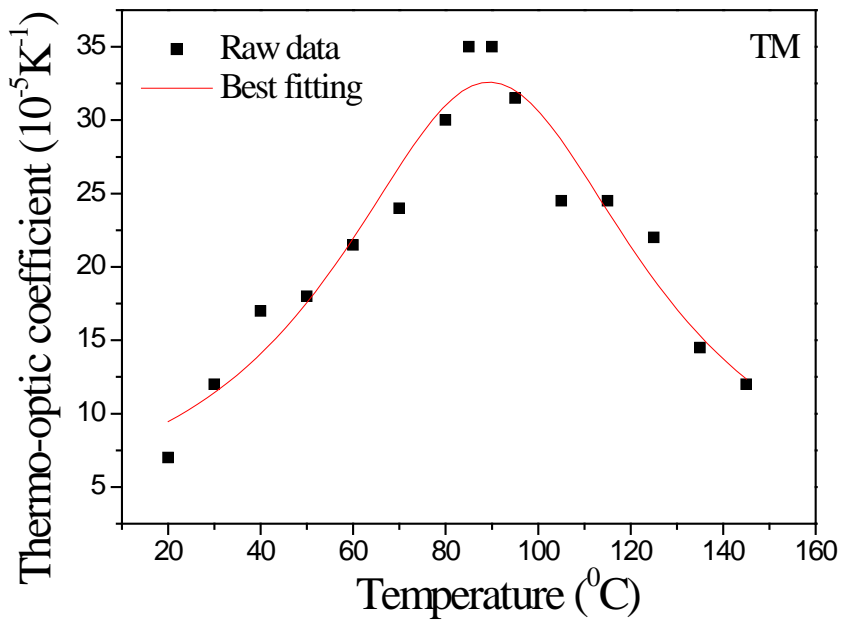
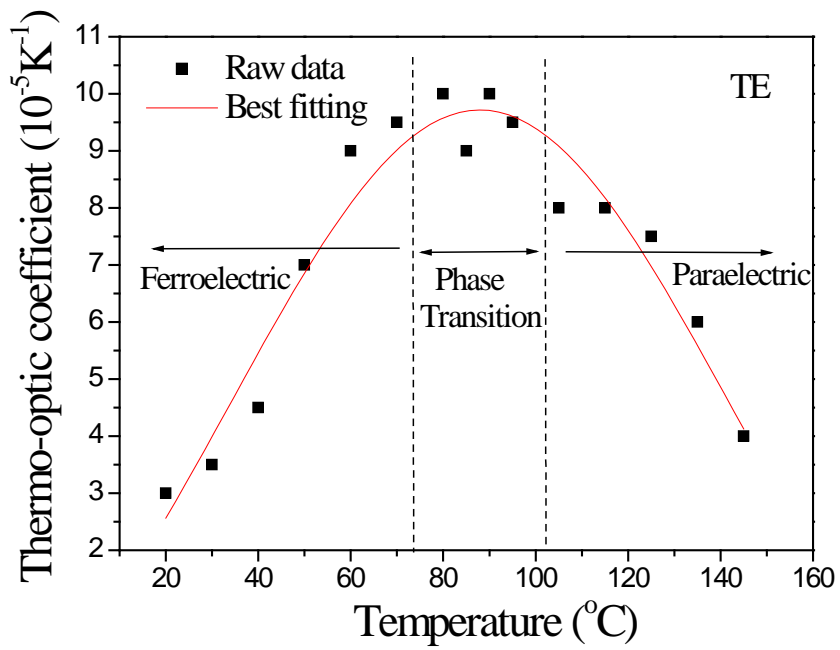


Fig. 3.22 Temperature dependence of thermo-optical coefficient of SBN films on MgO.

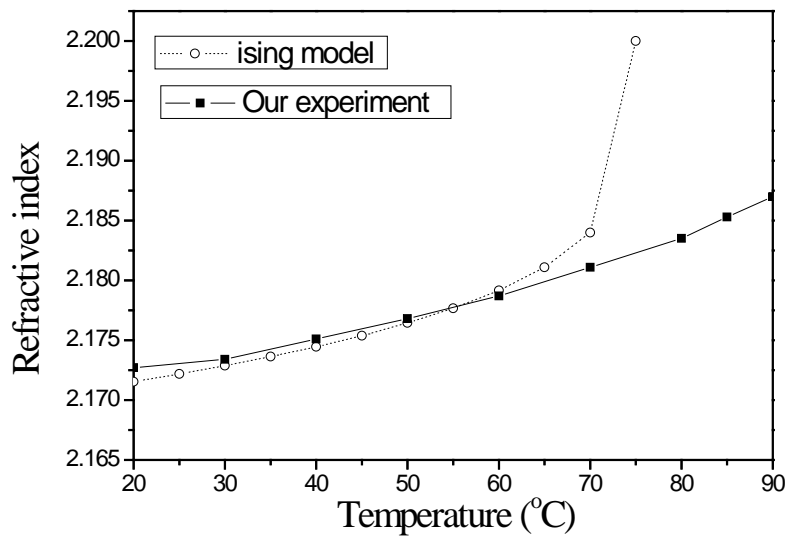


Fig. 3.23 Experimental and theory data of temperature dependence of refractive index.

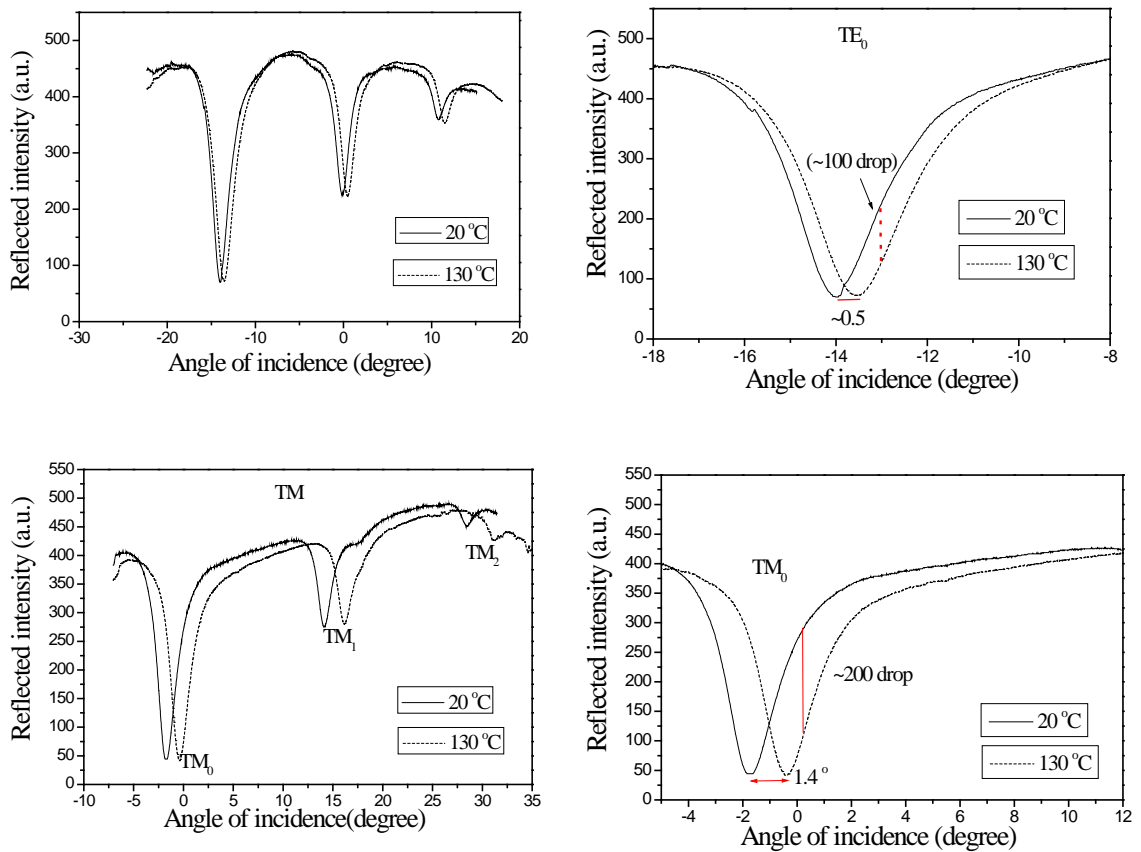


Fig. 3.24 The mode spectrum and their enlarged figure at room temperature and Curie temperature.

Material	dn_o / dT ($10^{-6}/K$)	dn_e / dT ($10^{-6}/K$)	Reference
KNbO ₃	---	160	[Pliska, 1995]
LiTaO ₃	10	100	[Cordo-Montalvo, 1981]
BaTiO ₃	~---	140	[Rush, 1991]
Si	~200		[Cocorullo, 1999]
BPDA/PDA (polymer)	-60	-101	[Terui, 2003]
SBN	~100	~300	[Present work]

Table 3.1 Thermo-optical coefficients of some TO materials.

3.3.4 Conclusion

In this section, the temperature dependence of refractive index of SBN thin films was investigated using a prism coupler technique. A thermo-optical coefficient at the order of 10^{-4} was measured. Three dimension random field Ising model was used to explain these experiment data. On the basis of our results, we demonstrate that SBN is a potential candidate for the thermo-optical modulator.

3.4 EO coefficient measurement of SCNN/fused quartz

3.4.1 Introduction

Based on the shift of the synchronous angles of the guided modes, we have developed a simple method to investigate the effective electro-optic coefficient using two co-planar electrodes.

3.4.2 Structural characterization

Figure 3.25 shows the XRD spectra of the SCNN targets and the as-deposited SCNN films. For Fig. 3.25 (a), all the diffraction peaks originate from the TTB phase of bulk SCNN. No other phases are observed, indicating that the targets are of single phase. For the as-deposited films, peaks corresponding to the TTB phase of SCNN with weaker intensities are observed. No preferred orientations are identified, demonstrating that the films are polycrystalline. The weak broad background at the small 2θ angles observed in Fig. 3.25 (b) is probably due to the amorphous state of the fused quartz substrates. Hence, the SCNN films on fused quartz present a polycrystalline structure and have a pure TTB phase with cell lattice parameters of $c = 3.899 \text{ \AA}$ and $a = b = 12.495 \text{ \AA}$. Inset of Fig. 3.25

displays the surface morphology and cross-section views of the SCNN films using SEM. Dense rod-like grains with random orientations are observed on the surface of the films, indicating that the films are polycrystalline. The interface of the substrate and the SCNN film is quite clear and no obvious interdiffusion is observed. This is important for the waveguide structure as this helps the laser beam to be confined in the SCNN waveguiding layer and thus reduces the propagation loss due to interface scattering. From the cross-section view, the film's thickness is determined to be about 480 nm, which is in good agreement with that obtained from the prism coupler study.

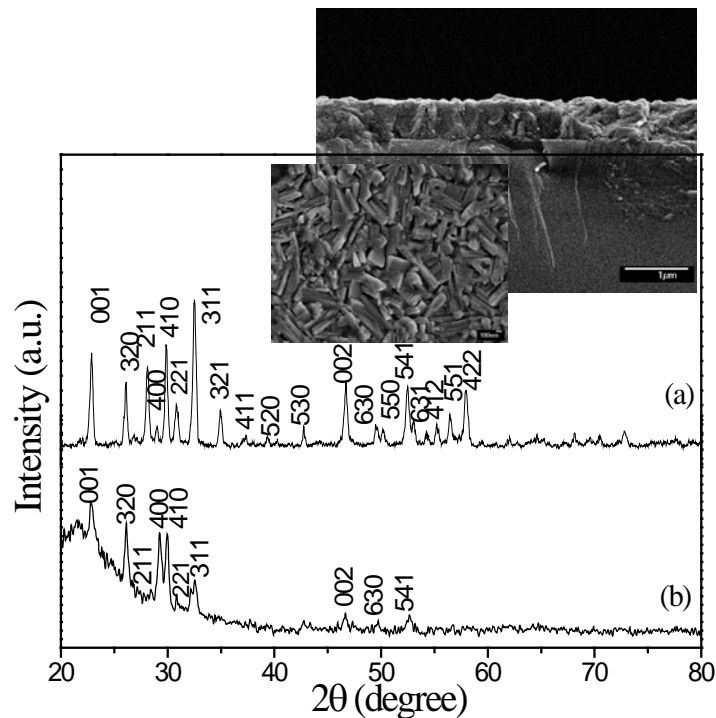


Fig. 3.25 X-ray θ - 2θ scans of (a) SCNN ceramic and (b) thin films deposited on fused quartz substrates. The inset is SEM surface and cross-section image of the SCNN films on fused quartz.

3.4.3 Transmission and E-O measurement

The optical transmittance spectrum of the SCNN thin films are shown in Fig. 3.26. The well oscillating optical transmittance in the visible region is caused by the interference between reflections from the top and bottom interfaces of the films, demonstrating that the films possess flat surfaces/interfaces as well as uniform thickness. For wavelengths longer than 300 nm, the films are transparent with transmission of ~ 80%. The optical band-gap was determined. This 3.9 eV value is slightly larger than the 3.1 eV obtained for the SCNN single crystal.

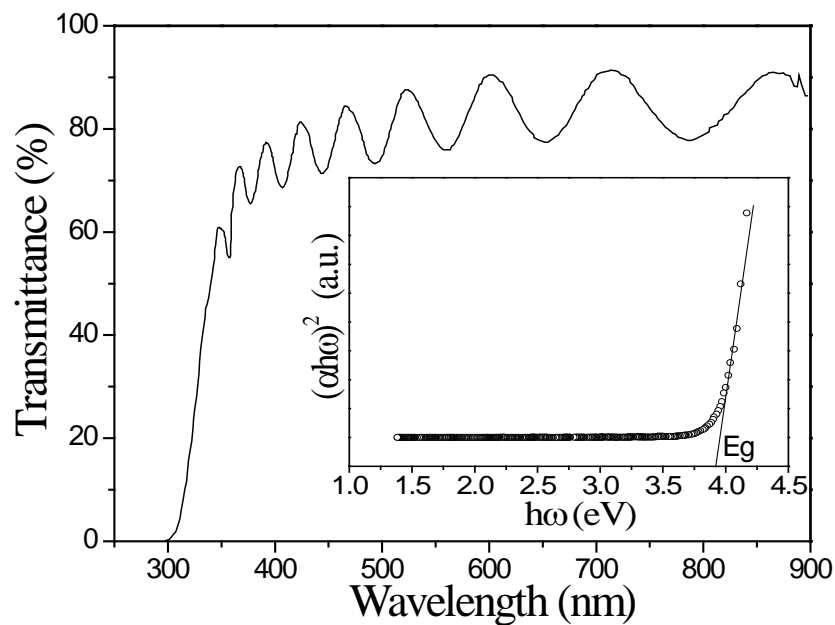


Fig. 3.26 The wavelength dependence of transmittance for SCNN films on fused quartz. Inset is plot of $(h\omega\alpha)^2$ as a function of $(h\omega - E_g)$. Extrapolating the line to intersect with the energy axis, E_g was obtained.

The refractive indices and effective EO coefficient of the SCNN films were examined by using a prism coupler method. Insets of Fig. 3.27 (a) and (b) display the digital camera captured pictures of excited transverse electric (TE) and transverse magnetic (TM) mode-lines obtained at 632.8 nm, respectively. From the photographs, it is noticed that both TE and TM mode-lines are sharp and distinguishable, indicating that a good confinement of light propagation is achieved in our films. In our measurements, the refractive indices of the SCNN films are found to be 2.251 and 2.237 for the TE- and TM-modes, respectively. Obviously, the randomly orientation in the polycrystalline films have small strain between films and substrates, resulting in a small birefringence, that is, a small difference between n_{TE} and n_{TM} (0.014). Compared to that of epitaxial SCNN films grown on MgO of 0.095 [Liu, 2006], the birefringence of SCNN films on fused quartz is six times less. The film thickness is 450 nm. This value is close to that obtained from SEM micrograph. Optical loss, which critically affects the performance of film devices, is a key parameter for waveguide. By measuring the scattered light intensity as a function of propagation distance, the propagation loss at TE₀ mode of the SCNN films was shown to be 2.28 dBcm⁻¹.

Some groups reported the measurements of EO coefficients (γ_{33}, γ_{13}) using the prism coupler technique, with EO layers sandwiched by a top and a bottom

electrodes [Khartsev, 2005; Boudrioua, 1999]. This configuration, however, has two main flaws: a) it needs one relatively large top electrode (about $2 \times 8 \text{ mm}^2$), thus, makes the EO layer to be charged easily, and b) this configuration is not popular in designing the EO modulator devices. Therefore, in this section, we introduce another method based on the prism coupler technique to measure the EO coefficient. Two parallel strips of semi-transparent Pt co-planar electrodes (of thickness $< 30 \text{ nm}$) were deposited on the sample surface using PLD. The distance between the two electrodes was fixed at $500 \text{ }\mu\text{m}$. This co-planar electrodes configuration (inset of Fig. 3.27 (a)) has been widely used in EO phase modulators or interferometric switches, and therefore is of great interest to scientists and engineers [Matsunaga, 2006; Shames, 1998]. In this configuration, the change induced by an applied external field is related to the EO coefficients through the relation [Boudiombo, 1999]:

$$\Delta n = -\frac{1}{2} n_f r_{i,3} E \begin{cases} f = o, e \\ i = 1, 3 \end{cases} \quad (2)$$

where E is the applied electric field and n is the refractive index. The derivation of expressions for refractive index in terms of the EO coefficient r_{13} shows that one can obtain r_{13} using transverse electric polarizer light (o) and r_{33} with transverse

magnetic polarizer light (e) using *c*-axis oriented samples sandwiched by top and bottom electrodes, or effective EO coefficient r_{eff} using co-planar electrodes [Boudiombo, 1999]. As the SCNN films grown on quartz are polycrystalline, only effective EO coefficient is of great interested. As shown in Fig. 3.28 (a), without applying any voltage, a clear coupling curve with two sharp dips is obtained. By applying a voltage across the electrodes and using light with the same polarization, another coupling curve with similar features and slight shift of the dips' positions, is observed. By using different voltage values ranging from 0 to 1100 V, the shifts in the position of the guided modes and hence the changes in the refractive index are measured. Figure 3.28(b) represents the linear Pockels EO effect observed in our experiment. It shows a linear variation of the refractive index n_e , for the TM modes. Using the relation (2) and the measured slope of Fig. 3.28(b), the effective EO coefficient r_{eff} is found equal to 176.6 pm/V. It is noticed that the determination of the effective EO coefficients r_{eff} ($r_{\text{eff}} = r_{33} - (n_o / n_e)^2 r_{13}$) with co-planar electrodes configuration depends on amount of overlapping between the optical electric field $E(\text{opt})$ associated to the TM modes and the electric field E_z produced by the electrodes. This made the measured data to be smaller than r_{33} of SCNN bulk single crystal (1350 pm/V) [Neurgaonkar, 1988], and consequently the accuracy of the EO coefficient value is rather limited.

However, this method is simple and straight forward for obtaining the effective EO coefficient. Finally, our results clearly demonstrate that the SCNN/fused quartz structures are potential candidate for optical waveguide applications.

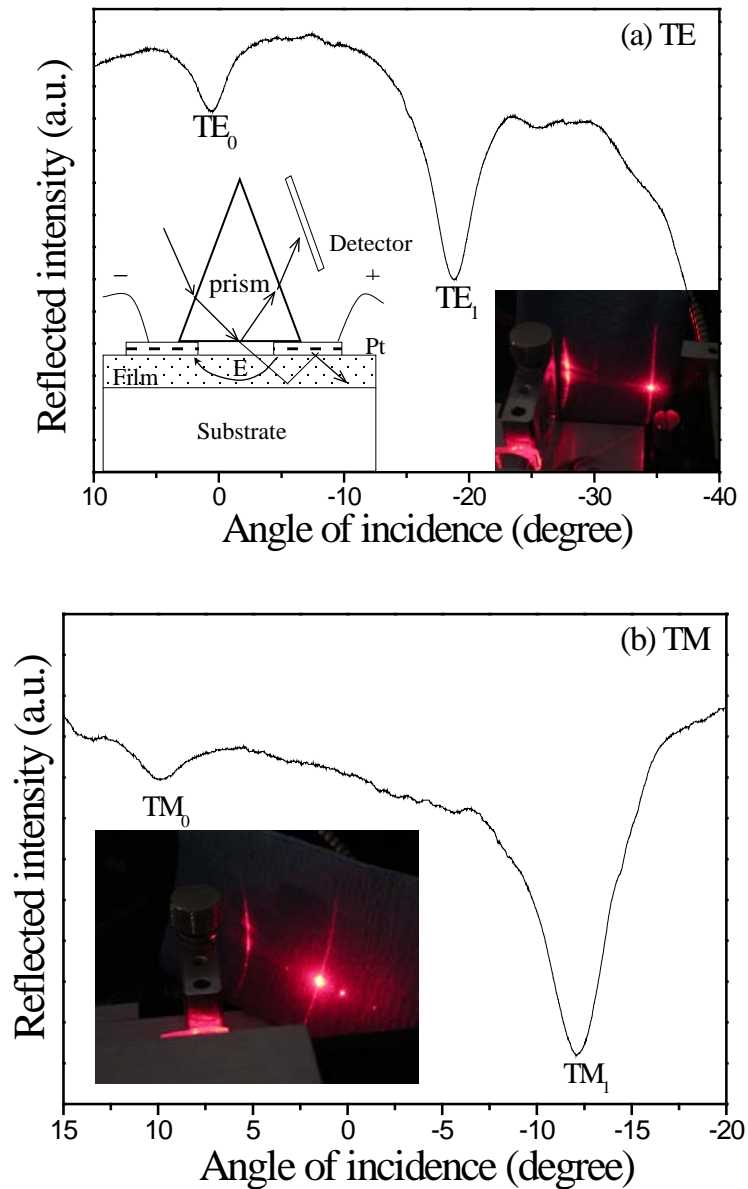


Fig. 3.27 Excited (a) TE-line and (b) TM-line (lower plot) spectra for the air/SCNN/fused quartz waveguiding structure. The left inset (a) shows the schematic diagram of the set-up for measuring EO coefficient. The inset in (a) and inset in (b) are the digital camera captured photographs of excited TE mode-lines and TM mode-lines at 632.8 nm, respectively.

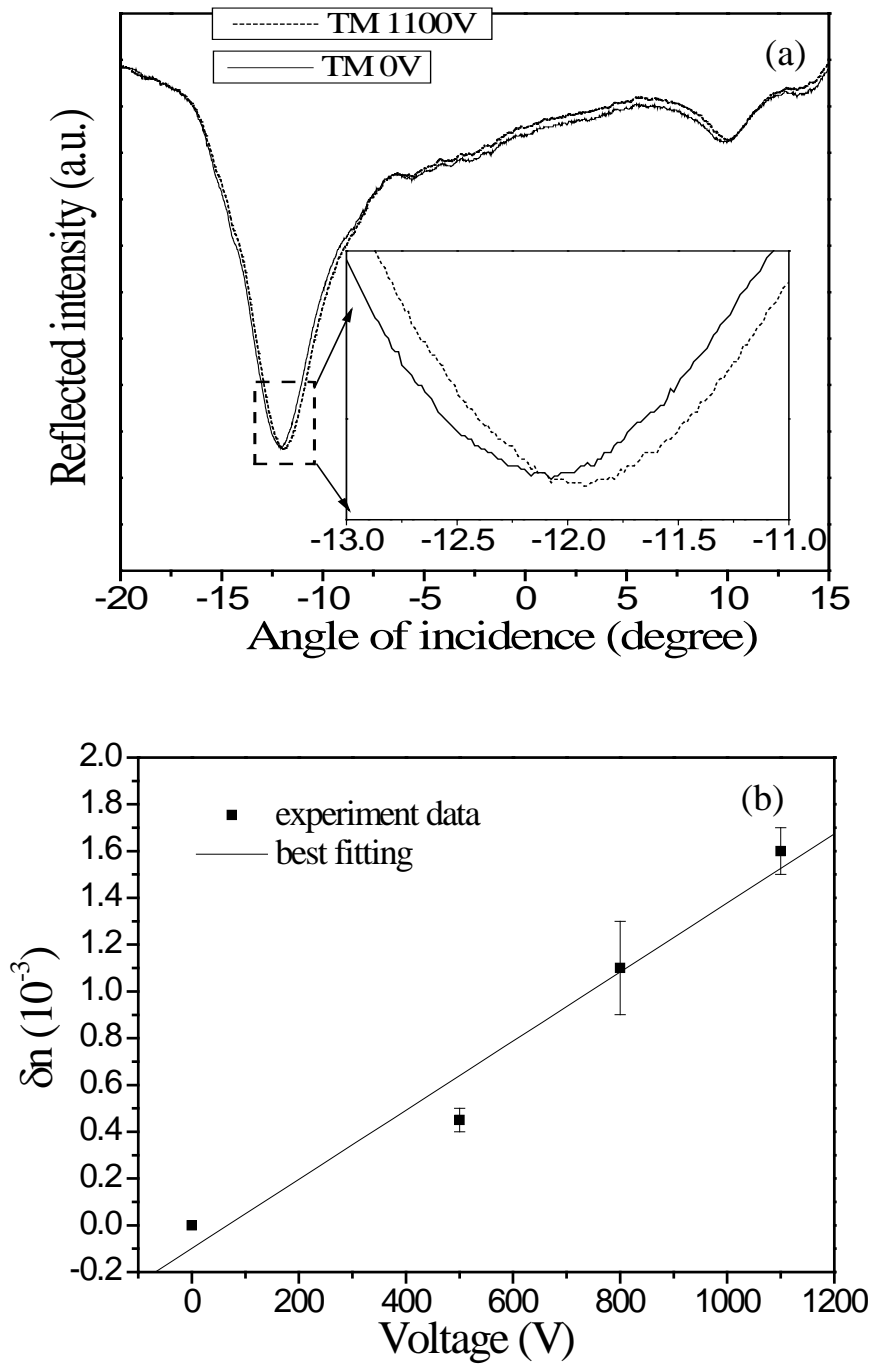


Fig. 3.28 (a) Reflectivity mode line curves measured with TM polarized light with (dot line) and without (solid line) an applied voltage. (b) Added voltage induced displacement of the refractive index.

3.4.4 Conclusion

Good quality tetragonal tungsten-bronze structure polycrystalline SCNN films with high transparency and large refractive index were successfully deposited on fused quartz by pulsed laser deposition. The as-grown films had an optical transmittance of 80% in the range of 400–900 nm. The optical band gap of the SCNN films was found to be 3.9 eV. Sharp and distinguishable excited mode lines were observed in the prism coupler measurements, indicating that a good confinement of light propagation is achieved in our planar waveguides. The transverse electric (n_{TE}) and transverse magnetic (n_{TM}) refractive indices of the SCNN/quartz films are determined to be 2.251 and 2.237, respectively, with a relatively small index difference of 0.014 due to the randomly oriented polycrystalline isotropic structure. The effective EO coefficient r_{eff} of SCNN thin films was measured to be 176.6 pm/V by using a simple prism coupler method with co-planar electrodes. The results suggest the feasibility of modulation devices using SCNN ferroelectric thin films for integrated optic.

3.5 A potential application of prism coupler technique: Roughness sensor

3.5.1 Introduction

The increasing need for non-destructive surface and interface characterization providing information about the materials microstructure has stimulated interest in looking for suitable characterization method. AFM is one of the most popular methods used to observe the surface morphology and roughness of the samples. In this chapter, we tried to characterize the surface morphology of SCNN films using a new method: prism coupler technique. A complete optical characterization based on prism coupler technique was proposed to carefully establish a relationship between the surface morphology and the optical information such as FWHM of excited guided-modes. The evolution of the surface roughness as a function of the SCNN films was comparable to that of the FWHM of TE guided-modes.

3.5.2 Results and discussion

As described in chapter 2.2, the SCNN thin films deposited at different temperature present different roughnesses. The roughness increases with the increase of deposition temperature. Here, the prism coupler technique was used to characterize the surface morphology of these deposited SCNN films. Reflectivity dips indicate the excitation of specific modes in the SCNN film. The sharpness of the dips is a good indication of light confinement into waveguide. The extracted energy from the reflected beam leads to sharp or mild dips in the reflectivity curve and it is believed that this is related to the film morphology. In this section, we have measured the FWHM of TE_0 guided modes of SCNN films deposited at different temperature and investigated the relationship of FWHM and roughness of these films.

With increasing the surface roughness of SCNN films, the scattering of light by the surface roughness change in the width of TE modes. This behavior was similar with that observed by AFM. A correlation can be exhibited between the angular width of the optical modes as expressed by the FWHM and the surface roughness, as shown in fig. 3.29. So, it suggests that prism coupler technique can

be used as a sensitive surface probe. The developed optical method based on prism coupler could be favorably compared to the AFM with a good accuracy.

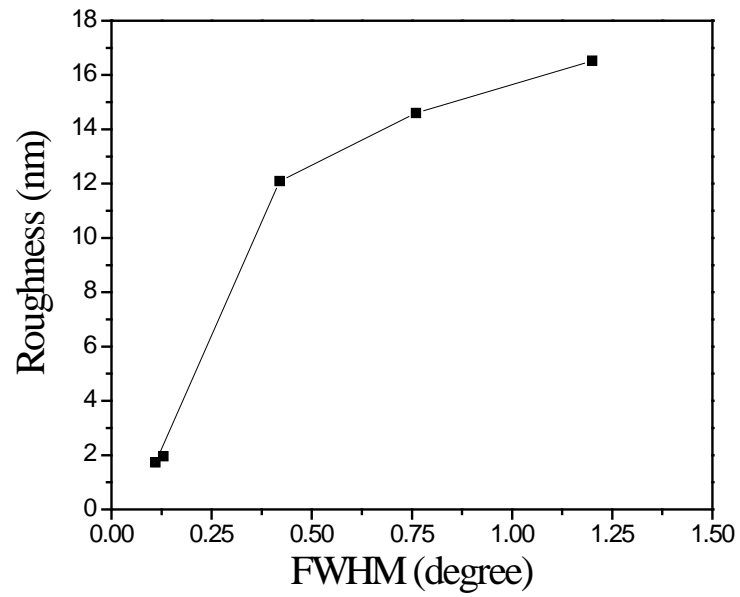


Fig. 3.29 Evolution of FWHM of the TE_0 excited guided-mode with roughness of SCNN films.

4 Raman and Brillouin scattering

investigation of SBN and SCNN thin films

4.1 Phase transition investigation of the epitaxial $\text{Sr}_{1.9}\text{Ca}_{0.1}\text{NaNb}_5\text{O}_{15}$ film using thermo-Raman scattering

Epitaxial ferroelectric $\text{Sr}_{1.9}\text{Ca}_{0.1}\text{NaNb}_5\text{O}_{15}$ (SCNN) thin films have been fabricated successfully by pulsed laser deposition on (100)MgO substrates. Temperature dependency of the vibrational modes of these films was investigated for the first time using Raman scattering technique. For temperatures ranging between 50°C and 450°C, two strong and broad A1(TO) phonons around 238 and 608 cm^{-1} , and one weak B1(TO) phonon around 142 cm^{-1} were observed. Changes in the temperature dependency of the peak position, the FWHM and integrated intensity of the Raman modes were studied in different temperature ranges. These changes are attributed to the structural phase transitions between 200 °C and 325 °C for the SCNN films as well as their relaxor properties.

4.1.1 Introduction

Being TTB ferroelectrics, SCNN has one close ancestor in this family, $\text{Sr}_{1-x}\text{BaNb}_2\text{O}_6$ (SBN). With similar structure, SCNN inherits SBN's large EO coefficient. By adding Na into the void site of SBN, the Curie temperature of SCNN is substantially increased. From the crystallographic point of view, TTB structure has a general formula $(\text{A1})_2(\text{A2})_4\text{C4}(\text{B1})_2(\text{B2})_8\text{O}_{30}$, where A is a divalent or monovalent metal, B is either Nb or Ta, and C is usually empty or occupied by small metals, as shown in Fig. 4.1. In SCNN, C sites are empty and Nb is placed at B sites, while A1 sites are fully occupied by Sr and Na and A2 sites are fully occupied by Sr and Ca in a disordered form [Jiang, 2005]. SCNN crystallizes in a tetragonal structure belonging to the $P4bm$ (C_{4v}^2) space group, where Nb cations have six-fold coordination originating two families of NbO_6 octahedra, which occupy sites with C_{2v} or C_1 symmetry. As we know, in partially occupied structure material, such as SBN, it is much disordered because Sr and Ba ions are distributed randomly and a one-sixth fraction of A-sites remains vacant. SCNN, however, has a fully occupied structure. The introduction of Na into the vacant sites decreases the disorder of the structure. Furthermore, the appropriate substitution of Sr^{2+} ions (1.44 Å) by smaller Ca^{2+} ions (1.34 Å) in SCNN enhances the structural distortion, and results in an increment in spontaneous polarization and related properties.

Thus, SCNN presents many interesting physical phenomena especially in phase transition owing to the competition of the order and disorder structure. Neurgaonkar et.al, for the first time, reported the fabrication and temperature dependence of dielectric constant of the SCNN single crystals [Neurgaonkar, 1988]. It undergoes a ferroelectric phase transition at T_c (270 °C), changing the point symmetry from $4/mmm$ (paraelectric) to $4mm$ (ferroelectric). At 100°C, it experiences a ferroelastic transition from the $4mm$ phase (ferroelectric) to the orthorhombic $2mm$ phase (ferroelastic). Xie et.al showed that the SCNN ceramics exhibited a typical but less pronounced diffuse phase transition by means of probing the temperature dependence of its dielectric constant. One ferroelectric phase transition at 270 °C was observed, while the ferroelastic transition was appeared at about 0 °C, instead of 100°C [Xie, 2002]. Up to now, there are limited reports about the phase transition of SCNN thin films. In order to exploit the anisotropic properties as well as to fabricate integrated optical devices, it is desirable to grow single-crystal thin films. Thus, it is valuable to investigate the transition behavior of these highly oriented or epitaxial thin SCNN films. Different from the previous classical method to characterize the phase transition by means of dielectric constant measurement [Xie, 2002], in this chapter, we investigated, for the first time, the temperature induced ferroelectric to paraelectric

(F-P) phase transition of epitaxial SCNN thin films using thermo-Raman spectroscopy, which is a powerful and sensitive technique used to study the crystalline structures based on the vibrational bands. Thermo-Raman spectroscopy is an important tool in studying phase transformation as it records the variation in vibrational modes as a function of temperature.

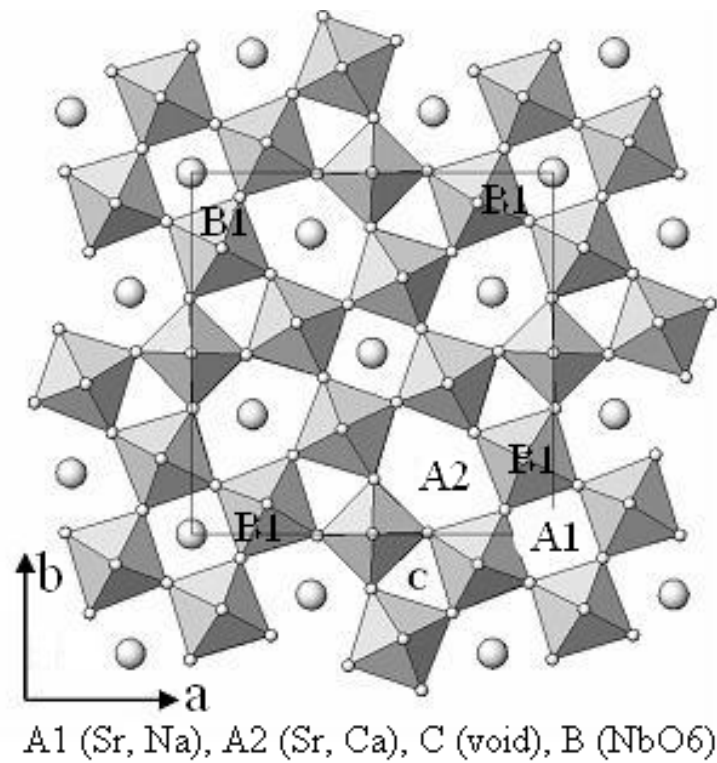


Fig. 4.1 Schematic representation of the structural skeleton of the TTB type structure projected on the *a-b* plane. Square, pentagonal, and triangular tunnels available for cation inclusion can be observed.

4.1.2 Experimental details

Epitaxial SCNN films were grown on single crystal MgO (100) substrate of size $10 \times 5 \times 0.5 \text{ mm}^3$ by pulsed laser deposition (PLD), as described in chapter 2. Raman spectra were taken using 488 nm laser line of an air cooled Ar-ion laser. A microscope was used to focus the incident laser beam to a spot of about 100 μm in diameter. Raman spectra were recorded by a 100 \times lens system in back scattering geometry using a Horiba Jobin Yvon HR800 spectrometer with a charge-coupled device (CCD) detector. The samples were mounted on a heating stage with the temperature varying between 25 - 450 $^{\circ}\text{C}$.

4.1.3 Raman scattering results and discussion

The epitaxial relationship of the SCNN film grown on MgO (100) substrate was confirmed in Chapter 3. The unpolarized room temperature Raman spectrum in the vicinity of the optical phonon frequencies of the epitaxial SCNN film is presented in Fig. 4.2. The MgO substrate has no Raman lines in the spectral range studied and therefore it does not interfere with the spectrum of the SCNN film. Two broad and strong A₁(TO) phonons at 238 and 608 cm⁻¹ and one weak B₁(TO) phonon at 142 cm⁻¹ are observed. The broad 2 A₁ (TO) modes are similar to the 248 and 628 cm⁻¹ modes observed in LiNbO₃ and to the 260 and 630 cm⁻¹ modes reported for SBN [Barker, 1967; Ho, 1999]. These Raman bands are related to the Nb-O vibrations in NbO₆ octahedra. The weak modes at 543, 383 and 281 cm⁻¹ arise from the Ca-O and Sr-O bending more or less with the Nb-O bending vibrations, as described in ref [Husson, 1977; Amzallag, 1971]. Since SCNN has two formula units per primitive tetragonal unit cell, there should be at most 135 normal optical phonon modes (3*2*23-3) in SCNN. With this large number of phonon modes, it is possible that several nearly degenerate modes may occur and appear as one band [Burns, 1969]. This degeneracy would contribute to the broadening of the band and asymmetric line-shape. Another reason that the Raman lines are fairly broad comes from the fact that the crystal

structure is partly disordered. Compared to the Raman spectrum of partly filled SBN, the peaks at 238 and 608 cm^{-1} are relatively narrow, it is because that in SCNN the structure is fully filled, inducing less disorder compared to SBN, where five combined Ba and Sr atoms are required to be distributed over six A sites in the TTB unit cell.

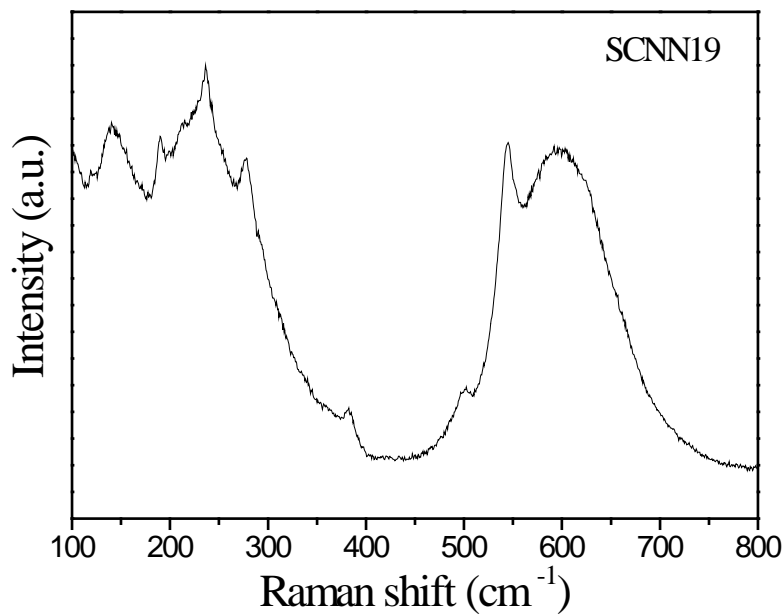


Fig. 4.2 Room temperature Raman spectrum of SCNN.

As observed in Fig. 4.2, the SCNN Raman spectrum is dominated by a broad and intense peak around 608 cm^{-1} and another intense peak at around 238 cm^{-1} . These two modes are polarized along the ferroelectric c axis, and so it is expected that these peaks should be the most appropriate to probe the F-P phase transition, as during the phase transition, the most important changes occur along this axis.

Among these two modes, the peak at 608 cm^{-1} is too broad and the peak position is difficult to be determined easily. In this thesis, we focus on the 238 cm^{-1} peak and investigate the temperature dependence of this peak. Figure 4.3 shows the temperature dependence of 238 cm^{-1} mode. Inspection of Fig. 4.3 reveals that the peak is observable in the measured temperature range, and is different from the spontaneous polarization which goes to zero above T_c . This means that the A_1 symmetry modes, which are mostly associated with motions of the NbO_6 octahedrons, are still active even at temperatures much higher than T_c . We notice that this peak broadens with temperature, and at the same time, it softens with the increase of temperature.

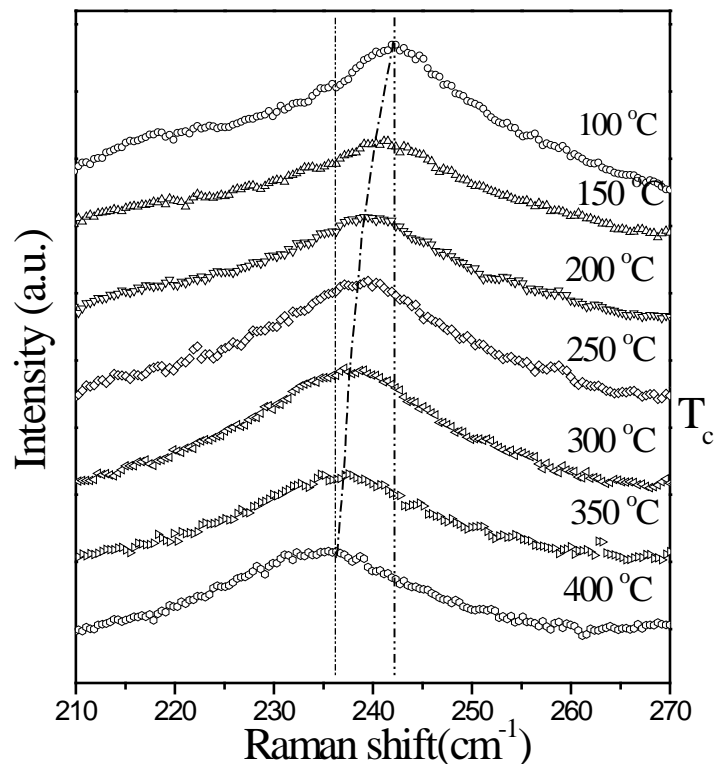


Fig. 4.3 Temperature dependence of the Raman spectra of the main mode (at around 238 cm^{-1}) for the SCNN film.

We have systematically investigated the temperature evolution of the peak position as well as FWHM of the 238 cm^{-1} phonon mode of the epitaxial SCNN film. The temperature dependence of the Raman shift shown in Fig. 4.4(a) suggests that clear anomalies occur at temperatures around T_c . General speaking, the Raman peak shifts to lower wavenumbers with increasing temperature, displaying an almost linear dependence, for most of the materials. However, for our experimental results, we notice that slope of the linear decrease in the ferroelectric phase is different from that in the paraelectric phase. This observation is in good agreement with the Raman measurements reported on SBN single crystal and $\text{PbBaNb}_2\text{O}_6$ ceramics [Speghini, 2006; Lima-Silva, 2004]. It is suggested that whole range is split into two ranges: one ferroelectric phase below $270\text{ }^\circ\text{C}$ and one paraelectric phase above it. The rates of this thermally induced softening for the two regions are clearly different: $0.024\text{ cm}^{-1}\text{ C}^{-1}$ for the ferroelectric phase and $0.009\text{ cm}^{-1}\text{ C}^{-1}$ for the paraelectric phase. Similar anomalies around T_c are experimentally observed when following the temperature evolution of the FWHM of the same 238 cm^{-1} band (Fig. 4.4(b)). The FWHM increases near linearly below $270\text{ }^\circ\text{C}$ and then increases linearly with a larger slope after $270\text{ }^\circ\text{C}$. Similar to the peak position, this band broadens linearly with temperature and the slope of broadening is different in different regions.

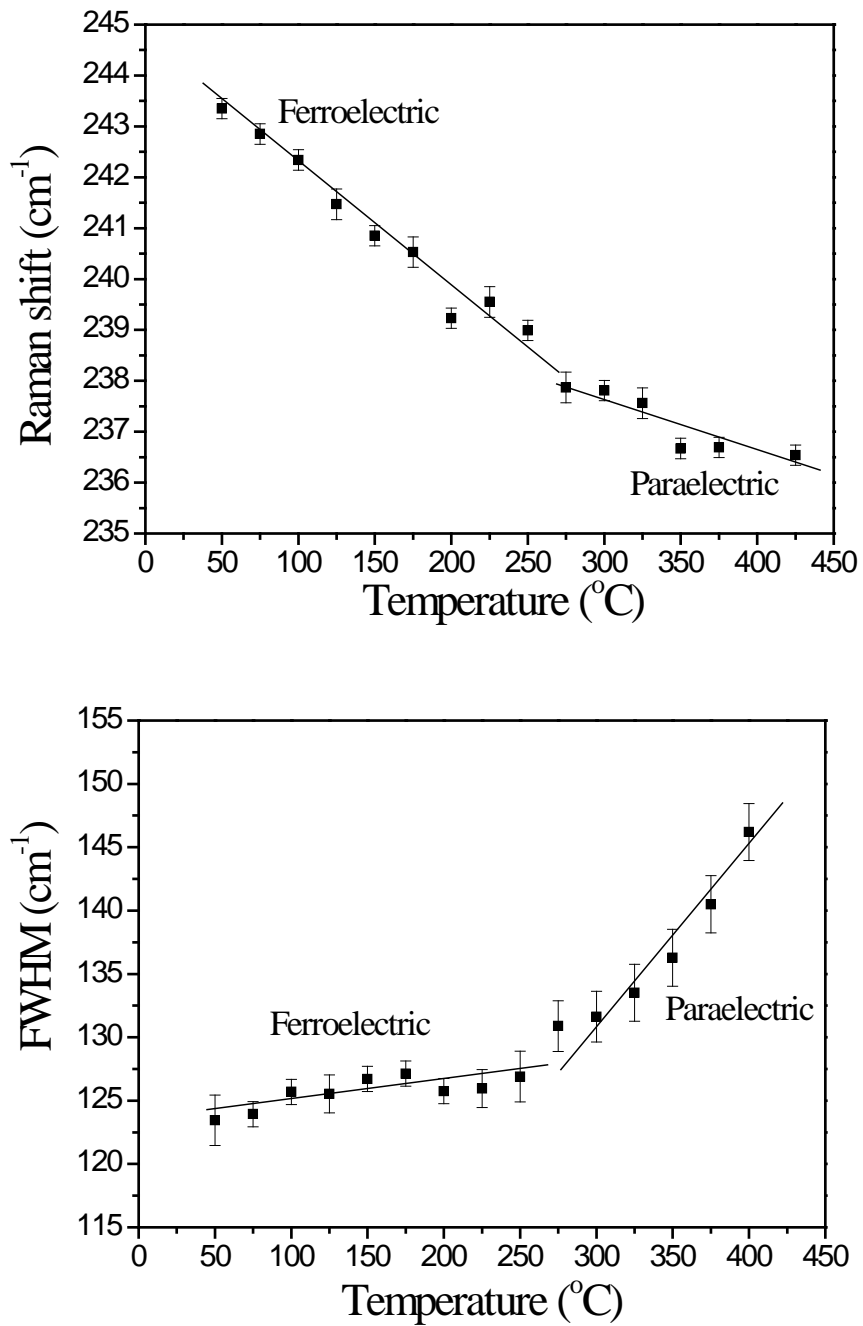


Fig. 4.4 Temperature dependence of the (a) Raman shift and (b) full width at half maximum (FWHM) of the main mode (at around 238 cm⁻¹) for the SCNN film.

Let us explain why the 238 cm^{-1} Raman peak still exists at temperatures much higher than the Curie temperature. The 238 cm^{-1} broad Raman band is related to internal modes of the two octahedra (those related to the B_1 and B_2 positions). Therefore, the temperature induced changes in that Raman band should be due to the changes experienced by the NbO_6 octahedra [Xia, 1998]. According to the SCNN formula, in the ferroelectric phase, 2 out of 10 Nb^{5+} ions lie in B_1 positions (C_{2v} symmetry, five A_1 modes are Raman active), while the other 8 lie in B_2 positions (C_1 symmetry, all modes are Raman active), both being distorted octahedral sites. In order to account for the different thermal softening and broadening observed around the phase transition temperature, together with the displacive effects associated with the NbO_6 octahedrons, the symmetry changes of the corresponding B_1 and B_2 sites when undergoing from ferroelectric to paraelectric phase should be considered. In the transition process from ferroelectric to paraelectric phase, the B_1 sites change from C_{2v} to D_{2h} symmetry gradually with the increment of the temperature, while the B_2 sites remain in its C_1 symmetry [Jamieson, 1968]. Thus, though the Raman modes related to Nb^{5+} at B_1 sites disappear gradually, those related to Nb^{5+} in B_2 sites are still Raman active, i.e. there are still some active modes remains in the paraelectric phase, but the number of the active Raman modes varies considerably. This explains why the

Raman band at 238 cm^{-1} survive in the paraelectric phase but the slope of the change of Raman shift is different after phase transition.

4.1.4 Conclusion

The chapter reports, for the first time, the temperature dependence of Raman spectra of calcium-modified strontium sodium niobate films across the ferro-paraelectric phase transition. The temperature dependence of the Raman shift and FWHM of the Raman bands present clear anomalies at the phase transition. The Raman band at 238 cm^{-1} survive in the paraelectric phase but the slope of the change of Raman shift is different after phase transition. It is believed that the changes of symmetry of the Nb ion in the NbO_6 octahedral are responsible for the observed change of Raman spectrum.

4.2 Phase transition investigation of the epitaxial SBN60 film using thermo-Raman scattering

4.2.1 Introduction

The outstanding properties and the potential applications of SBN have pushed many instructive studies. Similar with SCNN, SBN also presents relaxor characteristics, such as strong frequency dependence of (T_m) and a broad phase transition temperature. Nevertheless, its relaxor characteristics are also very sensitive to variation of the Sr/Ba ratio and, consequently, to the cationic site occupation on the lattice. The TTB unit cell is shown in Fig. 1.3 in the prototypic tetragonal symmetry $4/mmm$ in the paraelectric phase. The B sites are found in the oxygen octahedra, which are slightly tilted, and are fully filled by niobium atoms. According to this configuration, the TTB cell has three distinct tunnels, which are the 12-fold coordinated A1 (square), 15-fold coordinated A2 (pentagon), and 9-fold coordinated C (triangle) sites. In SBN, the C sites are the smallest and remain completely vacant. The different radii of Sr^{2+} (1.12 Å) and Ba^{2+} (1.35 Å) cations make them preferentially distributed in different A sites. Sr ions prefer A1 sites, while Ba ions prefer A2 sites, respectively. Since there are only five Ba^{2+} and Sr^{2+} cations available for six A sites in the unit cell, there is a

vacancy distributed in the A sites. Furthermore, increasing Sr^{2+} increasing in the SBN composition, more and more Sr^{2+} ions will occupy A2 sites, as well. In other words, the A2 site is disordered in relation to the cationic occupation type. Thus, different from SCNN where the six A1 and A2 sites are fully occupied by metal ions, SBN, is a partially occupied structure material. Fan *et.al.* systematically reported on the dielectric relaxation characteristics of SBN ceramics and confirmed the existence of polar nanoregions in these relaxors [Fan, 1998]. Dec *et.al.*, however, investigated the probing polar nanoregions in SBN60 relaxors via second-harmonic dielectric response and suggested that the appearance of dielectric second harmonic generation may be interpreted as a signature of the polar clusters [Dec, 2003]. Santos *et.al.* reported on the dielectric behavior and diffuse phase transition features of rare earth doped SBN60 ceramics and investigated the effect of doping on the relaxor properties [Santos, 2002]. The first investigation on the phase transition of SBN50 single crystal using thermo-Raman spectra was reported by Bartlett *et.al* [Bartlett, 1973]. All A1 modes soften with the increase of temperature in a large temperature range from 100 K to 500 K. Though much work has been done to investigate the phase transition and relaxor properties of SBN, most of these work focuses on the investigation of SBN bulk materials such as single crystals or ceramics. Thin

films become more and more popular in the field of integrated optics application. Thus, it is important to investigate the phase transitions of high quality SBN thin films. To the best of our knowledge, there have been no reports about the thermo-Raman of SBN thin films. In this chapter, we introduce the temperature dependence of Raman spectra of epitaxial SBN60 thin films and investigate the relationship between the thermo-Raman spectra, phase transition and structure. The epitaxial SBN60 thin films were deposited epitaxially on MgO(100) substrates as introduced in Chapter 3.3.2 and thermo-Raman experimental details were introduced in Chapter 4.1.2.

4.2.2 Thermo-Raman spectra results and discussion

Figure 4.5 shows the temperature variation of the Raman spectra for the epitaxial SBN60 film. Two broad and strong A1(TO) phonons at around 240 and 625 cm^{-1} , one weak B1(TO) phonon at 155 cm^{-1} and one weak B2 phonon at 425 cm^{-1} are observed. Lorentzian profiles were used to fit the line bands. After fitting, both Raman shift of the bands peak and the FWHM of these bands are obtained, as shown in fig. 4.6. Right of fig. 4.6 shows some relative parameters such as peak site and FWHM. Since there are 132 optical phonon modes in the

unit cell, it is possible that several nearly degenerate modes may occur and appear as one band. This degeneracy would contribute to the broadening of the band and asymmetric line-shape. This is similar to the 238 and 608 cm^{-1} modes observed in SCNN as introduced in chapter 4.1 and to the 260 and 630 cm^{-1} modes reported for SBN [Barker, 1967; Ho, 1999]. The 240 and 625 cm^{-1} bands are related to the Nb-O vibrations in NbO_6 octahedra. The weak modes at 155 cm^{-1} and 425 cm^{-1} arise from the Ba-O and Sr-O bending vibrations. In SBN, since the Nb-O distances (ranging from 0.192 to 0.211 nm) are much shorter than the Sr-O and Ba-O distances (ranging from 0.2547 to 0.3035 nm) [Line, 2001; Lima-Silva, 2001], the NbO_6 octahedra (sites B1 and B2) are more strongly bonded than the coordination polyhedra about the Sr^{2+} and Ba^{2+} lattice cations. Thus, the Nb-O vibrations are much stronger than that of Sr-O and Ba-O, which imply the peaks at 425 and 155 are much weaker as compared with the two main modes. This is different with that of SCNN, in SCNN, Ca-O distance (0.23 nm) are smaller than that of Ba-O and Sr-O [Francesc, 2004] and similar with that of Nb-O. Thus, in SCNN some mode peaks related to Sr and Ca-O vibrating are relatively strong and can still be observed. In both SBN and SCNN, several nearly degenerate modes may occur and appear as one band and result the broadening of the band and asymmetric line-shape. Comparing to SCNN, SBN

shows broader main bands. The FWHM of the main mode at 240 cm^{-1} band (160 cm^{-1} at Curie temperature) are larger than that of 240 cm^{-1} band of SCNN (around 130 cm^{-1} at Curie temperature).

The reason that the Raman lines of SBN are relatively broader than that of SCNN originates from the fact that the crystal structure of SBN is partly filled, where five combined Ba and Sr atoms are required to be distributed over six sites in the TTB unit cell. Thus, the structure of SBN is very disordered. In SCNN, however, due to the introduction of Na ions, all six sites are filled by metal ions, thus reducing the disorder degree.

The SBN Raman spectrum is dominated by a broad and intense peak around 625 cm^{-1} and another intense peak at around 240 cm^{-1} . These two modes are polarized along the ferroelectric c axis and the most important changes must be occurred along this axis during the phase transition, so it is expected that these peaks should be the most appropriate to probe the F-P phase transition. In this chapter, we give a systematic investigation about the change of peak position and FWHM of these two peaks with the increase of temperature. Similar with SCNN, as shown in figure 4.6, both of the two main modes can survive in the whole

temperature range of measurement. This means that the A_1 symmetry modes, which are mostly associated with motions of the NbO_6 octahedrons, are still active even at temperatures much higher than T_c . Near the peak position and FWHM of these two modes, we use Lorentzian functions to fit the measured Raman spectra and obtain the relative parameters.

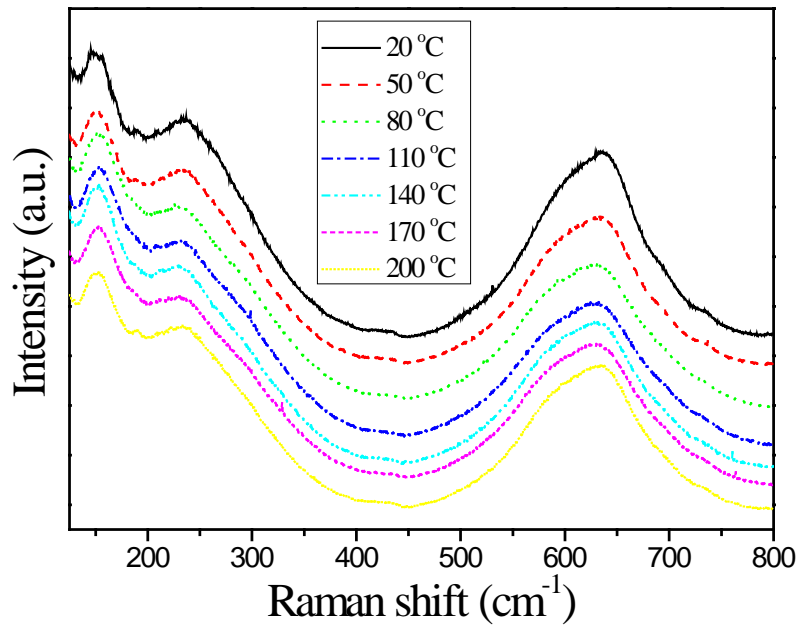


Fig. 4.5 Temperature dependence of the Raman spectra for the epitaxial SBN60 film.

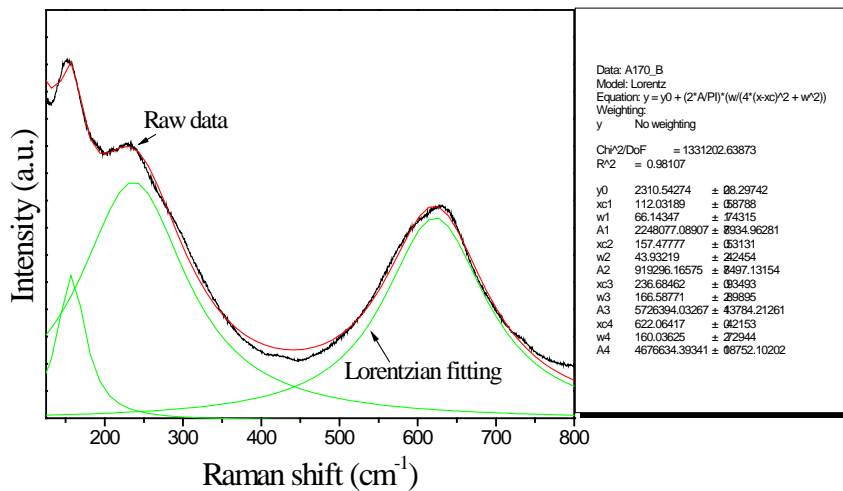


Fig. 4.6 Raman spectra and multi-peak Lorentzian fit at 170 °C for the epitaxial SBN60 film.

The temperature evolution of the peak position as well as the FWHM of the 238 cm^{-1} phonon mode of the epitaxial SBN film were systematically investigated. As shown in fig 4.7 and 4.8, the temperature dependence of both modes exhibits anomaly around the critical temperature. The 625 cm^{-1} mode softens below the phase transition and keep nearly constant above it. The one at 240 cm^{-1} , however, first soften and, above the critical temperature, harden. Similar anomaly around T_c are experimentally observed when following the temperature evolution of the FWHM of two bands (Fig. 4.8(b) and 4.9 (b)). The FWHMs follow a practically linear dependence below 100 $^{\circ}\text{C}$, and then increase linearly with a smaller slope.

Why the 240 and 625 cm^{-1} Raman peaks still exist at temperatures much higher than the Curie temperature? Why the slopes of FWHM and Raman peak position vs temperature before and after Curie temperature are different? The explanation is similar as that described in chapter 4.1. The broadening of the characteristic Raman spectra originates from the distorted octahedral. The 240 and 625 cm^{-1} broad Raman band are related to internal modes of the two octahedra (those related to the B1 and B2 positions). In the transition process from ferroelectric to paraelectric phase, the B1 sites of SBN change from C_{2v} to D_{2h} symmetry gradually with the increment of the temperature, while the B2 sites

remain in its C_1 symmetry. Thus, though the Raman modes related to Nb^{5+} at B1 sites disappear gradually, those related to Nb^{5+} in B2 sites are still Raman active, Thus, there are still some active modes remains in the paraelectric phase, but the number of the active Raman modes varies considerably. This explains why the Raman band at 238 cm^{-1} survives in the paraelectric phase but the slope of the change of Raman shift is different after phase transition.

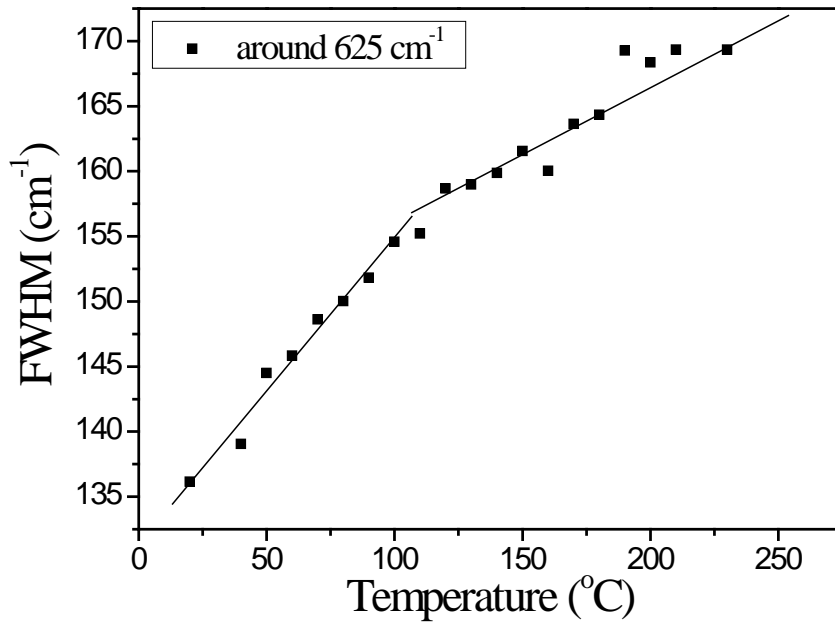
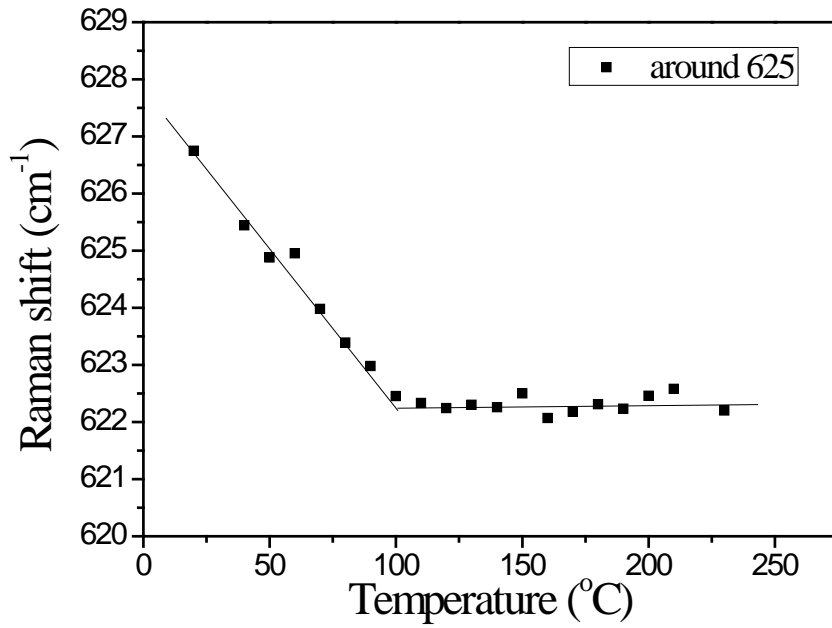


Fig. 4.7 Temperature dependence of the (a) Raman shift and (b) full width at half maximum (FWHM) of the main mode (at around 625 cm⁻¹) for the SBN film.

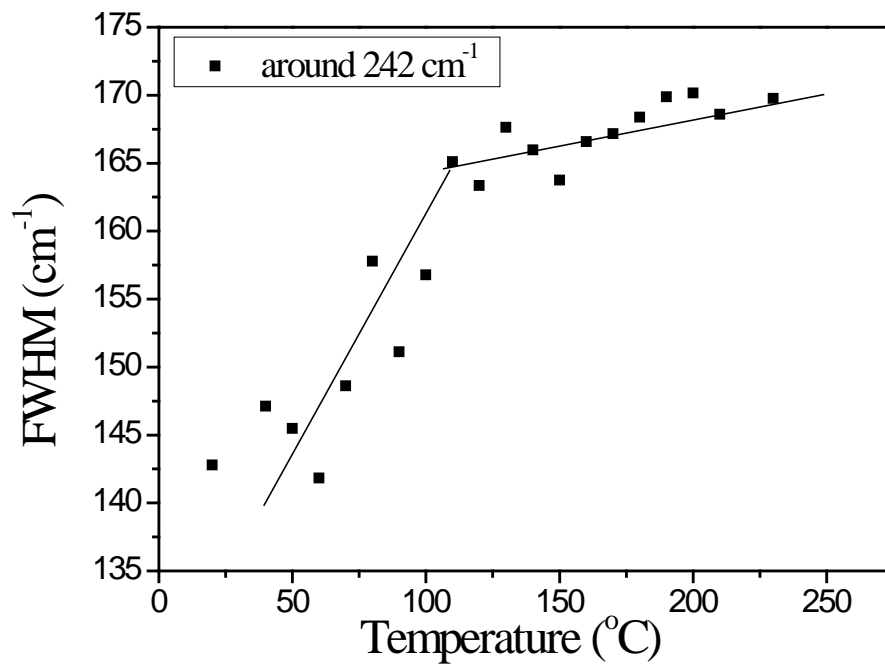
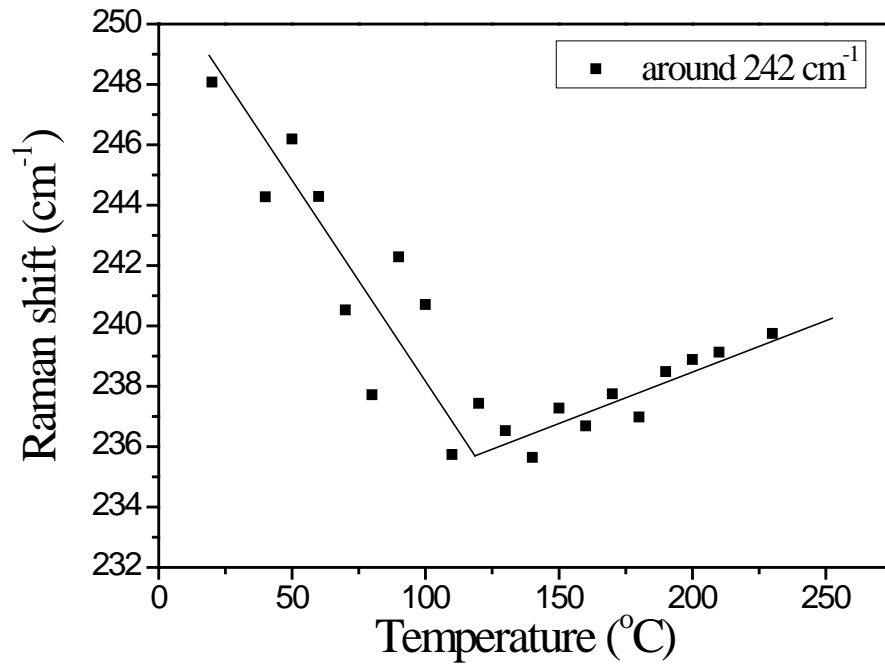


Fig. 4.8 Temperature dependence of the (a) Raman shift and (b) full width at half maximum (FWHM) of the main mode (at around 242 cm⁻¹) for the SBN film.

4.2.3 Conclusion

The temperature dependence of Raman spectra of SBN60 films across the ferro-paraelectric phase transition was discussed. The Raman bands at 240 and 625 cm^{-1} are broader than that of SCNN due to the relative disorder structure compared to SCNN. The temperature dependence of the Raman shift and FWHM of the Raman bands presents clear anomalies at the phase transition. The Raman bands at 240 and 625 cm^{-1} survive in the paraelectric phase but the slopes of the change of Raman shift are different after phase transition. It is because that some Nb^{5+} at B1 sites disappear gradually, but Nb^{5+} ions in B2 sites are still Raman active after Curie temperature.

4.3 Central peaks, acoustic modes, and the dynamics of polar nanoregions in of high oriented SCNN thin films on Si substrate by Brillouin scattering.

4.3.1 Introduction

$\text{Sr}_{2-x}\text{Ca}_x\text{NaNb}_5\text{O}_{15}$, with $0.05 \leq x \leq 0.35$, is of interest with regard to both fundamental research on uniaxial relaxor TTB structure ferroelectrics and applications, due to its prominent pyroelectric, electro-optic, and piezoelectric properties [Liu, 2006; Xie, 2002]. The TTB type structure can be regarded as consisting of a framework of sharing corner oxygen octahedra, forming three, four, and five membered rings in such a way that three types (C, A1, and A2) of interstitials result, which may receive different metal atoms, and the oxygen atoms of each octahedron surround an atom which is frequently Nb, Ta, or W located at B (B1, B2) sites. This structure is unstable, and most of the tetragonal and orthorhombic Tb type crystals undergo a paraelectric-ferroelectric transition versus temperature. Different cation substitutions in the A1, A2 sites as well as replacements of the Nb atoms in the B sites, which are consistent with the size and charge requirements of the lattice, can induce modifications of the crystal

phases and the critical transition temperatures with corresponding variations in physical properties. In SCNN, the A1 site is occupied by the smaller Ca^{2+} and Na^+ , and the A2 site is occupied by Sr^{2+} , all six A sites are occupied by metal ions, while the C site is empty. Thus, compared to partly occupied SBN, where 5 ions distribute in 6 A sites, SCNN has a fully occupied structure. The introduction of Na into the vacant A sites decreases the disorder of the structure. Meanwhile, the appropriate substitution of Sr^{2+} ions (1.44 Å) by smaller Ca^{2+} ions (1.34 Å) in SCNN enhances the structural distortion, and results in an increase in spontaneous polarization and related properties. Thus, SCNN presents many interesting physical phenomena owing to the competition of the order and disorder structure. Due to the uniaxial tunnel structures existing along the c axis, the difference between the ionic radii of Ca^{2+} and Sr^{2+} and built-in disorders, both local random fields and polarizations are expected to exist along the c axis.

TTB structure ferroelectric material is one of the most important ferroelectric relaxors. Relaxor ferroelectrics have been one of the most technologically important materials due to their huge piezoelectric, dielectric constants and pyroelectric properties. Relaxors are highly disordered materials showing a diffusive dielectric response with a broad maximum in the permittivity

curves at Curie temperature, the absence of long-range order and existence of local polarization far above the freezing temperature. In order to investigate the origins of the appearance of these properties, many experiments have been performed so far. The dynamics of polar nanoregions (PNRs) are thought to play an essential role in the physical properties of relaxor materials. Investigating the PNR dynamics of disordered ferroelectric systems poses challenging problems that have been studied during the past several decades, and many attempts have been made to understand the involved mechanisms. Despite this effort, the nature of these dynamics remains largely unexplained. Many attempts to explain the PNR dynamics in perovskite structure single crystals such as $\text{Pb}(\text{Ni}_{1/3}\text{Nb}_{2/3})\text{O}_3$, $\text{Pb}(\text{Mg}_{1/3}\text{Nb}_{2/3})\text{O}_3\text{-PbTiO}_3$ and $\text{Pb}(\text{Zn}_{1/3}\text{Nb}_{2/3})\text{O}_3\text{-PbTiO}_3$ using Brillouin light scattering (BLS) and Raman technique have been reported [Ye, 1998; Bokov, 2006; Tsukada, 2006]. Limited researches about the BLS study of TTB structure ferroelectric materials were reported. Jiang *et.al.* investigated the diffuse phase transition behavior of uniaxial relaxor single crystals of TTB structure $\text{Sr}_{0.61}\text{Ba}_{0.39}\text{Nb}_2\text{O}_6$ [Jiang 2002]. Surprisingly, though SCNN shows excellent piezoelectric, pyroelectric and electro-optic properties, up to now, there are no reports about the relaxor behavior investigation of SCNN thin films using the BLS technique. In this thesis, the purpose of the present section is to investigate

the dynamics of PNRs by BLS experiment. In order to obtain more insight into the uniaxial relaxor behavior observed in SCNN, detailed Brillouin spectra were obtained as functions of temperature and possible origins of Central Peaks (CP) were discussed. Diffuse phase transition behavior is illustrated by the use of the frequency shifts and their linewidths in the Brillouin spectra for different scattering geometries.

4.3.2 Experiment details

Highly oriented SCNN thin film on Si(100) substrate was fabricated by PLD as introduced in Chapter 2. Brillouin Light Scattering (BLS) with temperature controller was used to investigate their diffuse phase transition behavior. This BLS technique generally refers to the interaction of photons with phonons, magnons, or other low frequency quasiparticles. The intensity of the frequency shifted scattered light is very small (of the order of 10^{-10} of the incident laser intensity) compared to the original incident laser beam. Separation of the very weak scattered signal from the strong un-shifted original beam is achieved by the use of two pairs of Fabry-Perot etalons arranged in tandem.

The experimental setup is schematically shown in Fig. 4.9. A 70mW frequency stabilized ($\lambda_0 = 514.5\text{nm}$) argon-ion laser beam was focused on the glass sample. The sample was placed inside a Linkam high temperature cell (model TMS94) that was able to reach a maximum temperature of $1500\text{ }^\circ\text{C}$ measured within $\pm 0.1\text{ }^\circ\text{C}$. The backscattered light from the specimen is collected by the same objective lens and entered the Fabry-Perot interferometers after passing through various optical components for eventual detection by an avalanche photodiode. The spectrum was then recorded by the BLS software Ghost and analyzed with

Origin.

Fig. 4.10 is a photograph of the Linkam high temperature cell. The sample stage (b) was placed on a titled holder whose angle relative to the horizontal could be adjusted from 0° to about 75° . The control unit (a) could be programmed to set heating rates and temperature maintenance times. For our SCNN samples, we used a heating rate of $10^\circ\text{C}/\text{min}$ and wait for 5 min after reaching the desired temperature in order to assure that the whole sample was stable at that temperature. BLS measurement was executed and the temperature was then adjusted to the next value. The sample sat inside the heating chamber which was covered with a glass window in the center. During the BLS measurement, the laser beam propagates through the window and was focused on the sample.

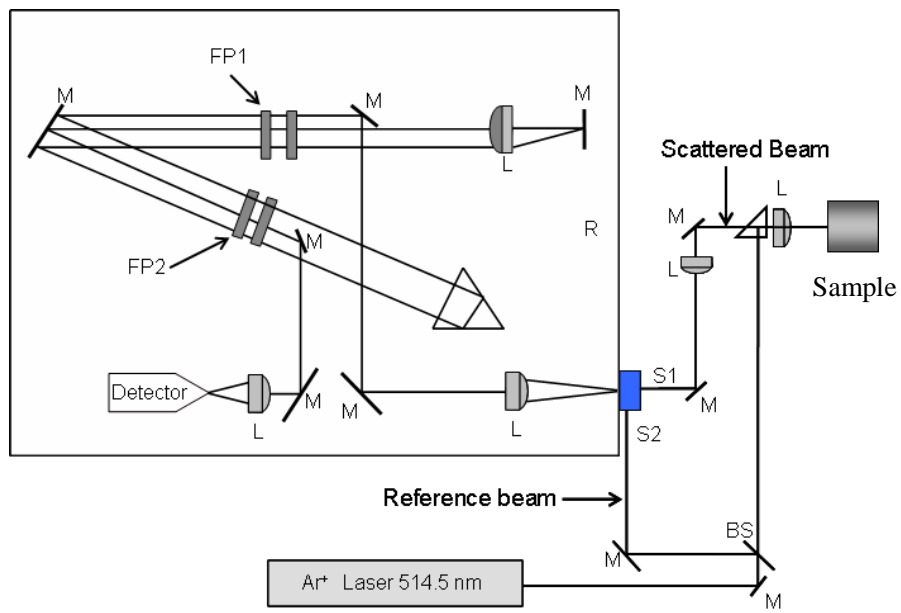


Fig. 4.9 Schematic of the experimental Brillouin scattering set-up in backscattering geometry. FP1 and FP2 represent the Fabry-Perot etalons; M, L and S identify various mirrors, lenses and slits, respectively. BS is a beam splitter and R a corner cube.

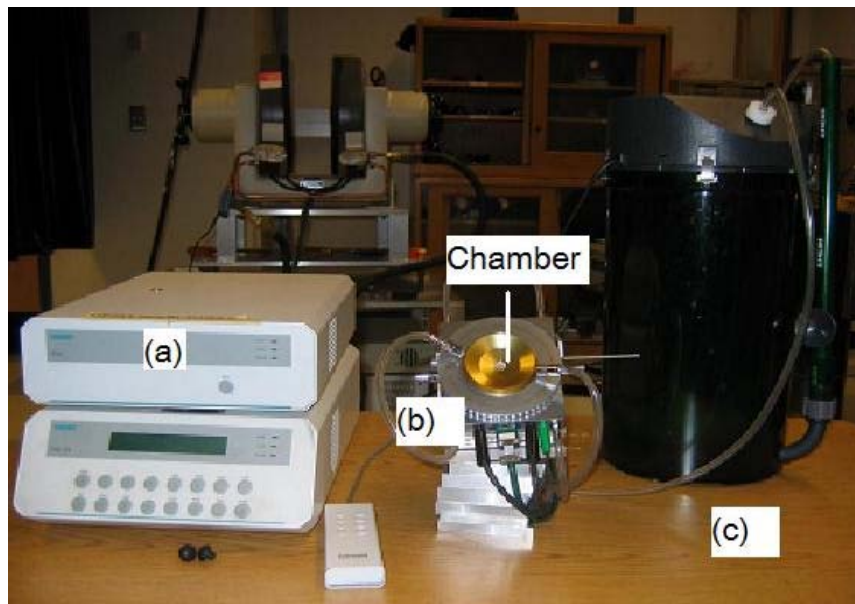


Fig. 4.10 Linkam high temperature cell (model TMS94). (a). Control Unit; (b). Sample Stage; (c). Water Tank & Pump.

4.3.3 Results and discussion

Figure 4.11. shows typical Brillouin spectra at different temperatures from 25 to 450 °C consisting of one longitudinal acoustic (LA) mode, one transverse-acoustic (TA) mode, and a central peak (CP). Data for each spectrum were accumulated for approximately half an hour in order to make the weak TA and LA mode to be observed. The two peaks and the central peaks were fitted using a Lorentzian profile to obtain the frequency shifts and the FWHM. Frequency shifts and FWHM in the Brillouin spectra are very sensitive to phase transitions, and the frequency shifts are related to elastic constants for certain acoustic modes. The frequency shift and FWHM of the TA and LA modes are plotted in Fig. 4.12-Fig. 4.15, respectively, as a function of temperature. It is seen that for the Brillouin shifts of both LA and TA mode frequency shifts change continuously with temperature. Both LA and TA modes show slightly softening with temperature at first, then a broad and marked increase in the LA shifts as well as TA shifts is found near 290 °C on further heating. This rising is accompanied by an increase in the FWHM with maxima at around 280 °C of the TA mode. These results are in agreement with temperature variation of the dielectric constant, which has a peak around 280 °C and is diffusive in nature [Liu, 2008; Xie, 2002]. Both the TA and LA modes show almost the same

temperature dependence with bending anomalies around Curie temperature (290 °C). This result indicates that both modes couple with the fluctuation of PNRs in the same way and the anomalies are caused by the slowing down of the motion of the PNRs.

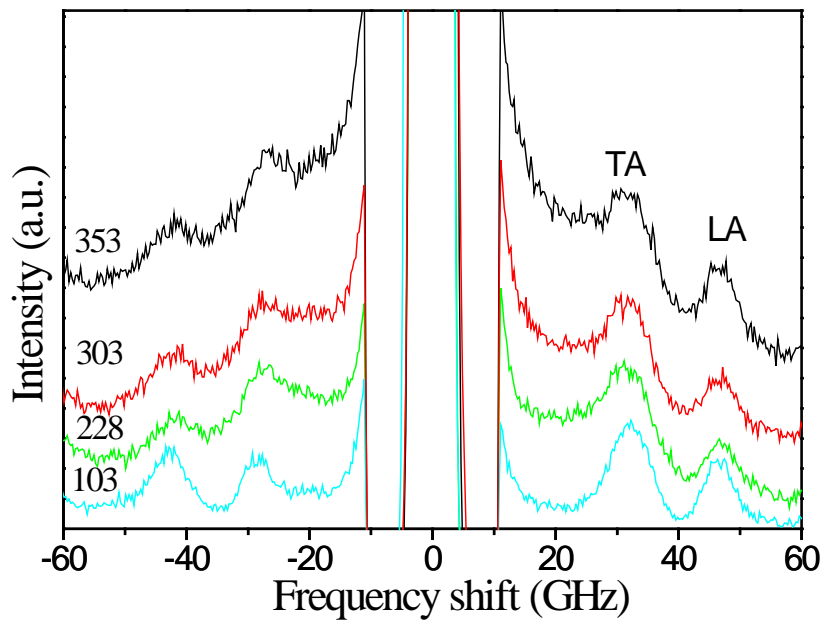


Fig. 4.11 Brillouin spectra at various temperatures observed in heating process.

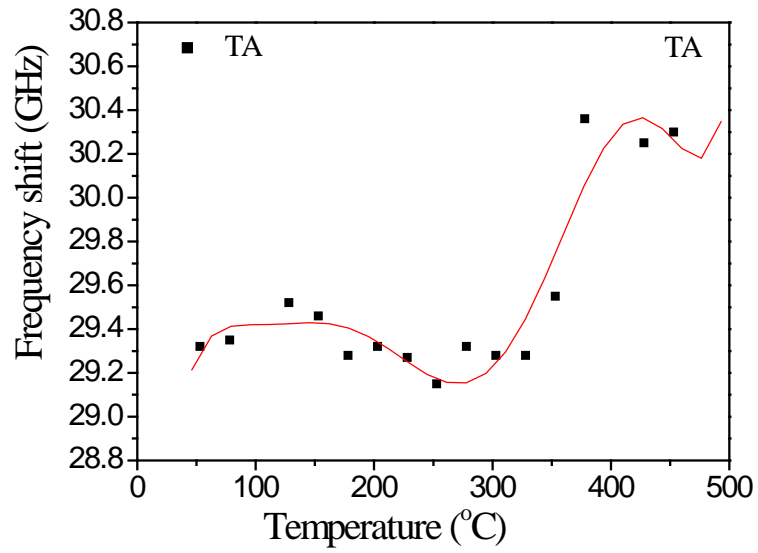


Fig. 4.12 Temperature dependence of the frequency shift of TA mode

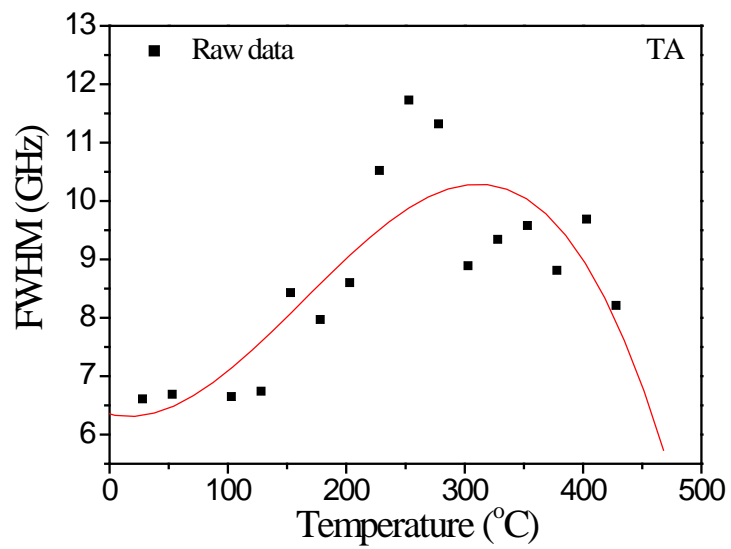


Fig. 4.13 Temperature dependence of the FWHM of TA mode

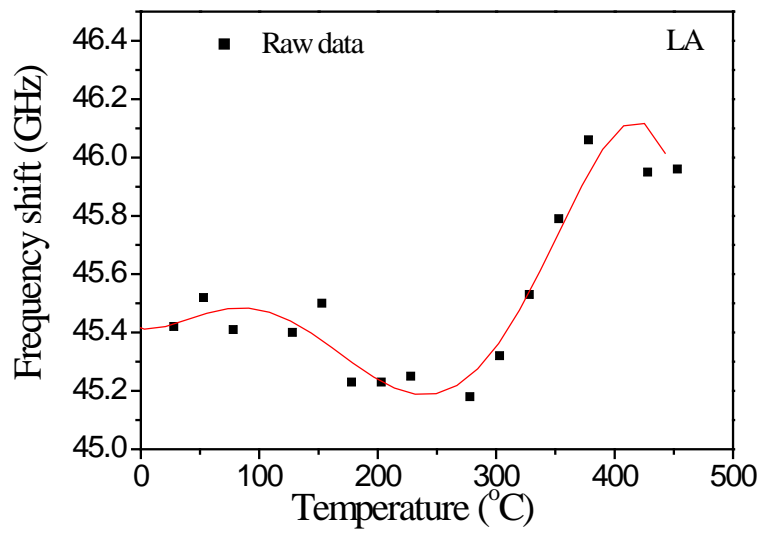


Fig. 4.14 Temperature dependence of the frequency shift of LA mode

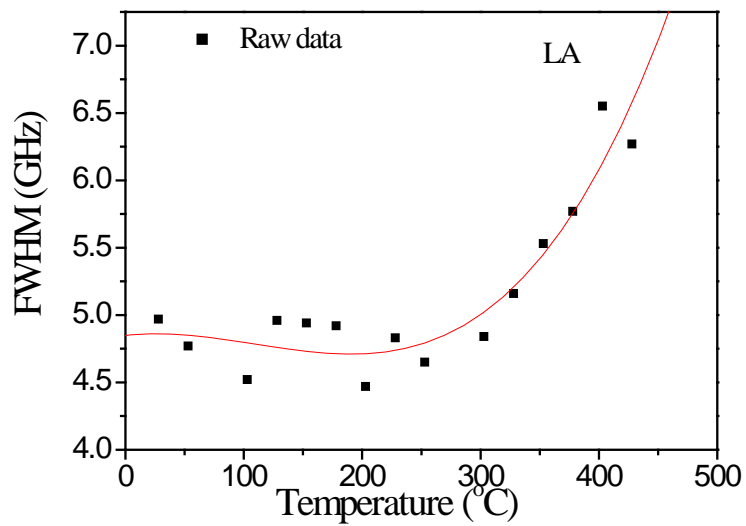


Fig. 4.15 Temperature dependence of the FWHM of LA mode

Note that one can determine the elastic constant C_{11} and C_{44} from the velocities of the LA and TA phonons studied in the c direction. The general relationship between the speed of sound (v), the density (ρ) of the specimen, and elastic constants C_{ij} is given by:

$$v = \sqrt{\frac{C_{ij}}{\rho}} \quad (4.1)$$

where i and j characterize the directions associated with the specific stress-strain components under consideration. The longitudinal (C_{11}) and transverse (C_{44}) elastic constants at a given temperature T are given by the following equations [Jiang, 2002]:

$$C_{11}(T) = \left[\frac{\rho(T) \lambda_0^2 v_{LA}^2}{4n(T)^2} \right] \quad (4.2)$$

$$C_{44}(T) = \left[\frac{\rho(T) \lambda_0^2 v_{TA}^2}{4n(T)^2} \right] \quad (4.3)$$

where v_{LA} and v_{TA} are the frequencies of the longitudinal and transverse acoustic

phonons at the fixed temperature, respectively. $\rho(T)$ and $n(T)$ are the density and refractive index at given temperature T , respectively. λ_0 is the laser wavelength. The calculated longitudinal and transverse elastic constants can then be used to determine the Young's modulus (E) of glass at the desired temperature using the relation:

$$E = \frac{C_{44}(3C_{11} - 4C_{44})}{(C_{11} - C_{44})} \quad (4.4)$$

In some reports dealing with the calculation of elastic constants using BLS results, only the values of the density and refractive index at room temperature were used. Thus, a significant error is induced due to the lack of temperature-dependent data. Thanks to the thermo prism coupler techniques, we measured the temperature dependence of the refractive index and thickness at different temperatures, as shown in Fig 4.16. Thickness of the film keeps nearly constant over the entire temperature range and the density of SCNN in room temperature is 5.01 g/cm^3 [Xie, 2002]. Thus, using equations 4.2-4.4 and the measured TA and LA frequency and refractive index data, we can calculate the temperature dependence of the elastic constant and Young's modulus, as shown in Figs 4.17-18. The temperature variation of all the elastic moduli is similar, but

not same, to their respective Brillouin shift. In the heating process, both LA and TA modes show obvious softening with temperature at first, and then a marked rise in the LA shifts and TA shifts is found above 280 °C on further heating.

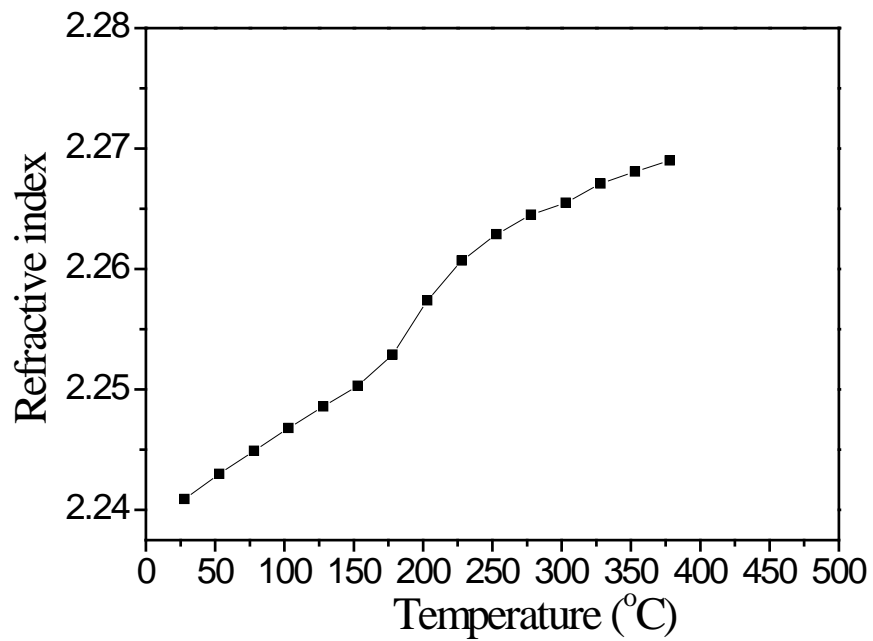


Fig. 4.16 Temperature dependence of refractive index.

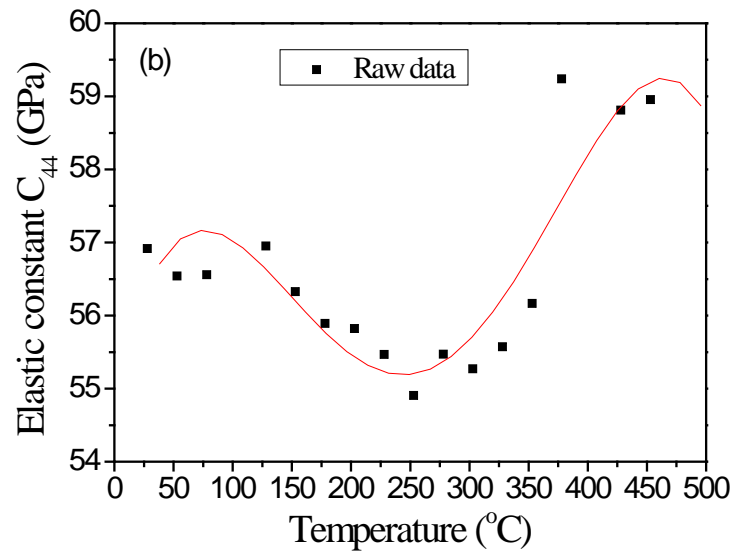
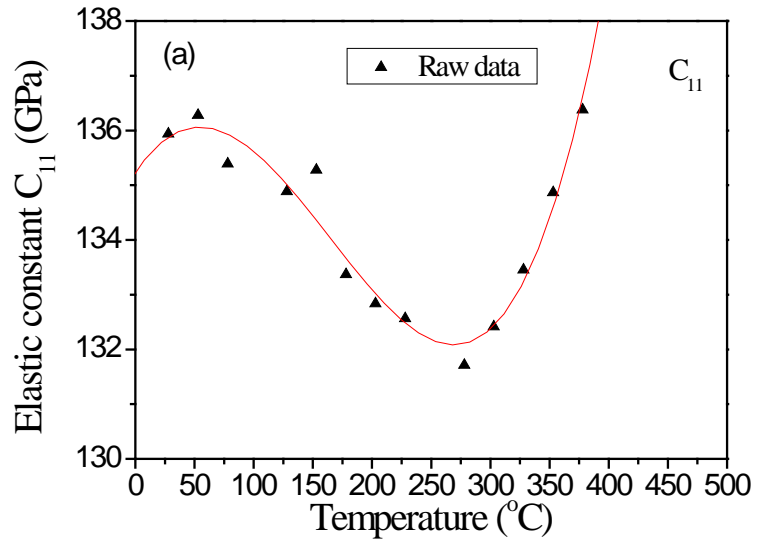


Fig. 4.17 Temperature dependences of elastic constants: (a) C_{11} and (b) C_{44} determined using Brillouin scattering.

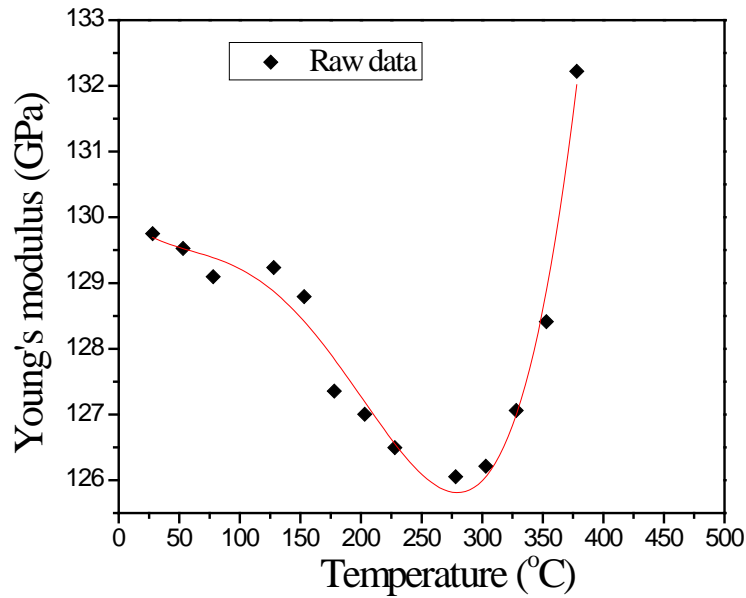


Fig. 4.18 Temperature dependences of Young's modulus.

The temperature dependences of Brillouin shift and elastic moduli can be interpreted qualitatively by the concept of freezing of the relaxation time dynamics. The diffuse phase transition in relaxors is characterized by the existence of PNRs at temperatures higher than the temperature at dielectric maximum (T_m). The growth of PNRs and the coupling between them seem to control the relaxor properties. In order to further understand the elastic change with the temperature, the free energy expression in terms of the order parameter should be considered. Generally, the Landau expression for the free energy F of

ferroelectrics can be consisted of three parts: the free energy associated with the order parameter, i.e., the polarization P , the free energy associated with the elastic energy, and finally the coupling term between the order parameter and the strain x . The details were given by Shabbir et.al. [Shabbir, 2003]. The change in elastic constant in terms of the local polarization P as an order parameter can be approximated as [Shabbir, 2003]

$$\Delta C = C - C^\infty = -g^2 \langle P^2 \rangle \chi \quad (4.5)$$

where g is the electrostrictive constant, $\langle P^2 \rangle$ is the mean value of the squared local polarization of PNRs and χ is the susceptibility. In ferroelectric relaxors this intrinsic local distortion constitutes the so-called polar nanoregions (PNRs) which exist below a certain temperature. This temperature, which is called Burns temperature (T_B), is typically a few hundred degrees higher than T_m . In the temperature range of $T_m \leq T \leq T_B$ in the heating process, the PNRs size becomes smaller and smaller with the increase of temperature. Due to the quadratic nature of this coupling, the decrease of local polarizations size results in rising of the elastic constants. For $T < T_m$, the Brillouin shifts of the two modes have negative temperature coefficients, which is most probably associated

with a lattice anharmonicity in the ordered phase. The maximum softening in the Brillouin shift and elastic constant occur near $T \approx T_m$. Meanwhile, due to strong thermodynamical fluctuations in the order parameter, caused by the complex dynamics of PNRs, the anomaly expected in the elastic constant might be spread over a wide temperature range.

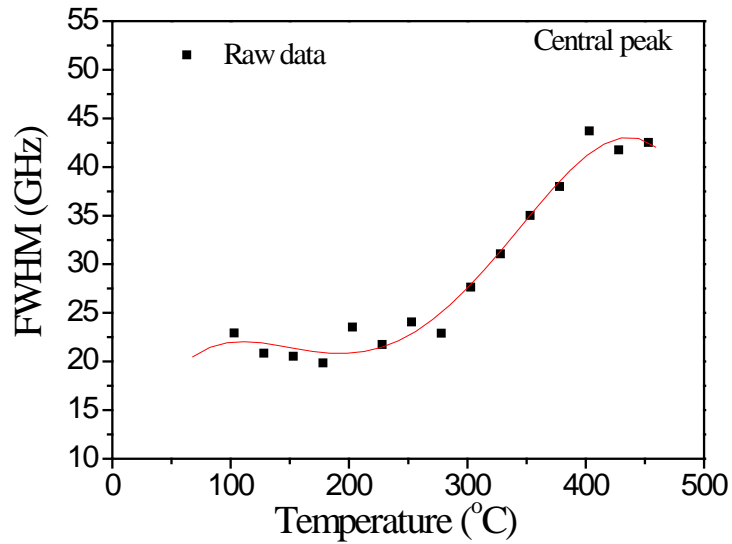


Fig. 4.19 Temperature dependence of the FWHM of central peak.

Central peak (CP) was fitted by a single Lorentzian centered at zero. Figure 4.19 shows the temperature dependence of the FWHM of CPs of SCNN. Although the origins of CPs have varied sources, CPs observed in ferroelectrics can arise from soft transverse-optic (TO) phonon, or from some relaxational entities, or from the coupling between them. However, the most probable origin of CPs in ferroelectric relaxors is the relaxational dynamics of PNRs. The temperature dependence of FWHM of CPs shows similar trend with that of frequency shift of LA and TA modes and the same mechanism can be used to explain it. In order to further understand the transition in SCNN relaxor, Debye relaxation $\exp(-t/\tau)$ is assumed to describe the dynamics of the CP. The relaxation time τ can be obtained by the equation [Gorouya, 2003]:

$$\tau = 1/2\pi\Gamma \quad (4.6)$$

where Γ is the full width at half maximum (FWHM) of CP. Fig. 4.20 (a) shows the temperature dependence of the relaxation time. The temperature dependence of relaxation time is similar to that of the dielectric constant, and has a broad peak at around T_m . At the temperature below T_m , τ increases with increasing

temperature, because the spontaneous polarization disappears gradually due to the ferroelectric phase transition and the fluctuations of PNRs becomes more active. Above T_m , however, the relaxation time becomes shorter with increasing temperature, because each PNR becomes smaller in size, thus, it takes smaller time to relax. Sokoloff *et.al.* used a semiclassical model to describe the temperature dependence of τ above T_m [Sokoloff, 1988; 1990]. In this semiclassical tunneling model, a B site ion of ABO_3 perovskite structure moves in a double-minima potential well with the barrier of energy height ΔV . An ionic carrier attempts to approach the barrier with the characteristic time τ_0 and tunnels the barrier with the probability $\exp(\Delta V - k_B T) / k_B T_0$ to cause the reorientation of electric dipole. Here, k_B is a Boltzmann's constant and T_0 is the temperature which is related to the mass of the B site ion and the curvature of the barrier. Thus, the reorientation time τ is expressed as $\tau = \tau_0 \exp(\Delta V - k_B T) / k_B T_0$. Although the relaxation mode is described quite well by the semiclassical tunneling model, Jiang and Kojima pointed out that the semiclassical tunneling model contains the physically unreliable assumption for the relaxor, that is, the potential barrier is invariant with temperature. So a modified superparaelectric model (Arrhenius-type relaxation model) with a temperature dependent activation energy was used to determine the potential

barriers [Gorouya, 2003]:

$$\tau = \frac{1}{2\nu_D} \exp(H/k_B T) \quad (4.7)$$

$$H = \begin{cases} 0 & (T \geq T_B) \\ H_0(T_B - T)/T_B & (T_m \leq T \leq T_B) \end{cases} \quad (4.8)$$

Here, H_0 is the activation energy extrapolated to 0 K, T_B is the temperature at which PNRs begin to appear (cooling process), ν_D is the Debye cutoff frequency. Then, in order to get the parameters of T_B and H_0 easily, we changed the form of the formula of the modified superparaelectric model:

$$\ln \tau = -\ln(2\nu_D) - H_0/k_B T_B + H_0/k_B T \quad (4.9)$$

The relaxation time plotted in the form of $\ln \tau$ vs $1000/T$ was fitted with the modified superparaelectric model, as shown in Fig. 4.20 (b), and it should follow a straight line above T_m . To estimate ν_D [Jiang, 2000], we use the formula $\nu_D = (6\pi^2 N/V)^{1/3} v_0 2\pi$, where $3/v_0^3 = 1/v_L^3 + 2/v_T^3$. Here, v_L , v_T , N and V are longitudinal and transverse acoustic mode velocity, the number of vibration modes, and the unit cell volume, respectively. The velocities

$v_L = 23.4 \text{ km/s}$ and $v_T = 15.2 \text{ km/s}$ are easily determined from the frequency shifts of the LA and TA modes, respectively. Using the above data and the N/V data in the literature [Burns, 1969], the Debye cutoff frequency ν_D was determined to be 6.36 THz. At last, by linear fitting above T_m (Fig. 4. 20) and using formula (4.9) and obtained parameters, the values of H_0 and T_B were determined to be 1430 K and 805 K, respectively. Though there are no related data of SCNN in literature that can be used to compare with our obtained results. These obtained values are reasonable and are of almost the same order of magnitude as those determined by Brillouin scattering in other relaxor and relaxor-based ferroelectrics (T_B 2300 K and H_0 1900 K in $0.8\text{Pb}(\text{Zn}_{1/3}\text{Nb}_{2/3})\text{O}_3$ -0.2 PbTiO_3 , T_B 852 K and H_0 6136 K in $0.65\text{Pb}(\text{Mg}_{1/3}\text{Nb}_{2/3})\text{O}_3$ -0.35 PbTiO_3 and T_B 670 K and H_0 1309 K in $\text{Pb}(\text{Ni}_{1/3}\text{Nb}_{2/3})\text{O}_3$) [Gorouya, 2003; Jiang, 2000; Kuok, 2001].

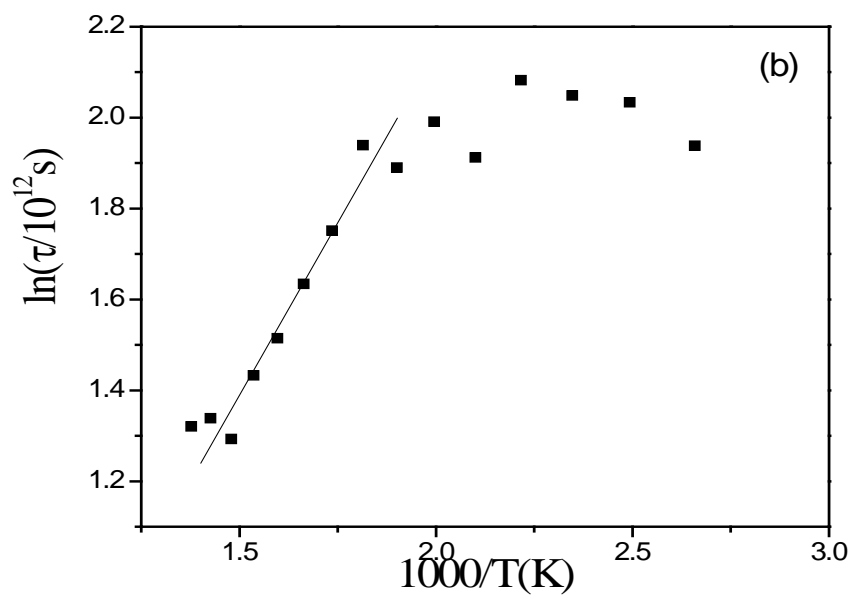
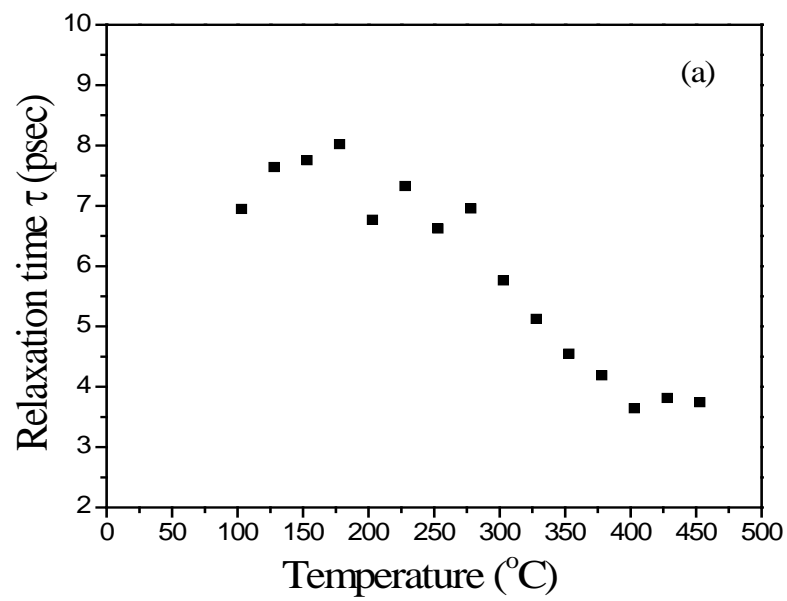


Fig. 4.20 Temperature dependence of the relaxation time.

4.3.4 Conclusion

In summary, we reported, for the first time, the Brillouin scattering study in detail of highly *c*-oriented SCNN films on Si (100) substrate over a wide temperature range. The Brillouin frequency shift with increasing temperature shows an anomaly for both LA and TA phonon modes. A gradual growth in damping (FWHM) with maximum near 280 °C is observed, at which the low-frequency permittivity has a maximum value. This result indicates that both modes couple with the fluctuation of PNRs in the same way and the anomalies are caused by the slowing up of the motion of the PNRs. The elastic stiffness C_{11} and C_{44} are also determined between 25 and 450 °C. In addition to the acoustic modes, a relaxational mode is found in the form of a central peak. The relaxation time τ of the mode has a temperature dependence similar to that of dielectric constant and shows a broad peak anomaly around T_m . By the analysis of modified superparaelectric model, the activation energies of relaxation processes H_0 and Burns temperature T_B are determined to be the 1430 K and 805 K, respectively.

5 Magneto-electric and dielectric relaxor properties of the $\text{Sr}_{1.9}\text{Ca}_{0.1}\text{NaNb}_5\text{O}_{15}$ - CoFe_2O_4 composite

In the past decades, there has been a continually increasing interest in magnetoelectric (ME) materials due to their attractive physical properties and potential applications in actuators, transducers, field sensors, and data storage devices [Busch, 1998; Hill, 2002; Zheng, 2004]. Such materials display a spontaneous dielectric polarization as a response to an applied magnetic field, or an induced magnetization driven by an external electric field. The prerequisite for the observation of the ME effect is the coexistence of magnetic and electric dipoles. Based on this primary requirement, ME effect could be realized in composites consisting both ferroelectric and ferro/ferrimagnetic phases, as first proposed by Van Suchetelene [Suchetelene, 1972].

5.1 Introduction

When designing these composites, the following issues should be considered: (a) a high Curie point for the ferroelectric phase, (b) a high Néel/Curie temperature for the ferri/ferromagnetic phase, and (c) large piezoelectric as well as magnetostrictive coefficients.

In the present study, a new ceramic system based on tetragonal-tungsten-bronze (TTB) ferroelectric relaxor $\text{Sr}_{1.9}\text{Ca}_{0.1}\text{NaNb}_5\text{O}_{15}$ (SCNN) and Co-ferrite CoFe_2O_4 (CFO) as the ferroelectric and ferrimagnetic components, respectively, was fabricated. To our knowledge, no similar ME composite systems have been reported. This selected composite system is attractive due to (i) the large spontaneous strain associated with the ferroelectric phase transition in SCNN as well as the strong elastic interaction between the two phases, (ii) the large magnetostriction of the ferrimagnetic CFO phase, (iii) the high Curie temperature of SCNN (250-300 °C) due to the introduction of Na ions in the void sites and the high Néel temperature of CFO (520 °C), and (iv) its lead-free and environmental friendly components. In this paper, we demonstrate that this composite exhibits relaxor properties, room temperature ferroelectric and ferrimagnetic hysteresis loops and desirable magnetoelectric coupling.

5.2 Experimental details

The SCNN-CFO composites were prepared via a conventional solid state reaction method. SrCO_3 , CaCO_3 , Na_2CO_3 and Nb_2O_5 powders were ball milled and then calcined at 1250 °C in air for 6 hours to prepare $\text{Sr}_{1.9}\text{Ca}_{0.1}\text{NaNb}_5\text{O}_{15}$ powder. On the other hand, mixture of $\text{Co}(\text{CH}_3\text{COO})_2$ and Fe_2O_3 powders was calcined at 1200 °C in air for 6 hours to create CoFe_2O_4 powder. Finally, mixture of SCNN and CFO powders, in molecular ratio of 6:4, was ball milled and pressed into discs. The composite ceramics were then obtained by sintering these discs at 1200 °C in air for 6 hours.

The ME effect of the composites was characterized using an home built automated measurement system. Prior to the ME measurement, the samples were poled electrically under 30 kV/cm in silicon oil while the samples were cooling from 260 °C and poled magnetically under 2.5 kOe for 30 min at room temperature. Since this selected poling magnetic field is larger than the coercive field of CFO (220 Oe), we believe that the composites was magnetically poled.

5.3 Results and discussion

Figure 5.1(a) shows a typical XRD pattern of the SCNN-CFO composites. Two distinct sets of diffraction peaks, corresponding either to the TTB phase of SCNN or the cubic spinel CFO phase, are observed. No extra peaks corresponding to other phases are identified. Furthermore, SEM image shown in figure 1(b) displays the microstructure of the composites. Dense, crack-free composite with no observable pores is identified within areas etched below the polished surface. As observed in the SEM micrograph, two different types of grain are recognized. The EDX results suggest that grains corresponding to SCNN phase are rod-like shapes with an average width and length of 2-3 μm and 15 μm , respectively, while the relatively small spherical grains correspond to the uniformly distributed CFO phase. Hence, both the XRD and SEM results indicate that no observable chemical reaction or diffusion between the CFO and SCNN phases existed in these composites.

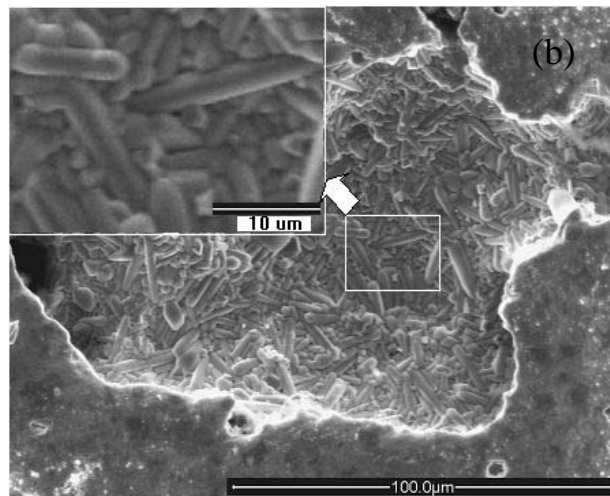
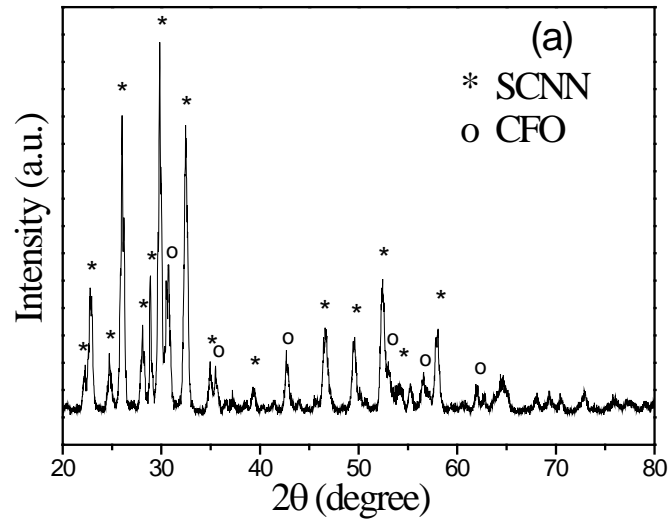


Fig. 5.1 (a) XRD patterns of the SCNN-CFO composite ceramic. (b) SEM micrographs of the polished and etched surface of composite ceramic. (The inset is an enlarged image of the labeled rectangular of the etched region)

Figure 5.2 shows the variation of the permittivity of the composite as a function of temperature measured at different frequencies. Higher permittivity is obtained at lower frequencies and all the permittivity curves are accompanied by an interesting temperature dependence. An increase in the permittivity is observed with increasing temperatures up to the transition temperature (270 °C) and then followed by a decrease in the permittivity as further increase of temperature. As shown in Fig. 5.2, the permittivity curves of our samples display a broad temperature dependence in the vicinity of the transition temperature. Compared to pure SCNN ceramics, the SCNN-CFO composites display a larger frequency dependence, i.e. the rate of change of permittivity with respect to frequency at a fixed temperature is larger in SCNN-CFO composites than that observed in pure SCNN ceramics [Xie, 2002]. The high permittivity measured at low frequencies might be attributed to the interface between ferroelectric and ferrimagnetic phases which have significantly different conductivities. These interfaces cause an additional polarization, the interfaces polarization, which boosts the permittivity [Tang, 2005]. As this interface polarization usually responses slowly to external field, it is inactive at high frequencies (about 10^5 to 10^6 Hz). Thus, it has no contribution to the permittivity at high frequencies, resulting in the decrease of the

permittivity. Furthermore, it is noticed that the high frequency curves have broader temperature dispersion as compared to the low frequency curves.

Apart from the remarkable dispersion behavior observed in the temperature dependence of the permittivity, a well-defined central peak is also observed in the Brillouin scattering spectrum of the composite (Figure 4.11). In addition to the observation of this central peak, the FWHM of this peak increases significantly around Curie temperature. These two features suggest that the composites belong to relaxor-type composites [Tsukada, 2006]. Details of the Brillouin scattering has been discussed in chapter 4.3.

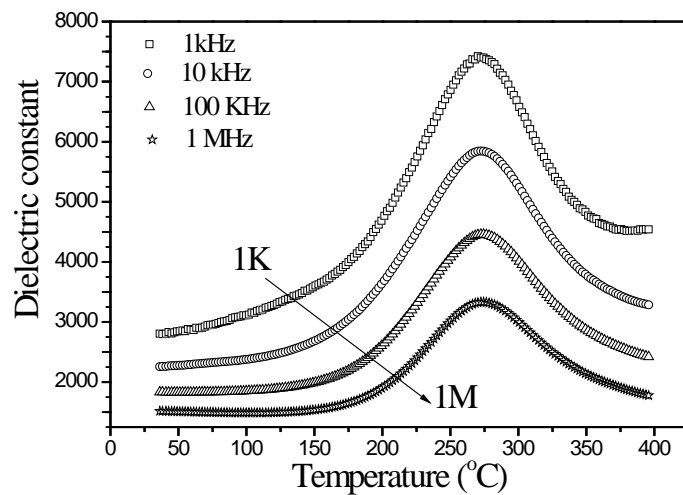


Fig. 5.2 Temperature dependence of the dielectric constant of the SCNN-CFO composite ceramic at various frequencies.

The phase transition feature of the composites was fitted using the modified

Curie–Weiss law [Kumar, 2007]:

$$\frac{1}{\varepsilon(f, T)} = \frac{1}{\varepsilon_m(f)} \left\{ 1 + \frac{[T - T_m(f)]^\gamma}{2\Delta^2} \right\} \quad (5.1)$$

This equation defines the diffuseness of the relaxor phase transition, where γ ($1 < \gamma < 2$) is a constant which expresses the diffuseness exponent of the phase transition, indicating if the phase transition being or not “completely” diffusive.

Δ is the peak broadening parameter that indicates the diffuseness degree, ε_m is the dielectric permittivity maxima and T_m is temperature at dielectric maxima.

When $\gamma = 1$, the material follows an ideal Curie–Weiss law which shows validity in case of normal ferroelectrics, whereas $\gamma = 2$ corresponds to a so-called “complete” diffuse phase transition [Uchino, 1982]. Figure 5.3 shows the plot of $\ln(\varepsilon_m / \varepsilon - 1)$ as a function of $\ln(T - T_m)$ at different frequencies. γ , obtained by fitting the experimental data with equation (5.1), are found to be 1.73, 1.82, 1.84 and 1.93 for frequencies of 1 kHz, 10 kHz, 100 kHz and 1 MHz, respectively.

These values are very close to 2, demonstrating the relaxor behavior of the SCNN-CFO composites.

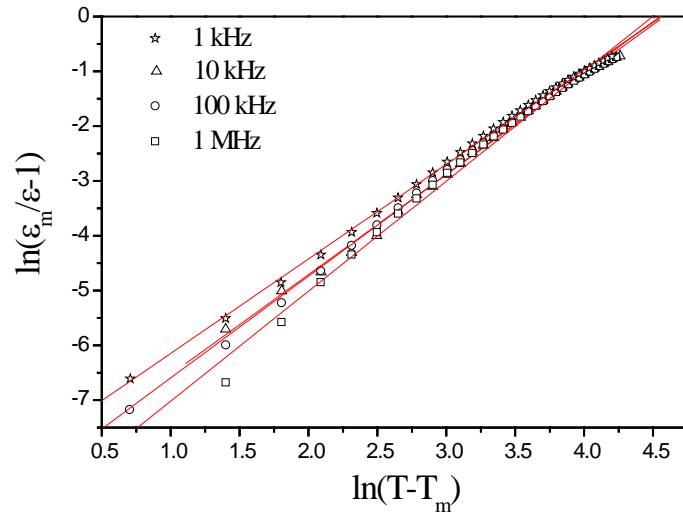
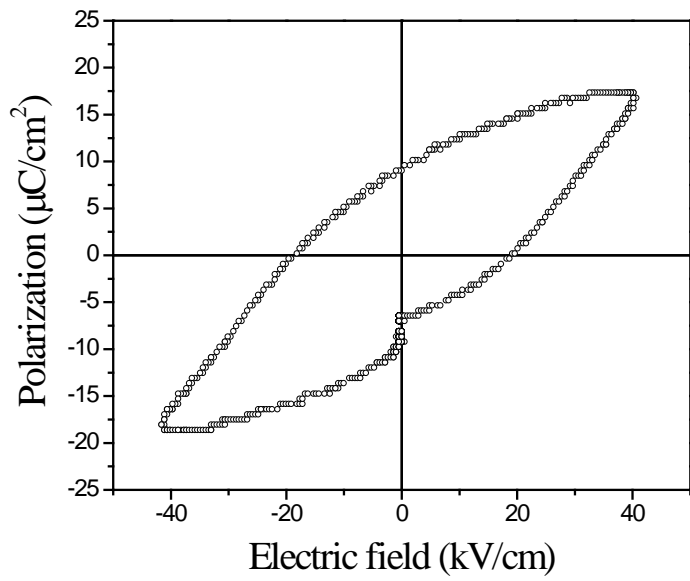


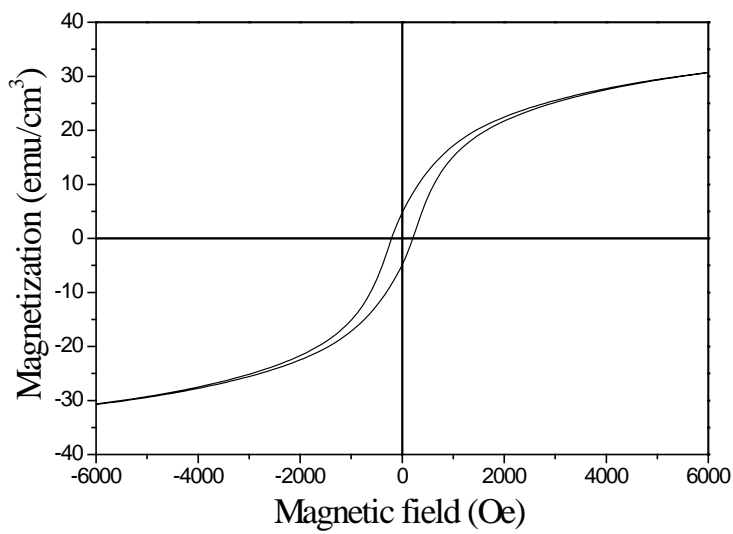
Fig. 5.3 Plot of $\ln(\varepsilon_m / \varepsilon - 1)$ as a function of $\ln(T - T_m)$ for the SCNN-CFO composite ceramics.

These composites also exhibit ferroelectric as well as ferrimagnetic hysteresis loops at room temperature. As shown in Fig. 5.4, SCNN-CFO composites show a well-defined ferroelectric loop with remnant polarization (P_r) and coercive fields (E_c) of about $9.5 \mu\text{C}/\text{cm}^2$ and $19.1 \text{ kV}/\text{cm}$, respectively, at an applied electric field of $30 \text{ kV}/\text{cm}$. The composites are highly resistive with no breakdown under an applied electric field upto $30 \text{ kV}/\text{cm}$. In addition to the P-E loop, a well-defined ferrimagnetic hysteresis loop is also displayed in Fig. 5.4. The saturation magnetization (M_s) of SCNN-CFO composites ($33 \text{ emu}/\text{cm}^3$ for

in-plane) is much smaller than that of pure CFO ceramics (350 emu/cm^3) due to the low volume concentration (22%) of the CFO in the composites. The magnitudes of the remnant magnetization (M_r) and coercive field (H_c) for SCNN-CFO composites are found to be 5.2 emu/cm^3 and 206 Oe, respectively. The H_c value for the present composites is much lower than that of the pure CFO bulk (2 kOe) [Manivannan, 2001]. This is probably because CFO magnetic domains can be switched easily in the non-magnetic environment inside SCNN matrix, due to its relaxor inherent property and the difference of thermal expansion coefficients between the SCNN and CFO phases [Wan, 2006]. This easy-magnetization characteristic facilitates magnetic domain rotation and results in a larger magnetostriction under very low magnetic fields, consequently leading to a strong ME coupling at the interface between the ferroelectric and ferrimagnetic phases. As expected, a significantly large thickness piezoelectric charge coefficient (d_{33}) of 105 pC/N was obtained using a quasistatic Berlincourt piezo meter.



(a)



(b)

Fig. 5.4 (a) Polarization-electric (PE) hysteresis loop and (b) ferromagnetic hysteresis (MH) loop of the SCNN-CFO composite ceramic.

The coexistence of the ferrimagnetic CFO and ferroelectric SCNN phases in

the present composites gives rise to a ME effect, which is characterized by their ME coupling coefficient $\alpha_E = dE/dH$. Figure 5.5 shows the frequency dependence of α_E at an applied ac magnetic field of 10 Oe. In our experiment, no DC bias magnetic fields were applied. From Fig. 5.5, it is noticed that α_E remains nearly constant in the frequency range of 100 Hz to 10 kHz, and then increases rapidly after 10 kHz. A maximum α_E value of 58 mV/cm·Oe was obtained under zero DC bias with an 88 kHz magnetic field of 10 Oe. These α_E values are comparable to those obtained in other ME systems such as BaTiO₃/CFO ($\alpha_E \approx 3\text{mV/cm.Oe}$), PZT/LSMO ($\alpha_E \approx 4\text{mV/cm.Oe}$) and Ni_{0.5}Cu_{0.5}Fe₂O₄/Ba_{0.5}Pb_{0.5}Ti_{0.5}Zr_{0.5}O₃ ($\alpha_E \approx 0.2\text{mV/cm.Oe}$) [Duong, 2007; Ma, 2007; Kanamadi, 2007]. No dramatic gain was observed due to two possible reasons: 1) the expected resonance frequency is higher than the highest frequency that our instrument can reach; and 2) there is no resonance in the samples that we studied. This was confirmed by the frequency dependence of the electric impedance where no dramatic gain was observed between 1-100 kHz (not shown). Such behavior is similar to that reported in ref [Jia, 2006; Tang, 2005; Dai, 2004].

The inset in Fig. 5.5 shows the dc bias magnetic field dependence of the ME coefficient. For two different ac frequencies of 5 kHz and 25 kHz, with an increase in DC bias magnetic field, α_E increases before reaching its maximum near the

coercive field then drops and remains nearly constant beyond 1 kOe. The observed trend is similar to that reported in Dai *et al.*'s work [Dai, 2004]. The present composites can work for frequencies up to and, probably, beyond 100 kHz without subjecting to redundant thermal-induced depolarization of the ferroelectric member due to its high Curie temperature. This permits promising applications in magnetic devices for these high Curie temperature composites.

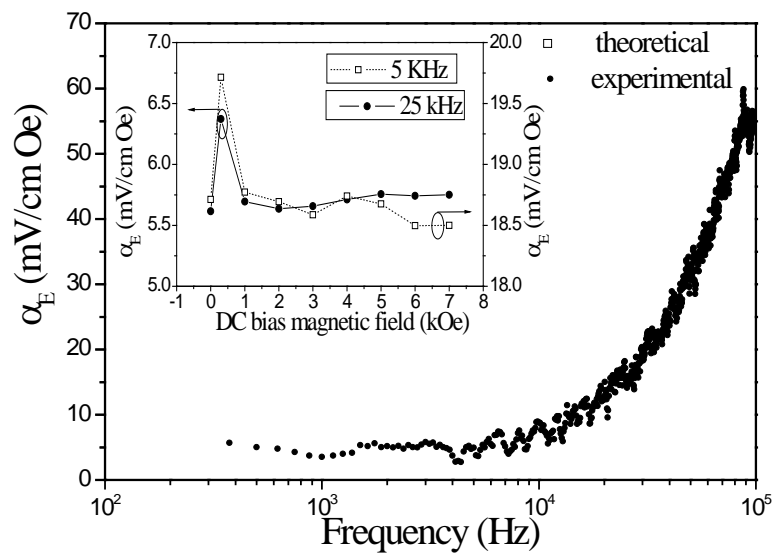


Fig. 5.5 Frequency dependence of experimental α_E at ac magnetic field of 10 Oe for the SCNN-CFO composite ceramic at room temperature. The inset shows the dc bias magnetic field dependence of α_E .

5.4 Conclusion

Lead-free high Curie temperature SCNN relaxor is chemically compatible with CFO ferrite. Their composites have been electrically and magnetically poled to exhibit a significant ME effect. A remarkable dielectric constant dispersion spectrum with Curie temperature of 270 °C was observed. A well-defined ferroelectric hysteresis loop with remnant polarization (P_r) and coercive fields (E_c) of about 9.5 $\mu\text{C}/\text{cm}^2$ and 19.1 kV/cm, respectively, and a ferrimagnetic hysteresis loop with remnant magnetization (M_r) and coercive field (H_c) of about 5.2 emu/cm^3 and 206 Oe, respectively, were obtained for the same composite ceramic. A maximum ME coupling coefficient α_E of 58 mV/cm·Oe was obtained under zero dc bias and an ac magnetic field of 10 Oe at 88 kHz. On the basis of our studies, it is suggested that the lead-free high Curie temperature SCNN-CFO relaxor composites are potential candidate for magnetoelectric devices.

6 Fabrication of SBN nanocrystals

6.1 Introduction

$\text{Sr}_x\text{Ba}_{1-x}\text{Nb}_2\text{O}_6$ (SBN, $0.25 < x < 0.75$) is an attractive ferroelectrics with tungsten bronze-type structure. It exhibits excellent electro-optic (EO), large pyroelectric and good ferroelectric properties, which make SBN a potential candidate for miniaturized EO modulators, infrared sensors and information storage devices [Tayebati, 1996; Marx, 1995; Trivedi, 1996]. A wide range of methods have been developed for the fabrication of SBN in various forms, such as RF-heating Czochralski method [Woike, 1997] and Stepanov technique [Volk, 2004] for the growth of pure and rare earth-ions doped SBN crystals, sol-gel method [Mak, 1998] and pulsed laser deposition [Tayebati, 1996] for the preparation of SBN films. For SBN powders, several fabrication methods have been reported. Traditional solid state reaction, which has been commonly used to prepare micron-size SBN powders, usually leads to poor compositional homogeneity. It also results in large grain size with a wide particle size distribution. In recent years, several wet chemical processes such as sol-gel method, Pechini method, and aqueous gel route have been used to synthesize

SBN powders [Pechini, 1967; Ho, 1999; Li, 2004]. All these methods need relatively high temperatures to form SBN of TTB phase. These high temperature processes often leads to compositional and structural inhomogeneities, large particle size, high impurity content due to repetitive calcination and grinding steps, and low chemical activity in the production. All of these problems impose drawbacks and thus hinder certain limitation on the researches as well as applications of these ferroelectric ceramics. Furthermore, these Ba, Sr and Nb organic source used in the above methods are sensitive to moisture in air. Thus, the synthesis process becomes complicated and has to be operated under dry nitrogen atmosphere. Additionally, these organic sources are relatively expensive and not cost-effective in commercial applications.

6.2 Fabrication of nanocrystals

A simple polymerizable complex route, known originally as the Pechini method, was selected to fabricate SBN nanocrystals at low processing temperature. It uses water-soluble precursors and is a highly flexible method for synthesis of oxide thin films as well as powders due to excellent homogeneity, precise stoichiometry, and processing simplicity [Pechini, 1967; Szanics,1999]. $\text{Sr}(\text{CH}_3\text{COO})_2 \cdot 1/2\text{H}_2\text{O}$, $\text{Ba}(\text{CH}_3\text{COO})_2$ powder and niobium oxalate solution were used as starting materials. The chelating agents were ethylenediaminetetraacetic acid (EDTA), citric acid and ethylene glycol. The water-soluble niobium oxalate solution was synthesized from niobium oxide and oxalic acid. It has been described elsewhere in detail [Li, 2004]. $\text{Sr}(\text{CH}_3\text{COO})_2 \cdot 1/2\text{H}_2\text{O}$, $\text{Ba}(\text{CH}_3\text{COO})_2$ and EDTA were dissolved in dilute ammonium hydroxide (NH_4OH) to form the Sr-EDTA and Ba-EDTA solutions. The mixed solutions were added in the niobium oxalate solution. A clear solution was obtained at a PH value of 7–8. Ethylene glycol was then added to the final solution. The molar ratio of metal cation : citric acid : ethylene glycol was fixed to 1: 4: 8. The precursor solution was heated at 130 °C for more than ten hours to form a glassy resin. After pyrolyzing at 450 °C for 2 h, gray powder precursor was produced. The final light yellow SBN nanocrystals were prepared by calcining the powder in air for 4 h at 750 °C.

6.3 Characterization

Figure 6.1 shows the XRD patterns of SBN50 nanocrystals prepared by the Pechini method, it presents a typical tungsten bronze tetragonal structure. Figure 6.2 shows the TEM and HRTEM images of the as-fabricated SBN nanocrystals. Using Pechini method, the fabricated SBN nanocrystals exhibit a nano-rod-like shape with a quasi-one-dimension of length up to 100 nm and a width within 20 nm. The lattice in elongated direction calculated from the HRTEM and electric diffraction images is 3.87nm, suggesting that the elongated direction coincided with the *c*-axis direction, its self-polarizing axis. The energy dispersive x-ray spectrum indicates that the as-prepared SBN powders are very pure (the signal of Cu is from the copper wire mesh used to keep the powder samples) with Sr:Ba:Nb equals to 0.49:0.51:2.07.

Figure 6.3 shows the unpolarized Raman spectrum in the vicinity of the optical phonon frequencies for as-synthesized SBN powders. It is clearly seen that the two strong $A_1(\text{TO})$ phonons modes of the SBN nanocrystals are located at 260 and 630 cm^{-1} . Indeed, this spectrum is very similar to the spectrum of SBN50 given by M. T. Ho *et al* [Ho,1999]. Since there are 132 optical phonon

modes in the unit cell, it is possible that several nearly degenerate modes may occur and appear as one band. This degeneracy would contribute to the broadening of the band and asymmetric line-shape. The spectrum of the SBN powders is identical to the TTB phase of SBN50 single crystal and SBN50 powders synthesized by sol-gel except that the phonon peaks are slightly broader.

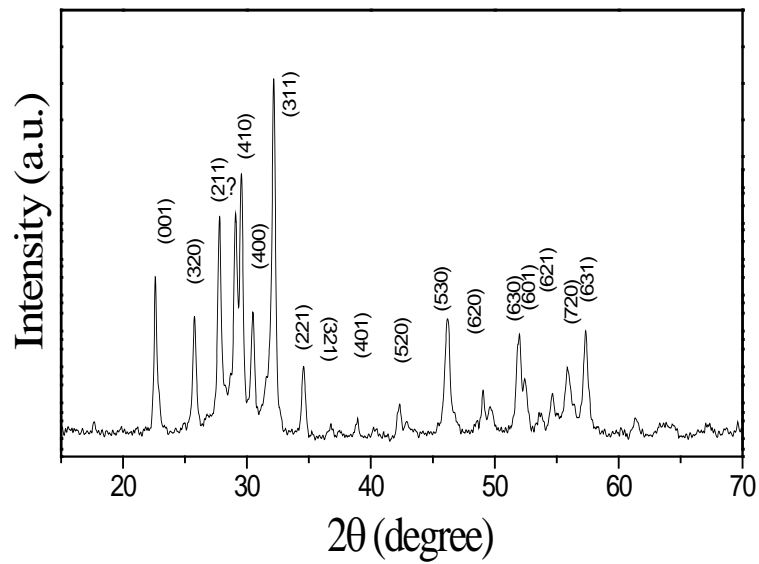


Fig. 6.1 XRD patterns of SBN nanocrystals.

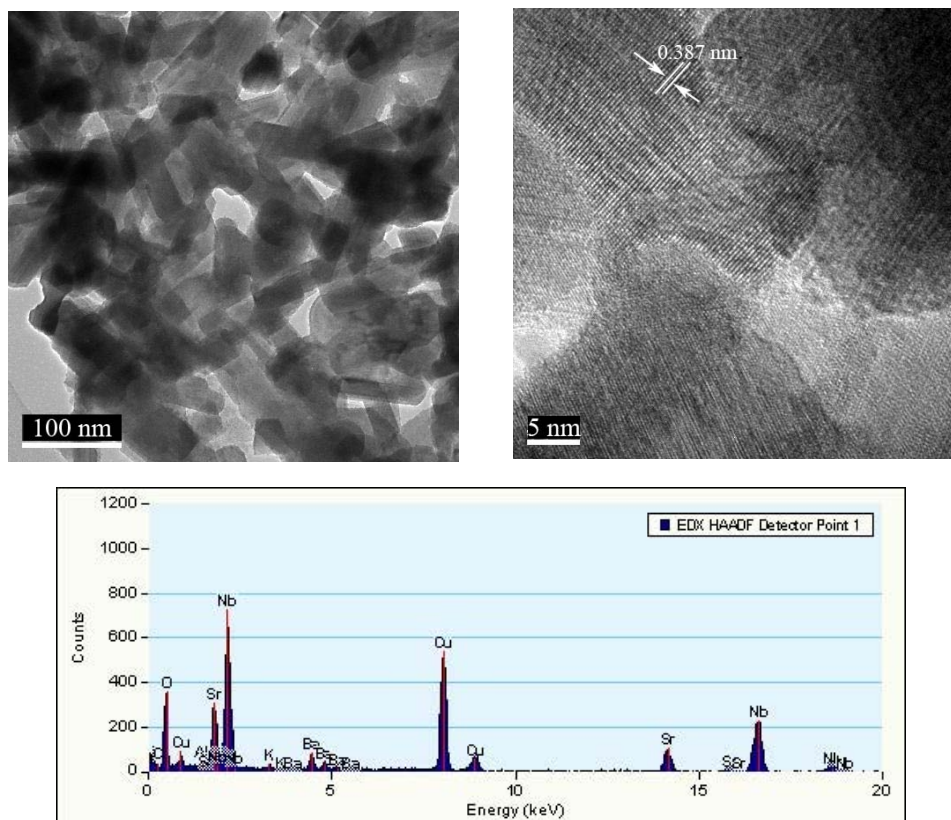


Fig. 6.2 The TEM photographs of: SBN nanocrystals. and the energy dispersive x-ray spectrum of SBN nanocrystals.

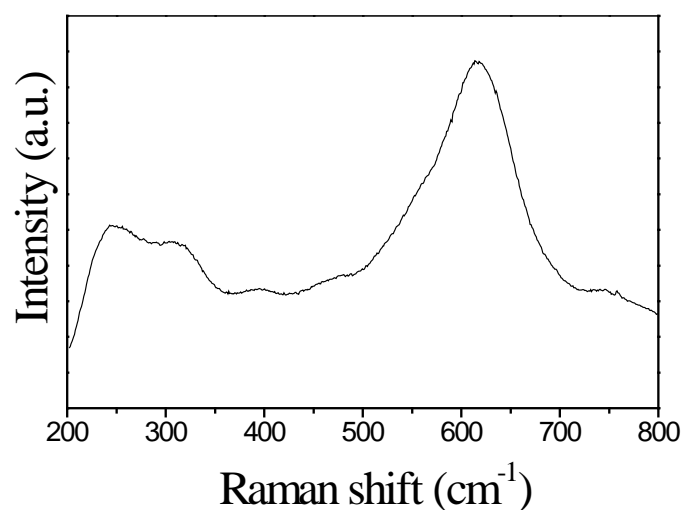


Fig. 6.3 Raman spectrum of as-synthesized SBN nanocrystals.

6.4 Conclusion

SBN nanocrystals with a nanorod-like shape were successfully synthesized, through a simple and convenient Pechini route. XRD patterns showed that the as-prepared sample was well crystalline with pure TTB structure. Raman spectroscopy demonstrated that the as-prepared samples were of high purity. The morphology of synthesized SBN nanocrystals was rod-shaped with a length up to 100 nm and a width within 20 nm. Our results suggest that it is possible to prepare SBN ferroelectric nanorod via this method. Furthermore, the simple and mild route may be extended to prepare other important multi-component TTB structure materials, as well.

7 Conclusions and Future Work

7.1 Conclusions

The present research focused mainly on the investigation of the fabrication, optical properties and magneto-electric properties of TTB structure SCNN and SBN thin films.

Epitaxial SCNN and SBN thin films were deposited on single crystal substrates by pulsed laser deposition. The structural properties of SCNN thin films were studied with regard to the effects of deposition temperature. It was found that the crystalline quality of thin films was enhanced when the deposition temperature was increased. The surface morphology of SCNN thin films depended strongly on the processing conditions. Both the grain size and surface roughness increased with an increase of deposition temperature. The FWHM of dip-modes of the prism coupler shows a direct proportion relationship to the roughness of SCNN films. This suggests that the prism coupler technique can act as a practical and sensitive surface probe.

The waveguiding properties of epitaxial and polycrystalline SCNN films were investigated systematically. Refractive indices dispersive curves of both

films following Sellmeier dispersion relationship were obtained from the measured transmittance curve using the Manifacier model. The polycrystalline SCNN/fused quartz film shows slightly low refractive indices compared to the epitaxial SCNN/MgO films due to more void networks in the polycrystalline SCNN film. The ordinary (n_o) and the extraordinary (n_e) refractive indices of the SCNN/MgO films are determined to be 2.278 and 2.183, respectively. The relatively large index difference of 0.095 compared to that of the polycrystalline film due to uniaxial birefringence is the result of anisotropic crystal microstructure. An optical propagation loss of 0.90 dB/cm for the TE₀ mode of the SCNN/MgO waveguide was measured. This is much smaller than the 2.28 dB/cm of the SCNN/fused quartz waveguide. This result confirms the interest of using a well oriented, textured, and crystallized thin film for integrated optics application.

In order to develop the potential in integrated waveguide optics, epitaxial SCNN/MgO/TiN/Si heterostructures were fabricated successfully by PLD. Furthermore, In:c-MZO, as a replacement of MgO, was also introduced as not only to act as the waveguide buffer layer, but also the conductive bottom electrode in EO modulator. Clear and sharp excited TE mode-lines and TM mode-lines were observed in both heterostructures. An accepted value of propagation loss of 1.7 dB/cm was obtained in our waveguides. On the basis of our results, we show that

these two epitaxial heterostructures, with SCNN films as waveguide layer and MgO or In:c-MZO as buffer layer, are promising waveguiding materials for practical integrated optical devices.

The temperature dependence of refractive index of SBN thin films was investigated using a thermo-controlled prism coupler technique. Epitaxial SBN films exemplify the large changes in refractive indices and birefringence associated with structural phase transitions. At T_c , a value of $dn_o/dT = 3.5 \times 10^{-4} K^{-1}$ was measured. It is believed that the primary contributions of the change of refractive index with temperature are EO effect and changes of polarization. It is possible to make an optical modulator using SBN based on this thermo-optical effect. Besides the thermo-optical properties, EO properties of SCNN films have also been investigated. A simple and direct method based on the shift of the synchronous angles of the guided modes was employed to investigate the effective electro-optic coefficient using two co-planar electrodes. The effective EO coefficient r_{eff} of SCNN thin films was measured to be 176.6 pm/V. The results suggest the feasibility of modulation devices using SCNN ferroelectric thin films for integrated optics.

The temperature dependence of Raman spectra of SBN60 and SCNN films across the ferro-paraelectric phase transition were discussed. In both films, we

believe that the Raman bands and the temperature dependence of their peak position and FWHM are associated with the disorder structure of the TTb structure. The Raman bands of SBN at 240 and 625 cm^{-1} are broader than that of SCNN due to a relative more disorder structure in SBN. The temperature dependence of peak position and FWHM of the Raman bands in both films present clear anomalies at the phase transition. The Raman band at around 240 and 625 cm^{-1} can survive in the paraelectric phase but the slopes of the change of peak position are different before and after the phase transition. It is because that some Nb^{5+} at B1 sites disappear gradually, but Nb^{5+} ions in B2 sites are still Raman active above Curie temperature.

The Brillouin scattering of high *c*-oriented SCNN films on Si (100) substrate over a wide temperature range was investigated in detail. The temperature dependent Brillouin frequency shift shows a broad rising anomaly for both LA and TA phonon modes. A gradual growth in damping with a maximum near 280 °C is observed, at which the low-frequency dielectric constant reaches its maximum value. This result indicates that both modes couple with the fluctuation of PNRs in the same way and the anomalies are caused by the slowing up of the motion of the PNRs. The elastic stiffness C_{11} and C_{44} are also determined between 25 and 450 °C. In addition to the acoustic modes, a

relaxational mode is found in the form of a central peak. The relaxation time τ of the mode has a temperature dependence similar to that of dielectric constant and shows a broad peak anomaly around T_m . By the analysis of modified superparaelectric model, the activation energies of relaxation processes H_0 and Burns temperature T_B are determined to be 1430 K and 805 K, respectively.

Magneto-electric properties of lead-free high Curie temperature SCNN relaxor and CFO ferrite composites were investigated. This composite has been electrically and magnetically poled to exhibit a significant ME effect. A remarkable dielectric constant dispersion spectrum with Curie temperature of 270 °C was observed. A well-defined ferroelectric hysteresis loop with remnant polarization (P_r) and coercive fields (E_c) of about 9.5 $\mu\text{C}/\text{cm}^2$ and 19.1 kV/cm, respectively, and a ferrimagnetic hysteresis loop with remnant magnetization (M_r) and coercive field (H_c) of about 5.2 emu/cm^3 and 206 Oe, respectively, were obtained for the same composite ceramic. A maximum ME coupling coefficient α_E of 58 mV/cm-Oe was obtained under a zero dc bias field and an ac magnetic field of 10 Oe at 88 kHz.

SBN nanocrystals with a nanorod-like shape with a length up to 100 nm and a width within 20 nm were successfully synthesized, through a simple and convenient Pechini route. XRD patterns and Raman spectroscopy demonstrated

that the as-prepared samples were of high purity.

7.2 Future Work

Ferroelectric thin films show great promise as EO and waveguide materials for integrated optics applications, but so far there have been only a few reports on waveguides based on ferroelectric thin films. The following are some suggested topics for future research which may be regarded as an extension of the present work.

The electro-optic properties of the SCNN thin films in this work can be further improved since our EO coefficients are not as high as the published data. If the deposition temperature can be increased to above 800 °C, better EO properties in SCNN thin films may be achieved. Furthermore, to realize better EO properties, we could attempt to use other thin film deposition techniques such as e-beam sputtering, and molecular beam epitaxy. Another important work is the measurement of EO coefficient of the integrated epitaxial SCNN films on Si substrates. This is a very important parameter in this integrated heterostructure.

Although the concept of magneto-electric devices based on ferromagnetic-ferroelectric composite ceramics has been realized both in our work and in several reports, so far there are only limited reports on ME thin film composite systems integrated on single crystal or semiconductor substrates. It is important to fabricate epitaxial ME composite films to investigate the ME properties in 2-dimensional systems.

References

Amzallag, E., Chang, T. S., Pantell, R. H., Feigelson, R. S., “Raman Scattering by $\text{Sr}_x\text{Ba}_{1-x}\text{Nb}_2\text{O}_6$ ”, J. Appl. Phys. **42**, 3254 (1971).

Barker, Jr. A. S., Loudon, R., “Dielectric properties and optical phonons in LiNbO_3 ”, Phys. Rev. **158**, 433 (1967).

Bartlett, K. G., Wall, L. S., “Temperature study of polarized Raman-spectra of strontium barium niobate”, J. Appl. Phys. **44**, 5192-5193 (1973).

Bergmann, M. J., Özgür, Ü., Casey, H. C., Everitt, Jr., H. O., and Muth, J. F., “Ordinary and extraordinary refractive indices for $\text{Al}_x\text{Ga}_{1-x}\text{N}$ epitaxial layers”, Appl. Phys. Lett. **75**, 67 (1999).

Betts, R. A. and Pitt, C. W., “Growth of thin-film lithium niobate by molecular beam epitaxy”, IEEE Electronics Letters. **21**, 960-962 (1985).

Boudiombo, J., Loulergue, J. C., Bath, A., Thevenin, P., “Electro-optical characterization of h-BN thin film waveguides by prism coupler technique”, Mater. Sci & Eng. B. **59**, 244 (1999).

Boudrioua, A., Loulergue, J. C., Dogheche, E., Remiens, D., “Electro-optic characterization of $(\text{Pb}, \text{La})\text{TiO}_3$ thin films using prism coupling technique”, J. Appl. Phys. **85**, 1780 (1999).

Bragg, W. L., “The Specular Reflexion of X-rays”, Nature. **90**, 410 (1912).

Burns, G., Axe, J. D., and Okane, D. F., “Raman measurements of $\text{NaBa}_2\text{Nb}_5\text{O}_{15}$ and related ferroelectrics”, Solid. State. Commun. **7**, 933 (1969).

Burns, G., Dacol, F. H., “Crystalline ferroelectrics with glassy polarization behavior”, Phys. Rev. B. **28**, 2527 (1983).

Busch-Vishniac, IJ., “Trends in electromechanical transduction”, Phys. Today. **51**, 28 (1998).

Chen, H., Jiang, Q., Lu, X., Chen, L., “Studies on growth and photorefractive

properties of manganese-doped potassium sodium strontium barium niobate crystal”, *Ferroelectrics*. **196**, 413 (1997).

Chiu, T. W., Wakiya, N., Shinozaki, K., and Mizutani, “Growth of highly (001)-textured strontium barium niobate thin films on epitaxial $\text{LaNiO}_3/\text{CeO}_2/\text{YSZ}/\text{Si}(100)$ ”, *Thin Solid Films*. **426**, 62 (2003).

Cocorullo, G., Della Corte, F. G., Rendina, I., “Temperature dependence of the thermo-optic coefficient in crystalline silicon between room temperature and 550 K at the wavelength of 1523 nm”, *Appl. Phys. Lett.* **74**, 3338 (1999).

Cordero-Montalvo, C., Vedam, K. “Piezo- and thermo-optic behaviour of LiTaO_3 ”, *J. Appl. Phys.* **52**, 944 (1981).

Dai, Y. R., Bao, P., Zhu, J. S., Wan, J. G., Shen, H. M., and Liu, J. M., “Internal friction study on $\text{CuFe}_2\text{O}_4/\text{PbZr}_{0.53}\text{Ti}_{0.47}\text{O}_3$ composites”, *J. Appl. Phys.* **96**, 5687 (2004).

Dec, J., Kleemann, W., Miga, S., Filipic, C., Levstik, A., Pirc, R., Granzow, T., Pankrath, R., “Probing polar nanoregions in $\text{Sr}_{0.61}\text{Ba}_{0.39}\text{Nb}_2\text{O}_6$ via second-harmonic dielectric response”, *Phys. Rev. B.* **68**, 092105 (2003).

DiDomenico, M., Wemple, S. H., “Optical properties of perovskite oxides in their paraelectric and ferroelectric phases”, *Phys. Rev.* **166**, 565 (1968).

Duong, Giap V., Groessinger, R., “Effect of preparation conditions on magnetoelectric properties of $\text{CoFe}_2\text{O}_4\text{-BaTiO}_3$ magnetoelectric composites”, *Journal of Magnetism and Magnetic Materials* **316**, e624–e627 (2007).

Eerenstein, W., Mathur, N. D., Scott, J. F. “Multiferroic and magnetoelectric materials”, *Nature*. **442**, 759 (2006).

Fan, H. Q., Zhang, L. Y., Yao, X., “Relaxation characteristics of strontium barium niobate ferroelectric ceramics”, *J. Mater. Sci.* **33**, 895 (1998).

Fiebig, M., “Revival of the magnetoelectric effect”, *J. Phys. D.* **8**, R123 (2005).

Foster, C. M., Chan, S. K., Chang, H. L., Chiarello, R. P. and Zhang, T. J., "Electromagnetic modes and prism-film coupling in anisotropic planar waveguides of epitaxial (101) rutile thin films", *J. Appl. Phys.* **73** 7823 (1993).

Francesc, Sepulcre., Grazia, M., Proietti, Maurizio Benfatto, Stefano Della Longa, Joaquin García, and Esteve Padrós, "A Quantitative XANES Analysis of the Calcium High-Affinity Binding Site of the Purple Membrane", *Biophys J.* **87**(1): 513–520 (2004).

Gardiner, D.J. *Practical Raman spectroscopy*. Springer-Verlag. ISBN 978-0387502540. (1989).

Gorouya, Y., Tsujimi, Y., Iwata, M., Yagi, T., "Brillouin scattering study on relaxor ferroelectric $\text{PbZn}_{1/3}\text{Nb}_{2/3}\text{O}_3$ ", *Appl. Phys. Lett.*, **83**, 1358 (2003).

Goulikov, M., Shinkarenko, O., Ivleva, L., Lykov, P., Granzow, T., Woike, Th., Imlau, M., and Wöhlecke, M., "New Parametric Scattering in Photorefractive $\text{Sr}_{0.61}\text{Ba}_{0.39}\text{Nb}_2\text{O}_6 : \text{Cr}$ ", *Phys. Rev. Lett.* **91**, 243903 (2003).

Granzow, T., Woike, Th., Wöhlecke, M., Imlau, M., Kleemann, W., "Change from 3D-Ising to Random Field-Ising-Model Criticality in a Uniaxial Relaxor Ferroelectric", *Phys. Rev. Lett.* **92**, 065701-1 (2004).

H. Stall and A. Yariv, "Coupled mode analysis of periodic dielectric waveguides", *Opt. & mm.* **8**, 5-8 (1973).

Hill, NA., "Density functional studies of multiferroic magnetoelectrics", *Annu. Rev. Mater. Res.* **32**, 1 (2002).

Ho, Melanie M. T., Mak, C. L. Wong, K. H., "Raman scattering and X-ray diffraction investigations of sol-gel derived SBN powders", *J. Euro. Ceram. Soc.* **19**, 1115 (1999).

Husson, E., Repelin, Y., Dao, N. Q., Brusset, H., "Normal coordinate analysis for CaNb_2O_6 of columbite structure", *J. Chem. Phys.* **66**, 5173 (1977).

Imlau, M., Bastwöste, K., Möller, S., Voelker, U., "Dispersion of the electro-optic properties of cerium-doped $\text{Sr}_{0.61}\text{Ba}_{0.39}\text{Nb}_2\text{O}_6$ ", *J. Appl. Phys.* **100**, 053110 (2006).

Iwata, K., Sakemi, T., Yamada, A., Fons, R., Awai, K., Yamamoto, I., Matsubara, M., Tampo, H., Sakurai, K., Ishizuka, S., Niki, S., “Doping properties of ZnO thin films for photovoltaic devices grown by URT-IP (ion plating) method”, *Thin Solid Films*. **451**, 219 (2004).

Jacinto, C., Jaque, D., Martín Rodríguez, E., García Solé, J., “Optical distortions through phase transition in the Nd³⁺:SBN laser crystal”, *Appl. Phys. Lett.* **88**, 161116 (2006).

Jamieson, P. B., Abrahams, S. C. Bernstein, J. L., “Ferroelectric tungsten bronze-type crystal structures: I. Barium Strontium Niobate Ba_{0.27}Sr_{0.75}Nb₂O_{5.78}”, *J. Chem.Phys.* **48**, 5048 (1968).

Jia, Y. M., Zhao, X. Y., Luo, H. S., Or, S. W., and Chan, H. W. L., “Magnetoelectric effect in laminate composite of magnets 0.7Pb(Mg_{1/3}Nb_{2/3})O₃-0.3PbTiO₃ single crystal”, *Appl. Phys. Lett.* **88**, 142504 (2006).

Jiang, F. M. Ko, J.-H., and Kojima, S., “Central peaks and Brillouin scattering in uniaxial relaxor single crystals of Sr_{0.61}Ba_{0.39}Nb₂O₆”, *Phys. Rev. B.* **66**, 184301 (2002).

Jiang, F. M., Kojima, S., “Relaxation mode in 0.65Pb(Mg_{1/3}Nb_{2/3})O₃-0.35PbTiO₃ relaxor single crystals studied by micro-Brillouin scattering”, *Phys. Rev. B.* **62**, 8572 (2000).

Jiang, W. H., Cao, W. W., Yi, X. J., Chen, H. C., “The elastic and piezoelectric properties of tungsten bronze ferroelectric crystals (Sr_{0.7}Ba_{0.3})₂NaNb₅O₁₅ and (Sr_{0.3}Ba_{0.7})₂NaNb₅O₁₅”, *J. Appl. Phys.* **97**, 094106 (2005).

Jong, C. A., and Gan, J. Y., “Crystallization of Sr_{0.5}Ba_{0.5}Nb₂O₆ thin films on LaNiO₃ electrodes by RF magnetron reactive sputtering”, *Jpn. J. Appl. Phys.* **39**, 545 (2000).

Kaminov, I. P., Ramaswamy, V., Schmidt, R. V. and Turner, E. H. “Lithium niobate ridge waveguide modulator”, *Appl. Phys. Lett.* **24**, 622-624 (1974).

Kanamadi, C. M., Kulkarni, S. R., Patankar, K. K., Chougule, S. S., Patil, S. J., and Chougule, B. K., “Magnetoelectric and dielectric properties of $\text{Ni}_{0.5}\text{Cu}_{0.5}\text{Fe}_2\text{O}_4\text{-Ba}_{0.5}\text{Pb}_{0.5}\text{Ti}_{0.5}\text{Zr}_{0.5}\text{O}_3$ ME composites”, *J. Mater. Sci.* **42**, 5080–5084 (2007).

Kang, Y. M. and Baik, S. “Microstructure and optical loss in epitaxial (Pb, La)TiO₃ thinfilms on (001) MgO”, *J. Mater. Res.* **13**, 995-1001 (1998).

Khartsev, S. I., Grishin, M. A., Grishin, A. M., “Characterization of heteroepitaxial $\text{Na}_{0.5}\text{K}_{0.5}\text{NbO}_3/\text{La}_{0.5}\text{Sr}_{0.5}\text{CoO}_3$ electro-optical cell”, *Appl. Phys. Lett.* **86**, 062901, (2005).

Kholkin, A.L., Brooks, K.G. Setter, N., “Electromechanical properties of $\text{SrBi}_2\text{Ta}_2\text{O}_9$ thin films”, *Appl. Phys. Lett.* **71**, 2044 (1997).

Khomchenko, Alexander V. *Waveguide spectroscopy of thin films*, Amsterdam: Elsevier, (2005).

Kim, D. H. and Kwok, H. S. “Pulsed laser deposition of BaTiO₃ thin films and their optical properties”, *Appl. Phys. Lett.* **67**, 1803-1805 (1995).

Kleemann, W., Dec, J., Miga, S., Woike, T., Pankrath, R., “Non-Debye domain-wall-induced dielectric response in $\text{Sr}_{0.61-x}\text{Ce}_x\text{Ba}_{0.39}\text{Nb}_2\text{O}_6$ ”, *Phys. Rev. B.* **65**, 220101 (2002).

Kumar, A., Murari, N. M., and Katiyar, R. S., “Diffused phase transition and relaxor behavior in $\text{Pb}(\text{Fe}_{2/3}\text{W}_{1/3})\text{O}_3$ thin films”, *Appl. Phys. Lett.* **90**, 162903 (2007).

Kuok, M. H., Ng, S. C., Fan, H. J., iwata, M. and Ishibashi, Y., “Hypersonic frequency softening and relaxation in relaxor ferroelectric $0.8\text{Pb}(\text{Zn}_{1/3}\text{Nb}_{2/3})\text{O}_3\text{-}0.2\text{PbTiO}_3$ ”, *Solid. State. Commun.* **118**, 169 (2001).

Lee, M. K., and Feigelson, R. S., “Growth of epitaxial strontium barium niobate thin films by solid source metal-organic chemical vapor deposition”, *J. Cryst. Growth.* **180**, 220 (1997).

Li, A. D, Wu, D, Ming, N. B. China patent, 200410014962.9

Li, M. H., Chong, T. C., Xu, X. W., Kumagai, H., “Influence of Ce and Co doping ions on photorefractive effect of SBN : 61 crystals”, *J. Cryst. Growth.* **225**, 479–483 (2001).

Liang, B. L., Wang, Z. Q., Cartwright, C. M., Zhang, H., Ding, M. S., Gillespie, W. A., “Holographic recording with orthogonally polarized beams in a cesium-doped ($K_{0.5}Na_{0.5}$)_{0.2}($Sr_{0.75}Ba_{0.25}$)_{0.9}Nb₂O₆ crystal”, *Appl. Opt.* **40**, 4667 (2001).

Lima-Silva, J. J., Garcia, D., Mendes Filho, J., Eiras, J. A., Ayala, A. P., “The ferro-paraelectric phase transition of $Pb_{0.6}Ba_{0.4}Nb_2O_6$ investigated by Raman scattering”, *Phys. Stat. Sol. (b)*. **241**, 2001 (2004).

Lin, W. J., Tseng, T. Y., Lin, S. P., Tu, S. L., Yang, S. J., Harn, J. J., Liu, K. S., and Lin, I. N., “Growth of epitaxial-like ($Sr_{0.5}Ba_{0.5}$)Nb₂O₆ ferroelectric-films”, *Jpn. J. Appl. Phys.* **34**, 625-627 (1995).

Lines, M. E., Glass, A. M., *Principles and Applications of Ferroelectrics and Related Materials* (Clarendon, Oxford, 1977).

Liu, W. C., Wu, D., Li, A. D., Ling, H. Q., Tang, Y. F., Ming, N. B., “Annealing and doping effects on structure and optical properties of sol-gel derived ZrO₂ thin films”, *Appl. Surf. Sci.* **191**, 181-187 (2002).

Liu, W. C., Mak, C. L., Wong, K. H., Wang, D. Y., and Chan, H. L. W., “Optical properties of epitaxial and polycrystalline $Sr_{1.8}Ca_{0.2}NaNb_5O_{15}$ thin-film waveguides grown by pulsed laser deposition”, *J. Appl. Phys.* **100**, 033507 (2006).

Liu, W. C., Li, A. D., Tan, J., Wu, D., Ming, N. B., “Preparation and characterization of poled nanocrystal and polymer composite PZT/PC films”, *Appl. Phys. A: Mater. Sci. Proc.* **81**, 543 (2005).

Liu, W. C., Mak, C. L., Wong, K. H., Lo, C. Y., Or, S. W., Zhou, W., Hauser, A.,

Yang, F. Y., and Sooryakumar, R., “Magnetoelectric and dielectric relaxation

properties of the high Curie temperature composite

Sr_{1.9}Ca_{0.1}NaNb₅O₁₅-CoFe₂O₄”, J. Phys. D: Appl. Phys. **41**, 125402 (2008).

Liu, W. C., Wu, D., Li, A. D., Ling, H. Q., Tang, Y. F., and Ming, N. B., “Annealing and doping effects on structure and optical properties of sol-gel derived ZrO₂ thin films”, Appl. Surf. Sci. **191**, 181 (2002).

Ma, Y. G., Cheng, W. N., Ning, M., and Ong, C. K., “Magnetoelectric effect in epitaxial Pb(Zr_{0.52}Ti_{0.48})O₃/La_{0.7}Sr_{0.3}MnO₃ composite thin film”, Appl. Phys. Lett. **90**, 152911 (2007).

Mak, C. L., Luk, C. H., Wong, K. H., “Thickness dependence of the structural properties of sol-gel derived Sr_{0.6}Ba_{0.4}Nb₂O₆ films”, Thin solid films. **325**, 79 (1998).

Manifacier, J. C., Gasiot, J., Fillard, J. P., “Simple method for determination of optical-constants n, k and thickness of a weakly absorbing thin-film”, J. Phys. E. **9**, 1002 (1976).

Manivannan, A., Constantinescu, A. M., Seehra, m. S., “Synthesis of CoFe₂O₄ nanoparticles via the ferri-hydrate route”, Mater. Res. Soc. Symp. Proc. **658**, GG6.32.1 (2001).

Marx, J. M., Tang, Z., Eknayan, O., Taylor, H. F., “Low-loss strain induced optical waveguides in strontium barium niobate (Sr_{0.6}Ba_{0.4}Nb₂O₆) at 1.3 μm wavelength”, Appl. Phys. Letter. **66**, 274 (1995).

Matsubara, K., Tambo, H., Shibata, H., Yamada, A., Fons, P., Iwata, K., Niki, S., “Band-gap modified Al-doped Zn_{1-x}Mg_xO transparent conducting films deposited by pulsed laser deposition”, Appl. Phys. Lett. **85**, 1374, (2004).

Matsunaga, S., Murata, H., Okamura, Y., “Optical pulse generation using guided-wave electrooptic modulator with resonant electrodes and polarization reversal”, J. Lightw. Technol. **24**, 3334 (2006).

Micheron, F., Bismuth, G., “Electrical control of fixation and erasure of

- holographic patterns in ferroelectric materials”, *Appl. Phys. Lett.* **20**, 79 (1972).
- Miller, S. E. “Integrated Optics: an Introduction”. *Bell System Technical Journal*, **48**, 2059 (1969).
- Mir, J. S., and Agostinelli, J. A., “Optical thin-films for wave-guide applications”, *J. Vac. Sci. Technol. A.* **12**, 1439 (1994).
- Miyazaki, T., and Adachi, S., “Analysis of optical-constants for sputter-deposited InSb films based on the interband-transition model”, *Jpn. J. Appl. Phys.* **31**, 979 (1992).
- Moret, M. P., Devillers, M. A. C., Wörhoff, K. and Larsen, P. K. “Optical properties of PbTiO_3 , $\text{PbZr}_x\text{Ti}_{1-x}\text{O}_3$, and PbZrO_3 films deposited by metalorganic chemical vapor on SrTiO_3 ”, *J. Appl. Phys.* **92**, 468-474 (2002).
- Moretti, L., De Stefano, L., Rossi, A.M., Rendina, I., “Dispersion of thermo-optic coefficient in porous silicon layers of different porosities”, *Appl. Phys. Lett.* **86**, 061107 (2005).
- Neurgaonkar, R. R. and Wu, E. T. “Epitaxial growth of ferroelectric $\text{Sr}_{1-x}\text{Ba}_x\text{Nb}_2\text{O}_6$ films for optoelectronic applications”, *Mater. Res. Bull.* **22**, 1095-1102 (1987).
- Neurgaonkar, R. R., Cory, W. K., Oliver, J. R., Sharp, E. J., Wood, G. L., Miller, M. J., Clark, W. W., and Salamo, G. J., “Growth and ferroelectric properties of tungsten bronze $\text{Sr}_{2-x}\text{Ca}_x\text{NaNb}_5\text{O}_{15}$ single-crystals”, *Mater. Res. Bull.* **23**, 1459 (1988).
- Nye, J. F. *Physical Properties of Crystals*. Oxford Science Publications, London (1976).
- Nystrom, M. J., Wessels, B. W., Lin, W. P., Wong, G. K., Neumayer, D. A., Marks, T. J., “Nonlinear-optical properties of textured strontium barium niobate thin-films prepared by metalorganic chemical-vapor-deposition”, *Appl. Phys. Lett.* **66**, 1726-1728 (1995).
- Ohtomo, A., Kawasaki, M., Koida, T., Masubuchi, K., Koinuma, H., Sakurai, Y.,

Yoshida, Y., Yasuda, T., Segawa, Y., “Mg_xZn_{1-x}O as a II-VI widegap semiconductor alloy”, Appl. Phys. Lett. **72**, 2466 (1998).

Palais, J. C. *Fibre Optic Communications*. Prentice Hall, Englewood Cliffs, NJ (1988).

Petraru, A., Schubert, J., Schmid, M. and Buchal, Ch. “Ferroelectric BaTiO₃ thin-film optical waveguide modulators”, Appl. Phys. Lett. **81**, 1375-1377 (2002).

Petrov, V. M., Bichurin, M. I., and Srinivasan, G., “Maxwell–Wagner Relaxation in Magnetolectric Composites”, Tech. Phys. Lett. **30**, 341 (2004).

Petrov, V.M., Bichurin, M. I., Srinivasan, G., Zhai, J., Viehland, D., “Dispersion characteristics for low-frequency magnetolectric coefficients in bulk ferrite-piezoelectric composites”, Solid. State. Communications. **142**, 515 (2007).

Pliska, T., Mayer, F., Fluck, D., Gunter, P., Rytz, D., “Nonlinear optical investigation of the optical homogeneity of KNbO₃ bulk crystals and ion-implanted waveguides”, J. Opt. Soc. Amer. B. **12**, 1878 (1995).

Prokhorov, A. M., *Ferroelectric thin-film waveguides in integrated optics and optoelectronics*. Great Abington, England : Cambridge International Science Pub., 1996.

Quiao, Y., Orlov, S., Psaltis, D., Neurgaonkar, R.R., “Electrical fixing of photorefractive holograms in Sr_{0.75}Ba_{0.25}Nb₂O₆”, Opt. Lett. **18**, 1004 (1993).

Rakuljic, G. A., Yariv, A., Neurgaonkar, R., “Photorefractive properties of undoped, cerium-doped, and Iron-doped single-crystal Sr_{0.6}Ba_{0.4}Nb₂O₆”, Opt. Eng. **25**, 1212 (1986).

Ramírez, M. O., Jaque, D., Bausá, L. E., García Solé, j., Kaminskii, A. A., “Coherent Light Generation from a Nd:SBN Nonlinear Laser Crystal through its Ferroelectric Phase Transition”, Phys. Rev. Lett. **95**, 267401 (2005).

Rouleau, C. M., Jellison, G. E., Jr. Beach, D. B., “Influence of MgO substrate miscut on domain structure of pulsed laser deposited Sr_xBa_{1-x}Nb₂O₆ as

characterized by x-ray diffraction and spectroscopic ellipsometry”, *Appl. Phys. Lett.* **82**, 2990 (2003).

Rush, D. W., Dugan, B. M., Burdge, G. L., “Temperature dependent index of refraction changes in BaTiO₃”, *Opt. Lett.* **16**, 1295 (1991).

Santos, I. A., Spinola, D. U., Garcia, D., Eiras, J. A., “Dielectric behavior and diffuse phase transition features of rare earth doped Sr_{0.61}Ba_{0.39}Nb₂O₆ ferroelectric ceramics”, *J. Appl. Phys.* **92**, 3251-3256 (2002).

Schwyn Thöny, S., Youden, K. E., Harris, J. S. Jr., Hesselink, L., “Growth of epitaxial strontium barium niobate thin films by pulsed laser deposition”, *Appl. Phys. Lett.* **65**, 2018 (1994).

Scott, J. F., and Carlos A. Paz de Araujo, “Ferroelectric Memories”, *Science.* **246**, 1400 (1989).

Scott, J. F., Sheih, S. J., Furer, K. R., Clark, N. A., “Anisotropic thermal-lens effect in ferroelectric Ba₂NaNb₅O₁₅ at T_c”, *Phys. Rev. B.* **41**, 9330 (1990).

Shabbir, G., and Kojima, S., “A micro-Brillouin scattering study of the acoustic properties of PLZT relaxor ceramics”, *J. Phys.: Condens. Matter.* **15**, 7717 (2003).

Shabbir, G., Kojima, S., “A micro-Brillouin scattering study of the acoustic properties of PLZT relaxor ceramics”, *J. Phys: Condensed. Mater.* **15**, 7717 (2003).

Shames, P. E., Sun, P. C., Fainman, Y., “Modeling of scattering and depolarizing electro-optic devices. II. Device simulation”, *Appl. Opt.* **37**, 3726 (1998).

Sharma, A. K., Narayan, J., Muth, J. F., Teng, C. W., Jin, C., Kvit, A., Kolbas, R. M., and Holland, O. W., “Optical and structural properties of epitaxial Mg_xZn_{1-x}O alloys”, *Appl. Phys. Lett.* **75**, 3327 (1999).

Shinya Tsukada, Yuji Ike, and Jun Kano, Tadashi Sekiya, Yoshihito Shimojo, and Ruiping Wang, Seiji Kojima, “Broadband inelastic light scattering of a relaxor ferroelectric 0.71Pb(Ni_{1/3}Nb_{2/3})O₃-0.29PbTiO₃”, *Appl. Phys. Lett.* **89**,

212903 (2006).

Sokoloff, J. P., Chase, L. L., and Rytz, D., “Direct observation of relaxation modes in KNbO_3 and BaTiO_3 using inelastic light-scattering”, *Phys. Rev. B* **38**, 597 (1988).

Sokoloff, J. P., Chase, L. L., Boatner, L. A., “Low-frequency relaxation modes and structural disorder in $\text{KTa}_{1-x}\text{Nb}_x\text{O}_3$ ”, *Phys. Rev. B* **41**, 2398 (1990).

Speghini, A., Bettinelli, M., Caldiño, U., Ramírez, M. O., Jaque, D., Bausá, L. E., and García Solé, J., “Phase transition in $\text{Sr}_x\text{Ba}_{1-x}\text{Nb}_2\text{O}_6$ ferroelectric crystals probed by Raman spectroscopy”, *J. Phys. D: Appl. Phys.* **39**, 4930 (2006).

Suchetelene, J. V., *Philips Res. Rep.* **27**, 28 (1972).

Szaniacs J, Kakihana M., “A novel tantalic acid-based polymerizable complex route to LiTaO_3 using neither alkoxides nor chlorides of tantalum”, *Chem. Mater.* **11**:2760-3 (1999).

Tang, Y. H., Chen, X. M., Li, Y. J., Zheng, X. H., “Dielectric and magnetoelectric characterization of $\text{CoFe}_2\text{O}_4/\text{Ba}_{0.55}\text{Sr}_{0.25}\text{Ca}_{0.2}\text{Nb}_2\text{O}_6$ composites”, *Mater. Sci & Eng B.* **116**, 150–155 (2005).

Tayebati, P., Trivedi, D., Tabat, M., “Pulsed laser deposition of SBN:75 thin films with electro-optic coefficient of 844 pm/V”, *Appl. Phys. Lett.* **69**, 1023 (1996).

Terui, y., and Ando, S., “Anisotropy in thermo-optic coefficients of polyimide films formed on Si Substrates”, *Appl. Phys. Lett.* **83**, 4755 (2003).

Thapliya, R., Okano, Y. and Nakamura, S. “Electrooptic characteristics of thin-film PLZT waveguide using ridge-type Mach-Zehnder modulator”. *IEEE Journal of Lightwave Technology.* **21**, 1820-1827 (2003).

Trainer, M., “Ferroelectrics and the Curie-Weiss law”, *Euro. J. Phys.* **21**, 459 (2000).

Trivedi, D., Tayebati, P., Tabat, M., “Measurement of large electro-optic coefficients in thin films of strontium barium niobate ($\text{Sr}_{0.6}\text{Ba}_{0.4}\text{Nb}_2\text{O}_6$)”, *Appl. Phys. Lett.* **68**, 3227 (1996).

Tsukada, S., Ike, Y., Kano, J., Sekiya, T., Shimojo, Y., and Wang, R., Kojima, S., “Broadband inelastic light scattering of a relaxor ferroelectric $0.71\text{Pb}(\text{Ni}_{1/3}\text{Nb}_{2/3})\text{O}_3\text{-}0.29\text{PbTiO}_3$ ”, *Appl. Phys. Lett.* **89**, 212903 (2006).

Uchino, K., Nomura, S., “Critical exponents of the dielectric-constants in diffused-phase-transition crystals”, *Ferroelectr. Lett. Sect.* **44**, 55 (1982).

Ulrich, R., and Torge, R., “Measurement of thin-film parameters with a prism coupler”, *Appl. Opt.* **12**, 2901-2908 (1973).

Valasek, “Piezoelectric and allied phenomena in Rochelle salt”, *J. Phys. Rev.* **15**, 537 (1920).

Volk, T., Isakov, D., Salobutin, V., Ivleva, L., Lykov, P., Ramzaev, V., Wöhlecke, M., “Effects of Ni doping on properties of strontium-barium-niobate crystals”, *Solid State Commun.* 130 (2004) 223–226.

Wan, J. G., Zhang, H., Wang, X. W., Pan, D. Y., Liu, J. M., and Wang, G. H., “Magnetoelectric CoFe_2O_4 -lead zirconate titanate thick films prepared by a polyvinylpyrrolidone-assisted sol-gel method”, *Appl. Phys. Lett.* **89**, 122914 (2006).

Wang, M. R., Xu, G., Lin, F. and Jansson, T. “Single-mode/multimode waveguide electro-optic grating coupler modulator”, *Appl. Phys. Lett.* **66**, 2628-2630 (1995).

Wegner, A.B., Brueck, S.R.J., Wu, A.Y., “Integrated PLZT thin-film wave-guide modulators”, *Ferroelectrics.* **116**, 195 (1991).

White, J. M., and Heidrich, P. F., “Optical-waveguide refractive-index profiles determined from measurement of mode indexes-simple analysis”, *Appl. Opt.* **15**, 151 (1976).

Woike, Th., Weckwerth, G., Palme, H., Pankrath, R., “Instrumental neutron

activation and absorption spectroscopy of photorefractive strontium-barium niobate single crystals doped with cerium”, *Solid State Commun.* **102**, 743-747 (1997).

Xia, H. R., Chen, H. C., Yu, H., Wang, K. X., Zhao, B. Y., “Vibrational spectra of a $K_{0.30}Na_{0.10}Sr_{0.48}Ba_{0.32}Nb_2O_6$ single crystal studied by Raman and infrared reflectivity spectroscopy”, *Phys. Stat. Sol. (b)*. **210**, 47 (1998).

Xie, R. J., Akimune, Y., “Lead-free piezoelectric ceramics in the $(1-x)Sr_2NaNb_5O_{15-x}Ca_2NaNb_5O_{15}$ ($0.05 < x < 0.35$) system”, *J. Mater. Chem.* **12**, 3156 (2002).

Xie, R. J., Akimune, Y., Matsuo, K., Sugiyama, T., Hirosaki, N., and Sekiya, T., “Dielectric and ferroelectric properties of tetragonal tungsten bronze $Sr_{2-x}Ca_xNaNb_5O_{15}$ ($x = 0.05-0.35$) ceramics”, *Appl. Phys. Lett.* **80**, 835 (2002).

Xiong, S. B., Ye, Z. M., Chen, X. Y., Guo, X. L., Zhu, S. N., Liu, Z. G., Lin, C. Y., and Jin, Y. S., “Ferroelectric $Sr_xBa_{1-x}Nb_2O_6$ optical waveguiding thin films on SiO_2 -coated Si(1 0 0) substrates”, *Appl. Phys. A*. **67**, 313 (1998).

Xu, Y. H. “Ferroelectric materials and their applications”, Amsterdam; New York: North-Holland, (1991).

Xu, T. H., Chen, C. J., Xu, R., Mackenzie, J. D., “Ferroelectric $Sr_{0.60}Ba_{0.40}Nb_2O_6$ thin films by the sol-gel process: Electrical and optical properties”, *Phys. Rev. B*. **44**, 35 (1991).

Yang, Y. S. Ryu, M. K. Joo, H. J. Lee, S. H. Lee, S. J. Kang, K. Y., Jang, M. S., “Ferroelectricity and electronic defect characteristics of *c*-oriented $Sr_{0.25}Ba_{0.75}Nb_2O_6$ thin films deposited on Si substrates”, *Appl. Phys. Lett.* **76** 3472 (2000).

Yariv, A and Yeh, P. “Optical Wave in Crystals”. *Optical Electronics*. New York: Wiley (1984).

Yin, J, Wu, Z. C., Wang, Z. L., Zhu, Y. Y. Liu, Z. G., “Pulsed laser deposition of $SrBi_2Ta_2O_9$ films on fused silica in waveguide form”, *J. Phys. D: Appl. Phys.* **31**,

3185 (1998).

Yoshiharu, T., Shinji, A., “Anisotropy in thermo-optic coefficients of polyimide films formed on Si substrates”, *Appl. Phys. Lett.* **85**, 4755 (2003).

Yoshihiro Gorouya and Yuhji Tsujimi, Makoto Iwata, Toshirou Yagi, “Brillouin scattering study on relaxor ferroelectric $\text{Pb}(\text{Zn}_{1/3}\text{Nb}_{2/3})\text{O}_3$ ”, *Appl. Phys. Lett.* **83**, 1358 (2003).

Zhai, J. W., Yao, X. and Zhang, L. Y. “The optical waveguide characteristics of highly oriented sol-gel derived polycrystalline ferroelectric PZT thin films”, *Ceramics International.* **27**, 585-589 (2001).

Zhang, H.Y., He, X.H., Shih, Y.H., Tang, S.H., “A new method for measuring the electrooptic coefficients with higher sensitivity and higher accuracy”, *Opt. Commun.* **86**, 509 (1991).

Zhang, X. J., Fan, X. Z., Wang, H. T., He, J. L., Ming, N. B., “Simple and efficient technique for evaluating the optical losses from surface scattering and volume attenuation in a thin film”, *Opt. Express.* **10**, 1485-1490 (2002).

Zhang, Y. L., Mak, C. L., Wong, K. H., and Choy, C. L., “Epitaxial growth and optical properties of $\text{Sr}_{2-x}\text{Ca}_x\text{NaNb}_5\text{O}_{15}$ thin films by pulsed laser deposition”, *Thin Solid Films.* **449**, 63 (2004).

Zheleva, T., Jagannadham, K., Narayan, J., “Epitaxial-growth in large-lattice-mismatch systems”, *J. Appl. Phys.* **75**, 860-871 (1994).

Zheng, H., Wang, J., Lofland, S. E., Ma, Z., Mohaddes-Ardabili, L., Zhao, T., Salamanca-Riba, L., Shinde, S. R., Ogale, S. B., Bai, F., Viehland, D., Jia, Y., Schlom, D. G., Wuttig, M., Roytburd, A., Ramesh, R., “Multiferroic $\text{BaTiO}_3\text{-CoFe}_2\text{O}_4$ Nanostructures”, *Science.* **303**, 661 (2004).

Zhu, Y. Y., Fu, J. S., Xiao, R. F., and Wong, G. K. L., “Second harmonic generation in periodically domain-inverted $\text{Sr}_{0.6}\text{Ba}_{0.4}\text{Nb}_2\text{O}_6$ crystal plate”, *Appl. Phys. Lett.* **70**, 1793 (1997).

Zhu, Y. Y., Xiao, R. F., Fu, J. S., Wong, G. K. L., and Ming, N. B.,

“Second-harmonic generation in quasi-periodically domain-inverted $\text{Sr}_{0.6}\text{Ba}_{0.4}\text{Nb}_2\text{O}_6$ optical superlattices”, *Opt. Lett.* **22**, 1382 (1997).

Appendix

Characterization method

A1. X-ray Diffraction

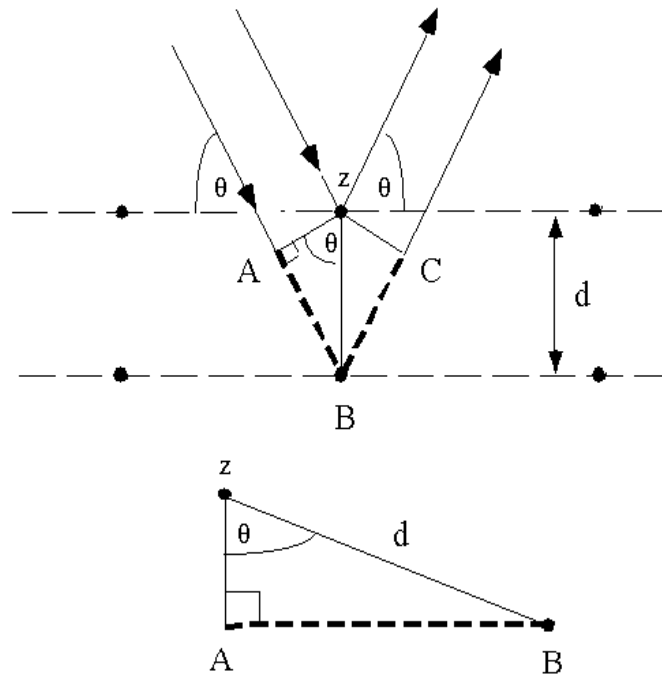
Diffraction occurs as waves interact with a regular structure whose repeat distance is about the same as the wavelength. The phenomenon is common in the natural world, and occurs across a broad range of scales. For example, light can be diffracted by a grating having scribed lines spaced on the order of a few thousand angstroms, about the wavelength of light. It happens that X-rays have wavelengths on the order of a few angstroms, the same as typical interatomic distances in crystalline solids. That means X-rays can be diffracted from minerals which, by definition, are crystalline and have regularly repeating atomic structures. When certain geometric requirements are met, X-rays scattered from a crystalline solid can constructively interfere, producing a diffracted beam. In 1912, W. L. Bragg recognized a relationship among several factors [Bragg, 1912].

i). d-spacing is the distance between similar atomic planes in a mineral (the interatomic spacing) and is measured in angstroms.

ii). The angle of diffraction, which we call the theta angle, is measured in degrees.

For practical reasons the diffractometer measures an angle twice that of the theta angle. Not surprisingly, we call the measured angle '2-theta'.

iii). The wavelength of the incident X-radiation.



These factors are combined in Bragg's Law:

$$n\lambda = 2d\sin\theta$$

Where:

n = an integer - 1, 2, 3..., etc ($n=1$ for our calculations)

λ (lambda) = wavelength in angstroms (1.54Å for copper)

d (d-spacing) = interatomic spacing in angstroms

θ (theta) = the diffraction angle in degrees

Fig. A1 Bragg'S Law

Basing on the Bragg's Law, the lattice constant at different plane can be obtained. In the present research work, XRD has three main functions to investigate the material crystal structures.

- i) $\theta - 2\theta$ scan is used to investigate the phase and out-plane relationship between films and substrates and the crystals phase of powders. It allows us to observe the lattice planes of the thin films grown with the direction of the substrate surface.
- ii) ω scan is used to characterize the films crystal quality. The value of the Full Width Half Maximum (FWHM) reflects the degree of the orientation of the thin films. The smaller the FWHM, the higher the degree of orientation. Generally, a FWHM of $\sim 1^\circ$ is considered to be good oriented film and if it is $< 1^\circ$, it can be said as highly oriented films.
- iii) Phi scan is used to investigate the in-plane relationship between epitaxial films and substrates. Figure A2 shows the three scan methods.

ω – angle between incident x-rays and sample surface
 2θ – angle between incident x-rays and detector
 ψ – sample tilt
 ϕ – in-plane sample rotation
 x,y – in-plane displacement of sample
 z – vertical displacement of sample

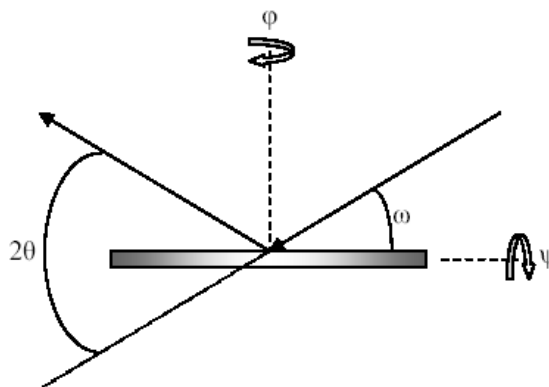


Fig. A2 Phi and omega scan.

A2. Scanning Electron Microscopy (SEM) and Energy-Dispersive X-ray spectrometer (EDX)

Use of SEM permits to analyze solid specimens. We used a Field Emission Scanning Electron Microscope (FESEM) - JEOL JSM-6335F and a Leica stereoscan 440 to obtain sample surface morphology and the cross-section images. For FESEM, a field emission cathode in the electron gun of a scanning electron microscope provides narrower probing beams at high electron energy than those found in conventional SEM. Consequently it provides both improved spatial

resolution and minimized sample charging and damage. In SEM, electrons from a thermionic, Schottky or field-emission cathode are accelerated through a voltage difference between cathode and anode that may be as low as 0.1 keV or as high as 50KeV. The interactions with the electron beam and the specimen surface cause several types of energetic emissions, including backscattered electrons, secondary electrons, Auger electrons (a special form of secondary electron), continuous X-rays and characteristic X-rays that are emitted from the area of the specimen where the electron beam is impinging. The induced signals are detected by the detector. The signals from the detector are then amplified by circuitry and synchronized with the scan generator to produce a SEM image, which comes from the secondary and backscattered electrons. Phases within a material are distinguished by the backscattered electrons. The SEM specimens need to be conductive. Inconductive specimen will build up negative charges on its surface and will deflect the incident electron beam and corrupt the image, therefore dielectric specimens should be coated with a conductive layer such as Au, Pt or carbon with thickness about 10 to 20 nm. This will help to increase secondary and backscattered electron emissions, to reduce thermal damages and to eliminate surface charging, leading to a relatively sharper SEM image. Energy Dispersive X-Ray Fluorescence Spectrometer (EDX) system is often installed in the SEM

equipment to identify the type and the amount of element species in the specimens.

A3. Atomic Force Microscopy (AFM)

The development of AFM was preceded by the development of the scanning tunneling microscopy (STM) in 1981 at IBM Zurich Research Laboratory by Binnig and Rohrer. STM can be used to view the atomic lattice of a sample surface. They were offered the Nobel Prize in physics in 1986. Although the STM provides subangstrom resolution, it is limited to conductive and semi-conductive samples. To image insulators as well as conductors, the atomic force microscope (AFM) was developed in 1986, and the first commercial AFMs were produced in 1989 by Digital Instruments.

AFM consists of a sharp tip sitting on the end of a flexible cantilever. The AFM images are obtained by scanning the sharp tip across a sample surface with a small continuous force. The tips typically have an end radius of a few nm depending on tip type. The scanning motion is conducted by a piezoelectric scanner which scans the tip in a raster pattern with respect to the sample (or scans to the sample with respect to the tip). The tip-sample interaction is monitored by reflecting a laser off the back of the cantilever into a split photodiode detector. By

detecting the difference in the photodiode detector output voltages, changes in the cantilever deflection or oscillation amplitude are determined. Fig. A3 is the schematic of the major components of an AFM.

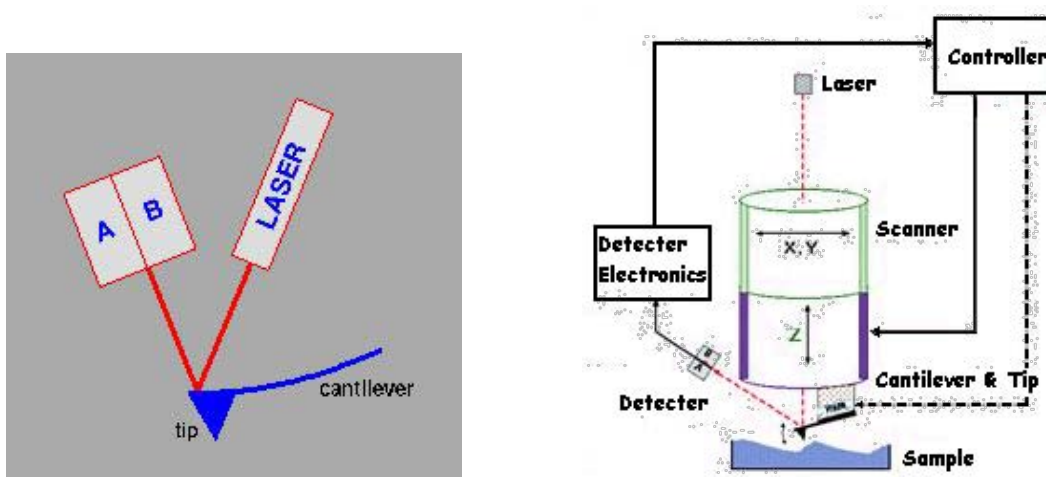


Fig. A3 Schematic of the major components of an AFM

A4. Transmission spectrometer

The optical transmittance measurements were carried out by a two-beam spectrophotometer (Shimadzu UV-2101). This spectrophotometer has a broad light source of wavelength from 200nm to 900nm. From transmittance spectra, optical band gap and wavelength-dependence refractive index can be calculated. The band gap energy and the transition mechanism could be deduced by a profile of $(\alpha h\nu)^n$ against $h\nu$, where α is absorption coefficient and n is under the

dependence of the transition mechanism. α can be expressed as $\alpha = (\ln 1/T)/d$, where T is the transmittance and d is the thickness of the film. The material is said to possess indirect band gap if $n=0.5$, and direct band gap if $n=2$.

The optical constants, i.e. the refractive index (n) and the extinction coefficient (k) of the films were determined from the transmittance spectrum. Following the method of Swanepoel, two envelopes are drawn through the maxima (T) and minima (T) of the oscillating Max Min transmittance. Then the refractive index (n) and extinction coefficient (k) are given as: [Zhang, 2004; Swanepoel, 1983]

$$n = [N + (N^2 - n_s^2)^{1/2}]^{1/2}$$

$$k = -\frac{\lambda}{4\pi d} \ln \frac{E_M - [E_M^2 - (n-1)^3(n^2 - n_s^4)]^{1/2}}{(n-1)^3(n - n_s^2)}$$

where

$$N = 2n_s \frac{T_{Max} - T_{Min}}{T_{Max} T_{Min}} + \frac{n_s^2 + 1}{2},$$

$$E_M = \frac{8n^2 n_s}{T_{Max}} + (n^2 - 1)(n^2 - n_s^2)$$

where n is the refractive index of the substrate and d is the film thickness. In addition, the basic equation for interference fringes is

$$2nd = m\lambda \quad (\text{A2})$$

where m is an integer for maxima or a half integer for minima. If n_1 and n_2 are the refractive indices at two adjacent maxima (or minima) at λ_1 and λ_2 , the thickness d is given by

$$d = \frac{\lambda_1 \lambda_2}{n_2 \lambda_1 - n_1 \lambda_2} \quad (\text{A3})$$

It should be noted that this method may not be accurate for deriving the refractive index since it largely depends on the quality of the film.

A5. Prism Coupler technique

The optical waveguide properties were examined by a prism coupler method (Model 2010 prism, Metricon, USA) using a 632.8 nm laser beam. As shown in Fig. 1.5. A rutile prism is used to couple a laser beam to the waveguide structure. The angle of incidence of the laser beam can be varied by means of a rotary table upon which the prism, film, coupling head, detector for m-line are mounted. At certain discrete values of the incident angle, called mode angles, photons can tunnel across the air gap into an optical propagation waveguide mode, causing a

sharp drop in the intensity of light reaching the detector. The laser beam is polarized with the electric field in the plane of the film (TE mode) or perpendicular to the film surface (TM mode). As recalled in Chapter 1, we can calculate the refractive index and thickness of the waveguide film using the measured values of mode angles. By recording the optical intensity at different sites using detector for loss, we can calculate the optical loss.

A6. Raman spectroscopy

Although the inelastic scattering of light was predicted by Smekal in 1923, it was not until 1928 that it was observed in practice. The Raman effect was named after one of its discoverers, the Indian scientist Sir C. V. Raman who observed the effect by means of sunlight (1928, together with K. S. Krishnan and independently by Grigory Landsberg and Leonid Mandelstam) [Gardiner. 1989]. Raman won the Nobel Prize in Physics in 1930 for this discovery accomplished using sunlight, a narrow band photographic filter to create monochromatic light and a "crossed" filter to block this monochromatic light. He found that light of changed frequency passed through the "crossed" filter. Subsequently the mercury arc became the principal light source, first with photographic detection and then with spectrophotometric detection. Currently lasers are used as light sources.

The Raman effect occurs when light impinges upon a molecule and interacts with the electron cloud of the bonds of that molecule. The incident photon excites one of the electrons into a virtual state. For the spontaneous Raman effect, the molecule is excited from the ground state to a virtual energy state, and relaxes into a vibrational excited state, which generates Stokes Raman scattering. If the molecule was already in an elevated vibrational energy state, the Raman scattering is then called anti-Stokes Raman scattering. A molecular polarizability change, or amount of deformation of the electron cloud, with respect to the vibrational coordinate is required for the molecule to exhibit the Raman effect. The amount of the polarizability change will determine the Raman scattering intensity, whereas the Raman shift is equal to the vibrational level that is involved.

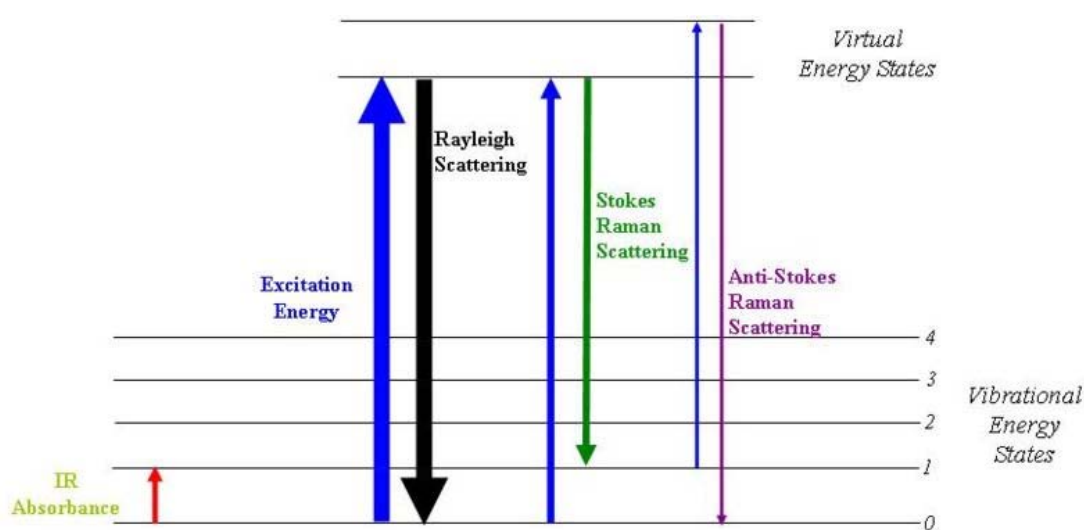


Fig. A4 Energy level diagram showing the states involved in Raman signal.

Raman spectroscopy is commonly used in chemistry, since vibrational information is very specific for the chemical bonds in molecules. It therefore provides a fingerprint by which the molecule can be identified. The fingerprint region of organic molecules is in the range $500\text{-}2000\text{ cm}^{-1}$. Another application of the technique is that it is used to study changes in chemical bonding, e.g. when a substrate is added to an enzyme.

In solid state physics, spontaneous Raman spectroscopy is used to, among other things, characterize materials, measure temperature, and find the crystallographic orientation of a sample. As with single molecules, a given solid material has characteristic phonon modes that can help an experimenter identify it. In addition, Raman spectroscopy can be used to observe other low frequency excitations of the solid, such as plasmons, magnons, and superconducting gap excitations.

The spontaneous Raman signal gives information on the population of a given phonon mode in the ratio between the Stokes (downshifted) intensity and anti-Stokes (upshifted) intensity. Raman scattering by an anisotropic crystal gives information on the crystal orientation. The polarization of the Raman scattered light with respect to the crystal and the polarization of the laser light

can be used to find the orientation of the crystal, if the crystal structure (specifically, its point group) is known.

A7. Brillouin light Scattering (BLS)

Brillouin scattering, named after Léon Brillouin, occurs when light in a medium (such as water or a crystal) interacts with time-dependent density variations and changes its energy (frequency) and path. The density variations may be due to acoustic modes, such as phonons, or temperature gradients. As described in classical physics, when the medium is compressed its index of refraction changes and the light's path necessarily bends.

The phenomenon of inelastic scattering of light due to acoustic phonons was first described by Leon Brillouin (1889-1969) in 1922 and 4 years later in 1926 independently by Leonid Mandelstam. In order to credit Mandelstam it is also denoted as Brillouin-Mandelstam scattering (BMS). Other commonly used names are Brillouin light scattering (BLS) and Brillouin-Mandelstam light scattering (BMLS).

From a quantum point of view, Brillouin scattering is an interaction of light photons with acoustic or vibrational quanta (phonons), with magnetic spin waves

(magnons), or with other low frequency quasiparticles interacting with light. The interaction consists of an inelastic scattering process in which a phonon or magnon is either created (Stokes process) or annihilated (anti-Stokes process). The energy of the scattered light is slightly changed: it is decreased for a Stokes process and increased for an anti-Stokes process. This shift, known as the *Brillouin shift*, is equal to the energy of the interacting phonon and magnon and thus Brillouin scattering can be used to measure phonon and magnon energies. The Brillouin shift is commonly measured by the use of a Brillouin spectrometer based on a Fabry-Pérot interferometer.

The inelastic scattering process of Brillouin light scattering is in principle the same as Raman scattering. Historically Brillouin scattering is called the scattering of acoustic phonons, while Raman scattering refers to the scattering from molecule vibrations and optic phonons. Nowadays the difference between Brillouin scattering and Raman scattering is considered to lie in the different experimental techniques and the different available frequency range. The term Brillouin scattering labels an experimental detection of the frequency shift with an interferometer, while Raman scattering is concerned with a setup employing a grating spectrometer. Brillouin scattering is technically limited to the detection of quasiparticles with frequencies below about 500 GHz, while with Raman

scattering much higher frequencies in the THz range can be measured.

A8. Vibrating sample magnetometer

The vibrating sample magnetometer has become a widely used instrument for determining magnetic properties of a large variety of materials: diamagnetics, paramagnetics, ferromagnetics, ferromagnetics and antiferromagnetics. This experimental technique was invented in 1956 by Simon Foner, a scientist of the MIT. Powders, bulk and thin films can be measured and studied.

If a sample of any material is placed in a uniform magnetic field, created between the poles of an electromagnet, a dipole moment will be induced. If the sample vibrates with sinusoidal motion a sinusoidal electrical signal can be induced in suitable placed pick-up coils. The signal has the same frequency of vibration and its amplitude will be proportional to the magnetic moment, amplitude, and relative position with respect to the pick-up coils system. Fig. A5 shows the vibrating sample magnetometer block diagram.

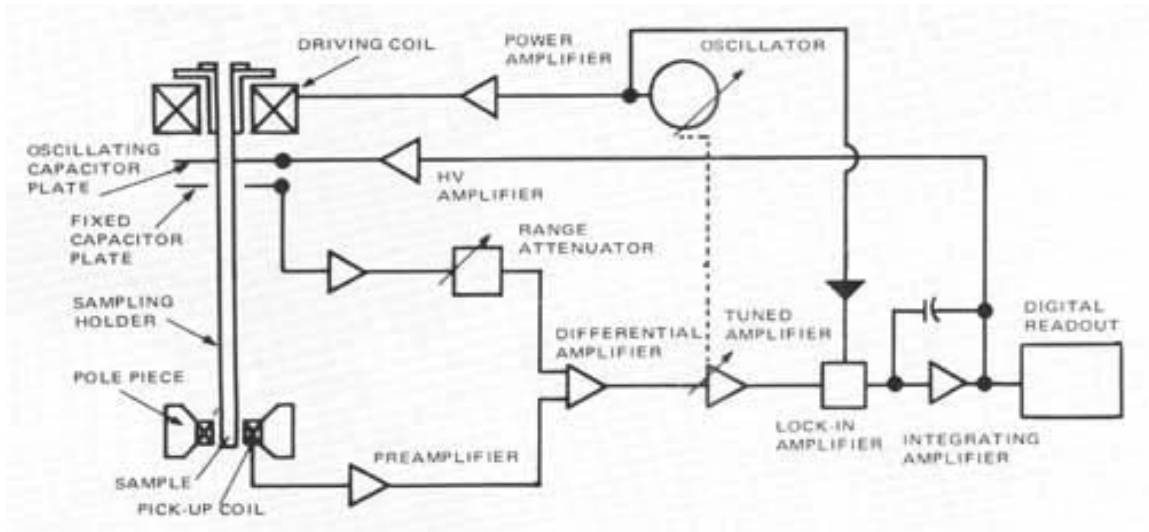


Fig. A5 Schematic of the vibrating sample magnetometer.

The sample is fixed to a small sample holder located at the end of a sample rod mounted in an electromechanical transducer. The transducer is driven by a power amplifier which itself is driven by an oscillator at a frequency of 90 Hertz. So, the sample vibrates along the Z axis perpendicular to the magnetizing field. The latter induced a signal in the pick-up coil system that is fed to a differential amplifier. The output of the differential amplifier is subsequently fed into a tuned amplifier and an internal lock-in amplifier that receives a reference signal supplied by the oscillator. The output of this lock-in amplifier, or the output of the magnetometer itself, is a DC signal proportional to the magnetic moment of

the sample being studied. The electromechanical transducer can move along X, Y and Z directions in order to find the saddle point (which calibration of the vibrating sample magnetometer is done by measuring the signal of a pure Ni standard of known saturation magnetic moment placed in the saddle point).

Using a vibrating sample magnetometer one can measure the DC magnetic moment as a function of temperature, magnetic field, angle and time. So, it allows to perform susceptibility and magnetization studies. Some of the most common measurements done are: hysteresis loops, susceptibility or saturation magnetization as a function of temperature (thermomagnetic analysis), magnetization curves as a function as a function of angle (anisotropy), and magnetization as a function of time.

A9. P-E loop measurement

Polarisation is defined as:

$$P = \frac{Q}{A} \tag{A4}$$

where Q is the charge developed on the plates (Coulombs) and A is the area of the plates (m^2). A good ferroelectric has $10 \mu\text{C cm}^{-2} < P < 100 \mu\text{C cm}^{-2}$.

We can measure the polarisation by using the classic Sawyer-Tower circuit, as shown in Fig. A6. During this experiment, the voltage is cycled by a signal generator. Its direction is reversed at high frequency, and the voltage across the reference capacitor is measured. The charge on the capacitor must be the same as the charge over the ferroelectric capacitor, as they are in series. This means the charge on the ferroelectric can be found by:

$$Q = C \times V \tag{2.5}$$

where C is the capacitance of the reference capacitor, and V is the voltage measured over this capacitor. We can therefore represent the polarization of a material in an oscillating electric field, by plotting the voltage applied to the material on the x-axis of the oscilloscope, and the surface charge on the y-axis.

This can be done because the capacitance of the reference capacitor is much higher

than the capacitance of the ferroelectric, so most of the voltage is applied to the ferroelectric. It is only possible to measure P by cycling the polarization through cycling the voltage across the ferroelectric. We cannot measure absolute values instantaneously, but can deduce absolute values from the changes measured when cycling the polarization.

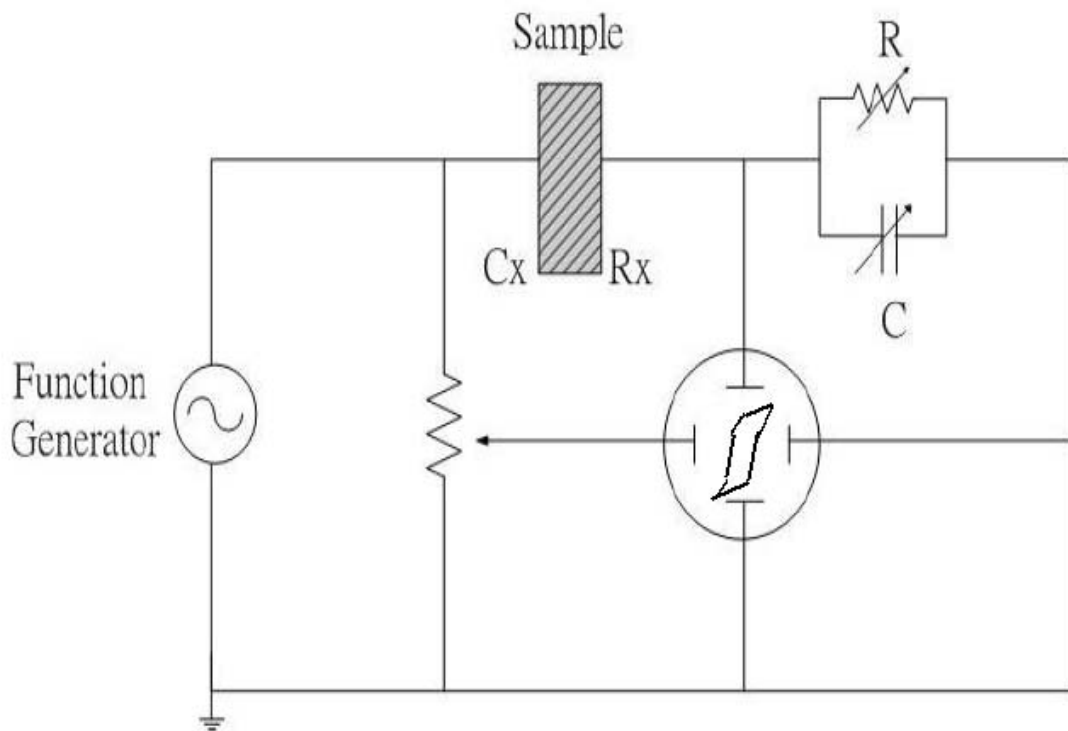


Fig. A6 Schematic of the Sawyer-Tower.